UNIVERSITÉ DE GRENOBLE

THÈSE

Pour obtenir le grade de

DOCTEUR DE L'UNIVERSITÉ DE GRENOBLE

Spécialité : **Physique**

Arrêté ministériel : 7 août 2006

Présentée par

Valentin Taufour

Thèse dirigée par **J.-P. Brison**
et codirigée par **D. Aoki & J. Flouquet**

préparée au sein **du CEA Grenoble**
et de **Ecole doctorale de Physique de Grenoble**

Croissance de cristaux de composés à base d'Uranium et étude de UGe_2

Thèse soutenue publiquement le **28 septembre 2011**,
devant le jury composé de :

P. C. Canfield
Ames Laboratory, Iowa State University, Rapporteur, Président
A. De Visser
Van der Waals Zeeman Institute, University of Amsterdam, Rapporteur
K. G. Sandeman
Imperial College London, Examinateur
C. Paulsen
CNRS, Grenoble, Examinateur
J. Flouquet
CEA Grenoble, Co-Directeur de thèse
D. Aoki
CEA Grenoble, Co-Directeur de thèse

Acknowledgment

First of all I thank Paul Canfield and Anne De Visser for having accepted to be referee of my thesis, for their efforts to read this thesis and give me feedback. I appreciate that it is a big task! Paul is acknowledged on three counts for having also taken the role of president and for taking me as a post-doc. I thank also Carley Paulsen and Karl Sandeman. I am honored to have them in my jury.

Jacques est un directeur de thèse toujours disponible, toujours motivé et motivant, ayant toujours plusieurs idées pour expliquer les résultats ou non-résultats d'une mesure... « Toujours » signifiant également le week-end, les jours fériés, la nuit... Il sait débloquer n'importe quelle situation rapidement, de la disponibilité du matériel experimental aux problèmes administratifs en passant par le changement d'objectif d'une manip. Bref, ce n'était que du bonheur pour moi.

I like to thank Dai for being responsible of the success of my thesis. I learned a lot from him about the experiments, the physics, how to tell Hai I want to work on sunday, cook japanese dishes... He succeeded to be a good supervisor and a good friend.

Jean-Pascal s'est toujours occupé de ma bonne santé, toujours le premier à s'inquiéter si je n'avais pas pris 3 desserts au restaurant ! J'ai également beaucoup profité de sa rigueur scientifique.

I thank my friend Tatsuma who have had a hidden but enormous influence on my life as a PhD student. I shared the way he enjoys physics, magic, brain teaser, hopeful mind, friendship, sushi, kendama....

Je remercie aussi GEORG pour toute l'attention qu'il porte aux autres et en l'occurence à moi, que ce soit pour les manips mais aussi pour le reste : sport, soirées, barbecue... Wunderbar !

Daniel m'a également beaucoup aidé. Je n'ai pas fini d'admirer sa patience et son savoir-faire expérimental.

Je remercie les membres du club D5 (jeu de mots que je viens de trouver pour l'occasion !) : Gerard, Christophe et Karine pour leur disponibilité et sympathie. Ma thèse a commencé avec l'installation du four tetra-arc qui s'est passée facilement grâce à eux. J'aime beaucoup discuter avec Gerard et j'en garde un excellent souvenir. Je constate que je ne suis pas le seul de cet avis ici en Iowa ! I take this opportunity to also thank T. Komatsubara and M. Suzuki for their help to set up the tetra-arc furnace.

Je fais une standing ovation pour Jean-Michel qui fait tourner toutes les dilus, et surtout les vieilles marmites qui font les meilleures soupes... J'aime beaucoup discuter avec lui.

Je remercie les premières personnes avec lesquelles j'ai travaillé, Alain et Atsushi, qui m'ont initié à la physique expérimentale et m'ont intégré dans le laboratoire.

J'ai aussi profité de l'humour de Bernard et des qualités de Marie-Jo. Je remercie Christophe Marcenat pour avoir partagé un peu de sa connaissance de la technique de calorimétrie alternative. Un grand merci aussi à Jean-Luc pour sa disponibilité et sa bienveillance quasi permanente, et aux électroniciens, Pierre et Frédéric. Je salue également Michel, qui a permis de résoudre bien des problèmes techniques.

J'ai passé d'excellents moments à l'ILL à compter les neutrons avec Béatrice, Eric, Louis-Pierre, Justin, Nicolas et en particulier Frédéric et Stéphane. C'était aussi un plaisir de travailler avec Ilya au LNCMI.

Je remercie les visiteurs du labo que j'ai beaucoup aimé rencontrer : Slavo et Samir qui ont partagé leur bureau avec moi, Rikio Settai for showing me the pressure cell setup at the level of Art as well as for nice Ski-Day, Hisashi Kotegawa for his great contribution to the football tournament as well as for our fruitful scientific teamwork, Sergey for his good mood and in anticipation of our future collaboration, Rena for my first Thanksgiving....

Merci à Vladimir, Vincent, Manuel, Driss, Mike pour leur aide théorique précieuse, et également Raphael, Florence, Pierre-Eric pour les excellentes soirées.

J'ai également eu la chance de rencontrer Frédéric Hardy que je remercie pour son soutien et ses conseils, ainsi que William Knafo, Christoph Meingast, Hermann Suderow, Tateiwa... and also the group of Stephen Julian with Fazel, Ming, Boris, Aaron, Dan : I keep an excellent souvenir of my stay in Toronto.

Je remercie également Marielle pour avoir géré toutes les demandes de HNO et de missions dans la joie et la bonne humeur.

J'ai eu la chance d'enseigner à l'université de Chambery et d'Annecy. Je remercie mes étudiants et mes collègues enseignants, Christian Lecot, Christophe Raffalli, Khalil Tawbeh et surtout mon tuteur Christophe Bonjour. Je remercie aussi Alexia Gorecki et Pierre Aldebert avec qui j'ai beaucoup aimé enseigner dans la classe passerelle du lycée Stendhal de Grenoble.

Je regrette déjà la présence de mes amis thésards, post-docs et stagiaires, avec lesquels j'ai partagé tous les bons moments de la thèse : Elena, qui me tire vers le haut dans tous les domaines und für alle Diskussionen, Ludovic, pour les moments vin-physique-fromage, Amalia, la plus jolie de mes co-bureau (Samir et Slavo me pardonneront), Tristan, témoin de mes exploits comme de mes bêtises, I thank Liam Malone for his careful reading of the thesis, frequent and interesting discussions about physics, beers and watching football..., Alexandre, LE gardien de but, et aussi Mathieu, Johnathan, Giorgios, Guillaume, Alexandra, Mounir, Xavier, Benoit et Benoit, Byron, Claude, Thomas, Charlène, Audrey, Silvano, Mario, Eduardo, Pana, Zoltan, Massimo, Eva...

Enfin, je remercie les membres de ma famille qui m'ont toujours soutenu et je dédie cette thèse à Hai sans qui je n'aurai pas pu faire cette thèse.

Contents

Abstract

In this thesis, the study on the superconducting ferromagnet UGe_2 is presented. Crystal growth of UGe_2 single crystals was realized in a tetra-arc furnace using the Czochralski technique. This technique was also used to obtain high quality single crystals of other uranium compounds, notably UCoGe and URu_2Si_2. The Curie temperature of UGe_2 ($T_{\mathrm{Curie}} = 53$ K) decreases with pressure and is suppressed at $p_c = 1.5$ GPa. Before being suppressed, the ferromagnetic transition changes from second to first order at a tricritical point. Precise resistivity and Hall resistivity measurements under pressure and magnetic field revealed the position of the tricritical point as well as its evolution under magnetic field which draw a wing structure phase diagram. Despite the theoretical prediction that this diagram is general for a ferromagnet, here we present the first experimental observation. Other measurements focus on the superconductivity ($T_{sc} = 0.75$ K) which coexists with ferromagnetism under pressure. The bulk nature of the superconductivity is investigated by AC calorimetry measurements under pressure. The attention is turned to the interesting phenomenon of field enhanced superconductivity.

Résumé

Cette thèse porte sur l'étude du composé supraconducteur ferromagnétique UGe_2. La croissance de monocristaux de UGe_2 a été réalisée dans un four tétra-arc par la technique du tirage Czochralski. Cette technique a également servi à l'obtention d'autres composés à base d'uranium, notamment UCoGe et URu_2Si_2. Pour la première fois, la structure avec des ailes (wings) du diagramme de phase de UGe_2 a été vérifiée expérimentalement. Cette observation est une conséquence d'une température de transition ferromagnétique qui décroît par application d'un paramètre extérieur tel que la pression, et qui devient du premier ordre avant de disparaître. Le changement d'ordre se fait à un point tricritique. D'autres mesures ont porté sur la transition supraconductrice qui se produit à l'intérieur de la phase ferromagnétique. La nature volumique de la supraconductivité a été confirmée et l'accent s'est porté sur son renforcement sous champ magnétique.

Chapter 1

General Introduction[1]

As early as in primary school, we learn that matter exists in three states : solid, liquid and gas. For example, we are taught that water boils at 100 ° C and freezes at 0 ° C. Later, we discover that evaporation can cool. Thus, our body is cooled down by the evaporation of sweat. And reciprocally, condensation releases heat : dewdrops that condense on flowers in the morning can prevent flowers from freezing. These familiar phenomena were however only understood in the 19$^{\text{th}}$ century with the birth of the science of the states of matter and thermodynamics.

Rapidly, the situation became very rich : the growth of metallurgy industry made possible new discoveries of transitions between different states of solids. Then, magnetic transitions were observed between states called paramagnetic and ferromagnetic or antiferromagnetic. At the beginning of the 20$^{\text{th}}$ century appeared the extraordinary phenomenon of superconductivity, later of superfluidity....

The physical properties of these states are far from being completely understood, although they have already a wide diversity of applications. Superconductors are used in medical devices (magnetic resonance imaging MRI), radiocommunication antennas, power applications (transmission lines, fault current limiters, magnetic energy storage), magnetic levitation train.... Ferromagnetic layers have a giant magnetoresistiance (GMR) which is used in read heads of hard disk, in data storage, in sensors.... Multiferroics are also promising materials for electronic device applications. It becomes apparent that these physical properties arise from a coupling between magnetic and electronic interactions.

In this context, uranium compounds are in a regime where magnetic and electronic interations are strongly coupled. They have several ground states (paramagnetic, ferromagnetic, antiferromagnetic, superconducting, hidden order...) and can change from one state to the other by changing the temperature, the pressure, the magnetic field.... The compound UGe_2 is the first material discovered where superconductivity coexists with homogeneous ferromagnetism.

The large diversity of ground states and phases transitions can be classified. Paul Ehrenfest proposed to distinguish the phase transitions with latent heat, i.e. that release or absorb heat (such as the solidification or evaporation), and phase transitions without latent heat (for example from paramagnetic to ferromagnetic). Later, Lev Davidovich Landau noticed that a change of symmetry accompanies phase transitions without latent heat[2]. Physics textbooks often consider the case of a magnet as an example. Above the transition temperature (Curie temperature), the magnetization is zero. The system has a high symmetry. Below the Curie temperature, a spontaneous magnetization appears with a particular orientation and direction (the magnet has a North and a South). The symmetry of the system is lower : there has been a **symmetry breaking** which manifests as a magnetic **order**.

[1] This introduction is inspired from [Papon02, Coleman05, Belitz07] in which more details can be found.

[2] A transition with latent heat can be accompagnied by a change of symmetry (such as the solid liquid transition of water) or not (liquid gas transition).

As has been highlighted by Landau, symmetry cannot change gradually. A symmetry element is either present or either missing. It cannot develop smoothly. This means, for example, that it is not possible to change continuously from a solid phase to a liquid phase. Landau associated the symmetry breaking to the concept of an **order parameter**. The order parameter is a variable null in the higher symmetry phase and finite in the lower symmetry phase. For example in the case of a magnet, the order parameter is the magnetization. The introduction of this new parameter modifies the expression of the thermodynamic potential G of the system. Landau supposed that the stable state is obtained by the minimization of the potential by respect to the order parameter. In the case of a magnet, the shape of the thermodynamic potential G is illustrated on fig. 1.1. We can see that above the Curie temperature T_C, the system has zero magnetization ; and below T_C, the magnetization is finite. To know the order parameter is thus to know what characterizes the ordered phase, but also to start to understand why the system undergoes a phase transition.

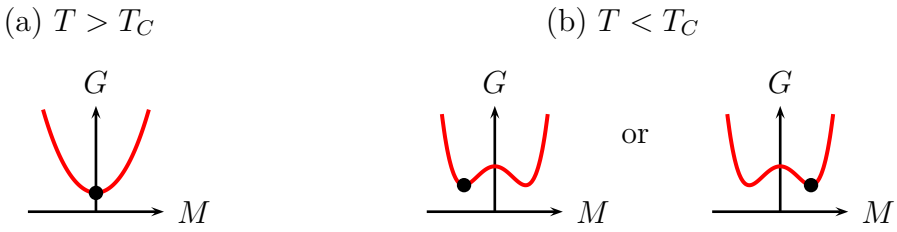

Figure 1.1: (a) $T > T_C$: the stable state is shown as a black dot and correspond to zero magnetization. The phase is not ordered and has a higher symmetry. (b) $T < T_C$: the system is in one of the stable state (black dots), the magnetization is finite with two possible directions. The phase is ordered and there has been a symmetry breaking.

In the case of ice, the ordered arrangement of molecules is sustained although there exists thermal motion of the molecules. At a certain temperature, the thermal energy is too high and the ice melts. Approaching a phase transition, short lived droplets of thermal fluctuations of order grow inside the material. In the case of a continuous phase transition such as from paramagnetic to ferromagnetic, the transition is **critical** : the droplets are of all sizes at the critical point. It means that the description of the system is independant of the considered scale. This description cannot explain a transition at zero temperature : in classical physics, no motion exist at 0 K, so that the system cannot leave its ordered states. However, if you have ever been skiing or skating on ice, you can appreciate the fact that the melting temperature of ice is reduced by the pressure. If one could pressurize ice enough so that the transition occurs at 0 K, one would have a phase transition at 0 K : a quantum phase transition. In the case of a second order transition, the critical state is called a **quantum critical point** (QCP).

Phase transitions at 0 K are possible when considering quantum mechanics. According to Heisenberg's uncertainty principle, quantum fluctuations exists at 0 K. Thus a new kind of phase transition can be driven not by thermal motion, but by the quantum fluctuations. John Hertz was fascinated by the question of how critical phenomena might be altered by quantum mechanics. Applying quantum mechanics to phase transition turns out to be very like Einstein's relativistic unification of space-time. A time dimension is included in the droplet of nascent order. The dimension is thus higher, which led Hertz to predict that the quantum ferromagnetic transition in metals should be of second order, and described by Landau theory.

In this study, I will present the phase diagram of UGe_2 in the pressure, temperature, magnetic field space. It will be shown that this phase diagram has a "wing" structure which is a direct consequence of the fact that the quantum ferromagnetic transition is of first order. This experimental observation reveals a new discrepancy to the theory.

In the past several decades other discrepancies have indeed been revealed especially in the low temperature dependences of the physical quantity such as the resistivity, the susceptibility, the specific heat. There are many discrepansies between theories and experiments. Some theories try to add the complexity of the materials into Hertz theory. Some others modify the original Hertz's approximations. Finally, some others believe that there is a true crisis that requires a new framework (see [Coleman05]).

1.1 Hill Plot of Uranium Compounds

The study of uranium compounds is motivated by the fact that some electrons of the uranium atom, the 5f electrons, simultaneously have magnetic properties (usually associated with localized electrons) and yet are close to being delocalized, i.e. to carry current through the metal. Thus, even if it requires very low temperatures, the study of these materials is important for understanding the electronic properties of solids.

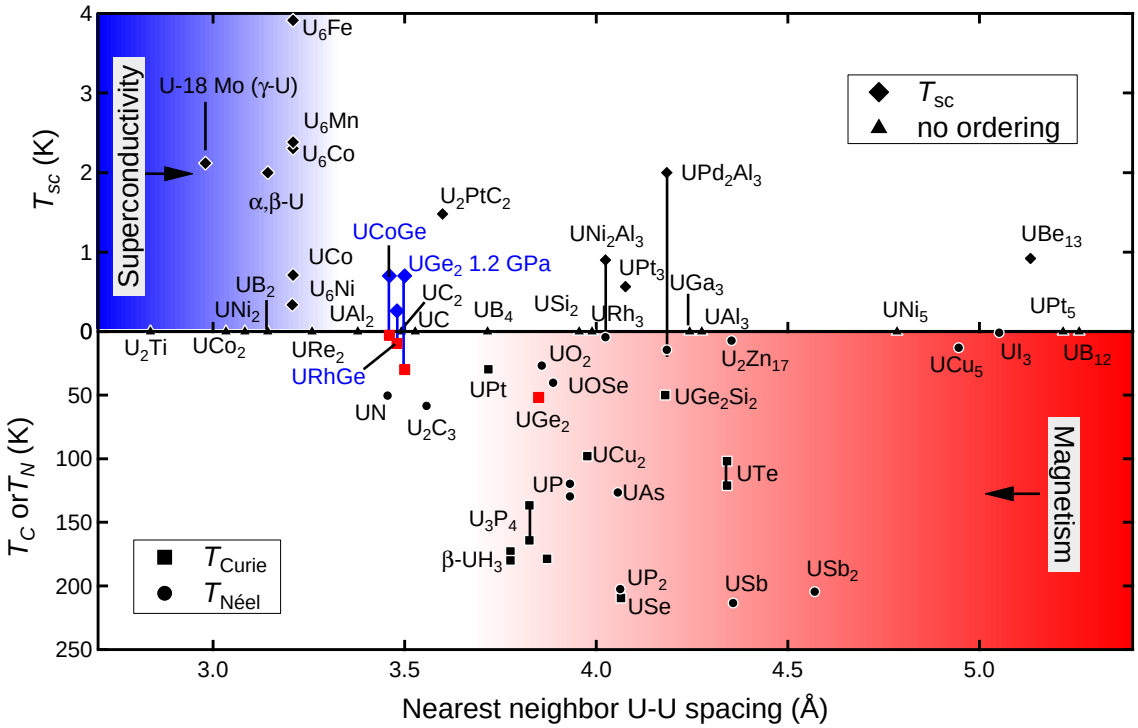

Figure 1.2: Hill plot for uranium compounds. Modified from [Hill70] and [Aoki00].

In most of the uranium compounds, the degree of overlap between the f electron wave functions is key to the ultimate collective ground state. Fig. 1.2 shows a so-called Hill plot for uranium compounds [Hill70]. Superconducting or magnetic transition temperatures are plotted vertically, and the spacing between f electron elements (uranium atoms) is plotted horizontally. Most compounds fall into two clear regions : large spacing with magnetism and short spacing with superconductivity. Hill conjectured that the overlap of the f electron wave functions between the uranium atoms determines whether the

f electrons are localized (magnetic) or itinerant (superconducting) independent of the intervening atoms. Most compounds behave as Hill outlined.

1.2 Magnetism and superconductivity

The fig. 1.2 exemplifies the antagonism between magnetism and conventional superconductivity, since these two phenomena are separated in two regions. The BCS theory (Bardeen Cooper Schrieffer) is successful at explaining the properties of most superconductors. The electrons team up to form pairs, known as Cooper pairs, due to interactions with the crystal lattice vibrations (phonons) at low temperatures. Electrons in these Cooper pairs have opposite spins. The early experimental studies showed that a small amount of magnetic impurities in a superconducting material reduces the superconducting transition temperature T_{sc} to 0 K [Matthias58]. It has been then theoretically demonstrated that the spin of the magnetic impurity acts as pair breaking for the formation of spin up-spin down Cooper pairs [Abrikosov61, Skalski64].

In the late seventies, the interest was attracted on compounds with a lattice of magnetic ions (RE)Mo_6S_8 (or (RE)Mo_6Se_8) and (RE)Rh_4B_4, where RE is a rare earth element. The two most studied cases are $ErRh_4B_4$ and $HoMo_6S_8$. In these compounds, superconductivity disappears when ferromagnetism appears below $T_{\text{Curie}} < T_{sc}$. Moreover, superconductivity coexists with a long range magnetic order in a small temperature range $T_{\text{Curie}} < T < T_m$. The magnetic order is not ferromagnetic but is with a period $d < \xi$ (the superconducting coherence lenght) but large by comparison to the interatomic distance. Therefore, the magnetic field is null on the size of ξ (see [Fischer90] for a review).

The coexistence of superconductivity with antiferromagnetism order is possible for compounds that have a superconducting coherence length much larger than the magnetic unit cell dimension [Flouquet02]. Moreover, the pair breaking due to spin-flip scattering by flipping the spin of a single magnetic ion is no longer a possibility in an antiferromagnet. The (RE)Ni_2B_2C family presents examples of co-existence of antiferromagnetism and superconductivity [Bud'ko06]. Interestingly, the coexistence of weak ferromagnetism and superconductivity was observed in $ErNi_2B_2C$ [Canfield96]. The internal field associated with the small ferromagnetic component is not sufficient to destroy the superconductivity.

In addition to the effect of magnetic impurity, a magnetic field can destroy singlet superconductivity in two ways. The first of these effects is known as the orbital effect and is simply a manifestation of the Lorentz force. Since the electrons in the Cooper pair have opposite momenta, the Lorentz force acts in opposing directions and the pair breaks up. The second phenomenon, known as the paramagnetic effect, occurs when a strong magnetic field attempts to align the spins of both the electrons along the field direction [Flouquet02]. This last effect does not break triplet superconductivity in which both electrons may point in the same direction as the field.

In the recently discovered superconducting ferromagnets UGe_2 [Saxena00], URhGe [Aoki01] and UCoGe [Huy07], there is also coexistence of ferromagnetism and superconductivity. The novelty is that the electrons responsible for the ferromagnetic order are believed to be the same as those which participate in the formation of Cooper pairs. Their Curie temperature is much higher than the critical superconducting temperature. In UGe_2 and URhGe, the superconductivity exists only in the presence of ferromagnetism. These compounds belong to the familly of heavy fermion.

1.3 Heavy Fermions

The Hill plot should be taken cautiously since the principal control parameter is not the U-U spacing, but hybridization of the 5f states with electronic states of other components. The heavy fermions superconductors are exceptions in the Hill plot. For example UBe_{13} or UPt_3 have a fairly large spacing between the uranium atoms, although the f electrons are not fully localized and even condense into the superconducting state. Also, the heavy fermions UNi_2Al_3 and UPd_2Al_3 show coexistence of superconductivity and antiferromagnetism. Even more surprising are the superconducting ferromagnets UGe_2, URhGe and UCoGe. These compounds are in the critical region of the Hill plot with respect to the U-U spacing, between the magnetic and the superconducting compounds.

Many studies have been performed in cerium compounds which show similar properties : the 4f electrons in cerium are rather localized but interact strongly with the 5d-6s conduction electrons. This is due to the spatial extension of the radial charge density of the 4f shell which overlaps with the maximum radial density of the 5d-6s shell, leading to hybridization. Many cerium compounds shows a "heavy fermion" character where a local behavior is observed at high temperature and a itinerant behavior is observed at low temperature.

1.3.1 High temperature regime, single impurity behavior

In the high temperature regime, the 4f electrons can be considered as localized magnetic impurities. Kondo found that the spin of the conduction electrons interact antiferromagnetically with the spin of the magnetic impurities to form a Kondo singlet. Therefore, the conductions electrons are less free for electrical conductivity and the resistivity increases with decreasing temperature. At the same time, the spin of the magnetic impurities is quenched by the spin of the conduction electrons. The increase of the resistivity with decreasing temperature is illustrated in fig. 1.3 for the compound $LaCu_6$. A small amount of magnetic impurities such as Ce atoms instead of La induces the Kondo effect. This remains observable at high temperature in the pure compounds $CeCu_6$, where the 4f electrons of Ce constitute a lattice.

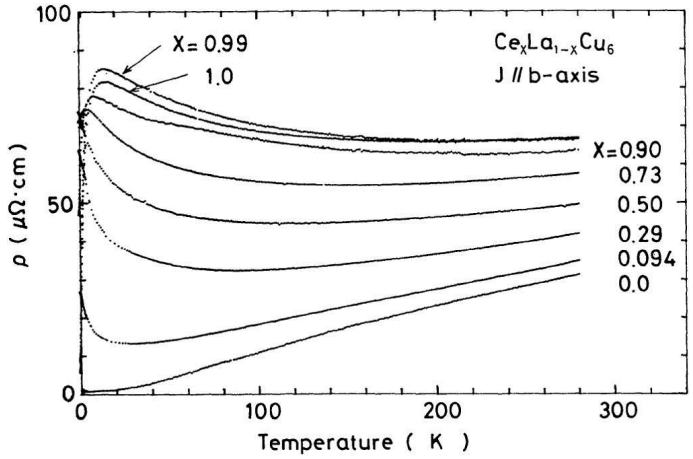

Figure 1.3: Resistivity of $Ce_xLa_{1-x}Cu_6$ [Sumiyama86]. In $LaCu_6$ ($x = 0$) the resistivity decreases as the temperature decreases. For $x = 0,094$, magnetic impurities gives rise to the Kondo effect. For $x > 0,7$, coherence effects appear.

1.3.2 Low temperature regime, Kondo lattice

In the low temperature regime, also called coherent regime, the electronic properties can be described by very heavy quasiparticules with effective mass as much as 1000 times the free electron mass m_0. These heavy masses account for the inertia of the electrons due to the strong interactions. The coherent regime is directly related to the density of Ce atoms in the compound : in fig. 1.4, the coherent regime revealed by a decrease of the resistivity with decreasing temperature is observed when the number of impurity is large ($x > 0.7$ in the case of $Ce_xLa_{1-x}Cu_6$).

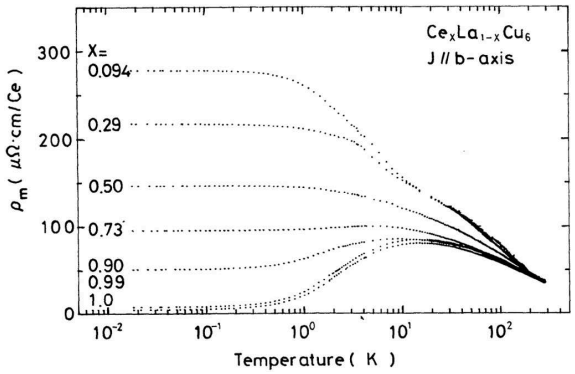

Figure 1.4: Resistivity of $Ce_xLa_{1-x}Cu_6$ [Sumiyama86]. When the number of impurity becomes large ($x > 0.7$), coherence effects appear, and a Fermi liquid regime is observed.

Fig. 1.5, shows the effective radial charge density of the uranium atom, which is compared to those of nickel or cerium atoms. The spatial extension of the 5f electrons of uranium compounds is larger than the 4f of cerium, so that their itinerant character is stronger. They can be regarded as intermediate between 3d and 4f cases. In addition, this higher radial extension increases the spin orbit coupling. These differences with cerium compounds gives uranium compounds a wider variety of magnetic behavior. The proximity of these elements to the boundary between the localized and itinerant character of the 5f electronic states makes them very sensitive to variations of the environment.

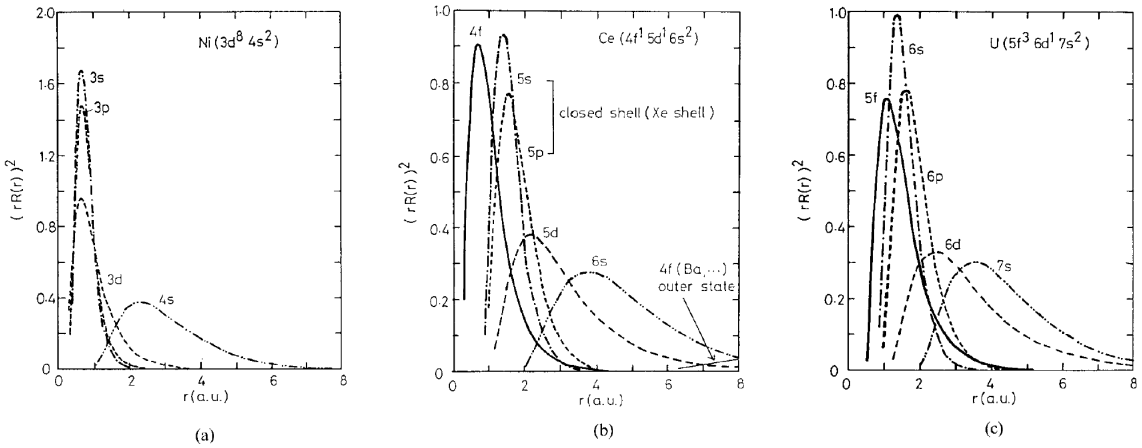

Figure 1.5: Effective radial charge densities of (a) Ni, (b) Ce and (c) U atoms. Taken from [Aoki00].

1.4 Plan of this Thesis

In order to study these compounds, high quality single crystals are required. Around 50% of my work was done on the sample preparation. It was time consuming work,

but necessary. It appears to be very exciting for different reasons. First, the sample preparation is the starting point of all the experiments so that it is a good way to be involved into several parts of the physics. Second, there are lots of examples of lucky discovery in the history of condensed matter physics, associated with the growth and preparation of new materials and samples. Third, many techniques are required to create and characterize research samples, making the work diversified. These techniques are presented in chapter 2.

All the single crystals have been grown by the Czochralski technique. As the story goes [Tomaszewski02][3], the young Jan Czochralski was studying the crystallization of metals. A crucible containing molten tin was left on his table for slow cooling and crystallization. Czochralski was preparing his notes on the experiments carried out during the day when at some point, lost in thought, he dipped his pen into this crucible instead of inkwell placed nearby the crucible. He withdrew it quickly and saw a thin thread of solidified metal hanging at the tip of the nib. The discovery was made! He had generated a nucleation point for crystallization by putting the cold tip into the melt and extracted a crystal by pulling it from the surface of the melt. Careful observation of this accidental process provided a discovery of great importance. "Chance favors the prepared mind"[4]. The Czochralski technique have been successful in obtaining new samples of uranium compounds which have permit other researcher in the laboratory to obtain new results.

I have performed new measurements on single crystals of UGe_2. The current state of research on UGe_2 is presented in chapter 3. It is a very interesting material since the superconductivity coexists with the ferromagnetism. Moreover, the ferromagnetism is suppressed with pressure but the transition becomes first order before occuring at 0 K.

Details of this ferromagnetic transition are presented in chapter 4. A line of critical points in the p-T-H space has been detected experimentally. It will be explained that this line is a direct consequence of the fact that the transition to the ferromagnetic state becomes first order. This critical line will reach the $T = 0$ K plane and a new class of quantum criticality is expected. This is the main result of this study. A brief presentation of the theories will be done. When possible, qualitative comparison between some theories and the experimental results is made.

Finally, new measurements on the superconducting phase have been performed and are presented in chapter 5. The bulk nature of the superconductivity is confirmed on single crystals. For the first time, a magnetic field enhancement of the superconductivity is observed with a bulk probe.

[3] I am always curious of that kind of story. The ref. [Tomaszewski02] gives [Czochralski16, Czochralski25] as references for this story. Pr. Pawel Tomaszewski kindly sent me a copy of [Czochralski25] and mentioned that he could not find [Czochralski16]. He also sent me the ref. [Czochralski18]. I noticed to Pr. Tomaszewski, that no such story is mentioned in [Czochralski18, Czochralski25]. He replied that the details of this story are published only in polish. Since I was not doing a PhD in history of science, I stopped here my investigation!

[4] Citation generally attributed to Louis Pasteur.

Chapter 2

Experimental Technique

2.1 Sample Preparation

2.1.1 Material Preparation

During this study, single crystals of uranium based compounds have been grown, such as URu_2Si_2, UCoGe, UGe_2, $UCoSi_2$, UNi_2Al_3.... They have been obtained from the Czochralski technique which is described in section 2.1.2. In this technique, particular attention is given to the starting materials in order to be as close as possible to the stoichiometric conditions. In this study, UGe_2 and URu_2Si_2 single crystals have been obtained in very high quality by starting from the stoichiometric ratio. This is certainly because their solidification is a congruent reaction. A congruent reaction is an isothermal reversible reaction in which both of the phases concerned have the same composition throughout the process. This is the case for the solidification of UGe_2 as can be seen on the phase diagram fig. 2.1. When it is not congruent, the knowledge of the phase diagram can allow one to speculate the off-stoichiometric starting composition to obtain single crystals. For example, single crystals of USi_3 can be obtained from the Czochralski technique by starting from a melt of $USi_{4.6}$ [Tokiwa00]. However, such a phase diagram does not yet exist in the case of uranium ternary alloys. Previous work on URhGe indicate that the diagram is more complicated. High quality single crystals of URhGe can be obtained only with an initial excess of Ge [Levy06]. Therefore, it is sometimes necessary to start with a composition slightly off-stoichiometric.

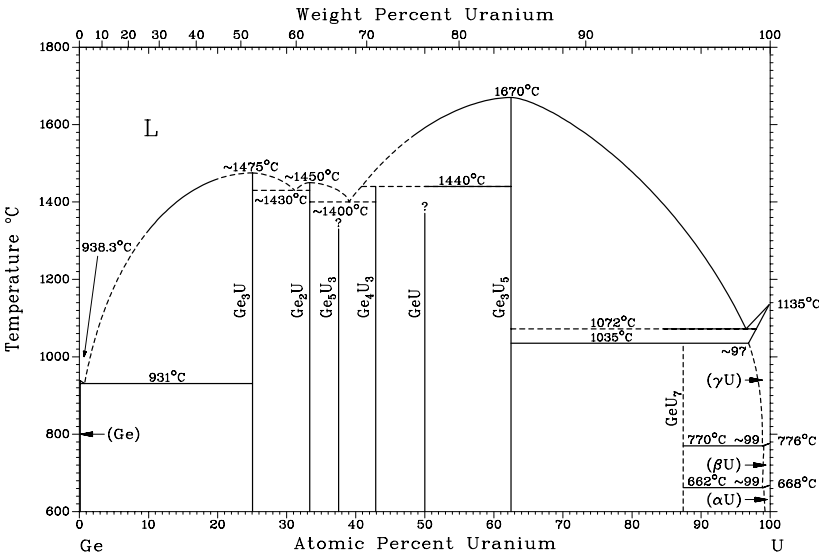

Figure 2.1: Binary phase diagram of Ge-U from ASM international database.

Note that I restrict the discussion to the Czochralski technique for which a congruent melt is suitable, but there exists many crystal growth techniques such as flux method, chemical transport method, Bridgman technique, zone melting....

The starting materials have to be as pure as possible, in the limit of commercial availability and cost.

The uranium we used is depleted uranium (mostly ^{238}U with 0.2% of ^{235}U) assumed to be pure at 99.9% (3N). It is available as solid bars which are oxidized and have a black color (country of origin : France). The first step is to cut the bar by electro-erosion (see 2.1.5) to obtain the amount of uranium we want to use for the growth (around $4-6$ g). Then, the oxidation is removed by electro-etching. Uranium is put into a mixture of 95% acetic acid and 5% perchloric acid. 12 V DC is applied between the uranium (anode) and a stainless steel plate (cathode). The uranium then has a shiny metallic surface. It is kept under acetone until it is placed into the furnace (usually less than 20 minutes). This process of electro-etching is also useful to adjust precisely the mass of uranium.

Rhodium or ruthenium (99.99% : 4N) are bought in powder form. With an arc furnace, it is impossible to start from powder since the arc discharge would blow the powder everywhere. For an induction furnace, the crucible has some slits and cannot contain a powder. Thus, we first create pellet by applying pressure. The pellet is then degassed under high vacuum (10^{-6} torr) and melted with arc discharge.

The cobalt (3N) is purified by etching. It is emersed for $30-60$ seconds in a 85 $^{\circ}$C melt of 30% nitric acid, 10% sulfuric acid, 10% phosphoric acid and 50% acetic acid. Sometimes, a pink color remains on the surface, it is removed using a melt of 50% hot water and 50% nitric acid.

Silicon and germanium (6N) are bought in very high purity pieces which are selected to obtain the correct mass.

The typical total mass of materials is around $6-10$ g.

2.1.2 Crystal Growth in a Tetra-Arc Furnace

Once the high purity elemental starting materials are ready, they have to be melted. Different techniques are possible such as induction heating, arc-melting.... At the beginning of my work in the laboratory, a tetra-arc furnace was bought and set up. It was done with the help of Gerard Lapertot, Christophe Marin, Karine Mony, Dai Aoki and mainly T. Komatsubara and M. Suzuki. After growth of a non radioactive material $CeRh_2Si_2$, the growth of uranium compounds began. After the first growth of URu_2Si_2, the Radio Protection Service (SPR) checked the contamination of the furnace and of the material used to clean it, and it was confirmed that we could work safely.

Polycrystal Growth

The materials are put on a copper crucible, and degassed under high vacuum (10^{-6} Torr). Then, the water circulation is activated to cool down the copper crucible, the tips, the seed-holder and the furnace chamber. The chamber is filled in purified argon atmosphere[1]. The arc discharge is then created taking care that its position is above a metal (Uranium, Rhodium, Ruthenium, Cobalt...) and not a semiconductor (Silicium, Germanium...). Indeed, the electrical current flows through the tip, the Argon plasma, the metal and the copper crucible.

Then the crucible can be rotated to improve the homogeneity. However, the bottom part which lies directly on the water cooled crucible remains solid and does not mix

[1]The purity is so high that $O_2 < 10$ ppb, $H_2O < 20$ ppb, $CO+CO_2 < 50$ ppb, THC (as CH_4)< 50 ppb and $N_2 < 300$ ppb.

well. Thus, the arc discharges are stopped. The materials solidify and cool down in around 10 minutes. Then, the polycrystal is flipped upside down using a spoon. The use of a spoon requires a bit of dexterity, but its presence avoids openning the furnace and restarting the pumping process. After that, the polycrystal is again melted by arc discharge. This process is repeated 5 times.

The polycrystal is left to cool for more than 1 hour and then the furnace is opened and cleaned.

The polycrystal is weighed to estimate the loss of materials. Surprisingly, the mass increased for the first batch of polycrystals (less than 0.2%). This is certainly due to some dust which disappeared after successive pumping and cleaning processes. Now, the loss is around $0.2 - 0.3\%$ of the total mass.

Single Crystal Growth by the Czochralski Technique

Starting from a polycrystal, a single crystal can be obtained by the Czochralski technique [Czochralski18]. It consists of putting a tip in the melt, and pulling vertically (see fig. 2.2). Since the tip is cold, a solid crystal forms on it. The crystal then grows during the pulling and, with care, a single crystal can be obtained.

The typical pulling rate is $10 - 20$ mm per hour.

At the beginning, several grains can crystallize with different orientations. To limit their number, a necking is performed : the diameter of the crystal is reduced. Then, a single crystal can be grown with a bigger diameter.

To avoid strains due to the thermal contraction during cooling, a tail shape is realized before the end of the pulling (see fig. 2.3). This was particularly important for URhSi and $UCoSi_2$, which show a tendency to explode after the growth, during the cooling. Indeed, if the diameter of the single crystal is reduced abruptly, the cooling is faster, resulting in a larger thermal gradient.

2.1.3 High Temperature Annealing

The quality of the crystals can be improved by high temperature annealing, which can remove defects and internal strain. Two furnaces have been used.

With big single crystals, ultra high vacuum annealing using an induction furnace is possible. The crystal is put on an horizontal boat : a water cooled copper crucible. It is sealed in a quartz tube and pumped until ultra high vacuum (10^{-9} Torr)[2]. The crystals are heated to just below their melting point during typically 12 hours. This process was realized successfully by Dai Aoki on some crystals of UCoGe I prepared and selected according to their Laue diffraction. The RRR increased from 3 to 30, which is similar to the best report [Huy08, de Visser09].

Another possibility is to use an electrical furnace which can heat up to 1075 $^\circ$C under ultra high vacuum (10^{-10} Torr). As described previously, such vacuum is obtained with ion pump, but in this furnace, a air-lock allows to keep the main chamber always under vacuum (see fig. 2.6). The heating is performed during 5 to 20 days. This process was

[2]To obtain such vacuum, a membrane pump (which contain no oil) is used. From 1 Torr, a turbomolecular pump is used in series. From 10^{-5} Torr, a baking is realized by covering the tubes with electrical cables. The power in the cables is increased progressively. At 10^{-6} Torr, the baking is stopped and a ion pump is started. At 10^{-8} Torr the baking is restarted. Then, the pumping is performed together with heating the sample so that impurity at the sample surface are degassed. The vacuum is kept below 5×10^{-8} Torr. Then, the heating is stopped and 10^{-9} Torr is obtained.

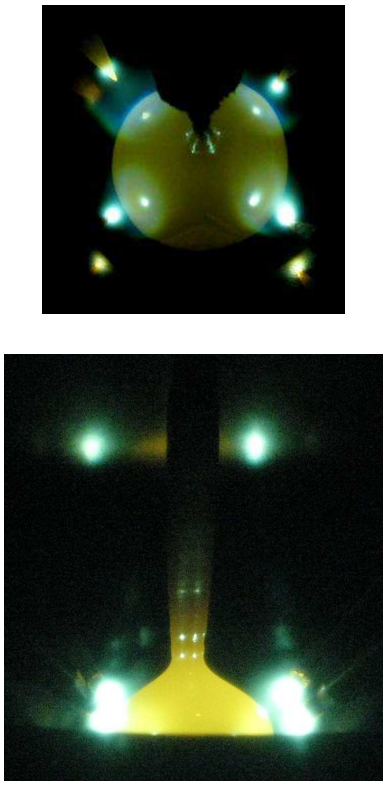

Figure 2.2: Crystal growth in a tetra arc furnace by the Czochralski technique.

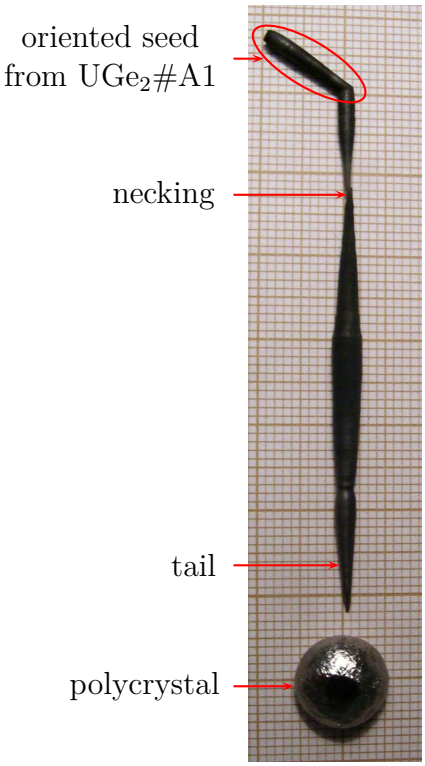

Figure 2.3: Crystal of UGe_2#A2 grown along the b axis using a seed from UGe_2#A1.

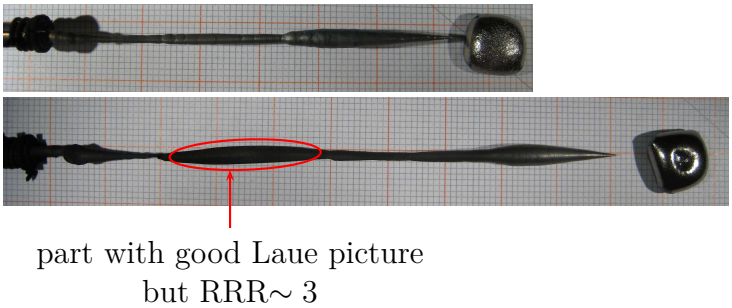

Figure 2.4: Crystals of UCoGe#A1 and #A2. The selected part was chosen from the Laue picture and a high temperature annealing was performed.

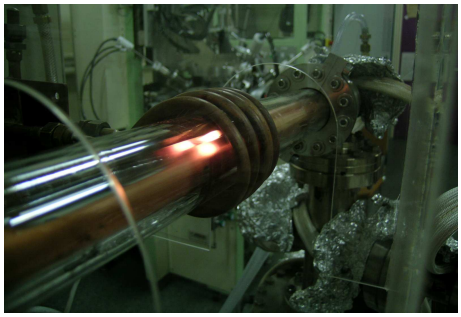

Figure 2.5: High temperature annealing of UCoGe for 12 hours just below the melting point ($\sim$ 1350 $^\circ$ C). The effect on the residual resistivity ratio is positive : the RRR increase from $\sim$ 3 to 30.

used for URu_2Si_2 (up to 1075 ˚C), UCoGe (850 ˚C), $UCoSi_2$ (1050 ˚C and 700 ˚C). For UGe_2, an attempt of 5 days at 900 ˚C reduced the quality, as well as a second attempt of 5 days at 850 ˚C. These conditions are however given in ref. [Yamamoto04], but the annealing may have opposite consequences if the defects arise from Ge inclusion or Ge vacancies. The Ge is indeed sensitive to high temperature high vacuum conditions since the vapor pressure of Ge is high.

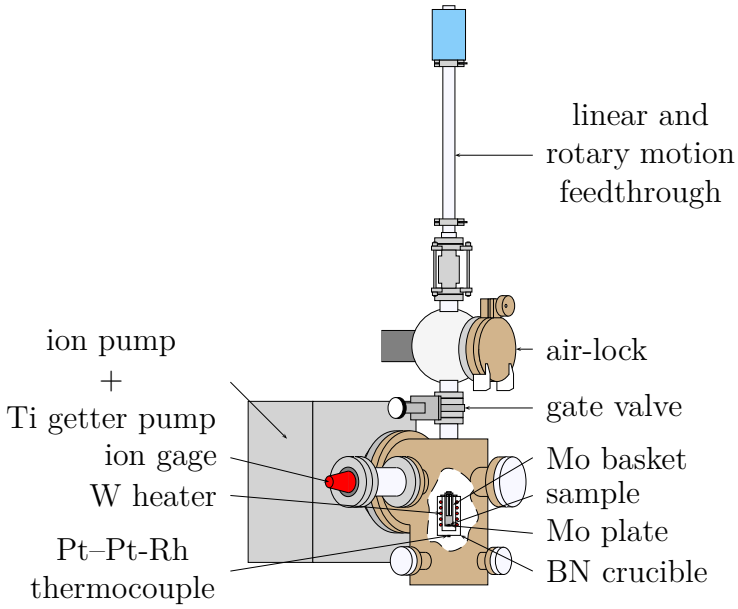

Figure 2.6: Scheme of the electrical furnace for high vacuum annealing. The sample is deposed on a plate in a molybdenium (Mo) basket. It is transfered from a air-lock to the heater crucible thanks to a linear motion feedthrough.

2.1.4 X-ray Laue Photograph

The X-ray Laue photograph is necessary to check the crystalinity of the sample, and to find the orientation before cutting. X-rays are generated from a W cathode and focussed by a feed through. The sample, which lies on a goniometer, diffracts the X-rays which give rise to a pattern on a film. Since the power of the generator is limited and that a photographic film is not sensitive, around 45 minutes are necessary to get a Laue pattern. Next, the film is developed in a dark room with developer and fixer. It is then dried.

At the beginning of this work, the X-ray generator and dark room were in the C5 building. A transport authorization was necessary to move radioactive materials from D5 (where they are grown) to C5. This was boring and time consuming. Thus, a new room was built in D5 into which the apparatus was moved. This lead a considerable improvement of efficiency. Recently, but I never used it, a CCD detector has been bought to replace the old fashion film and dark room technique. The time for obtaining one Laue photograph will reduce from 40 to $\sim$ 1 minute and no development and drying will be necessary.

The orientation is obtained thanks to a software developed in CNRS Grenoble : orientexpress.

In fig. 2.8, an example of the copy of the lab-book for the single crystal UGe_2#A3 is represented. It serves to follow the different X-ray Laue Photograph, Electro-Erosion

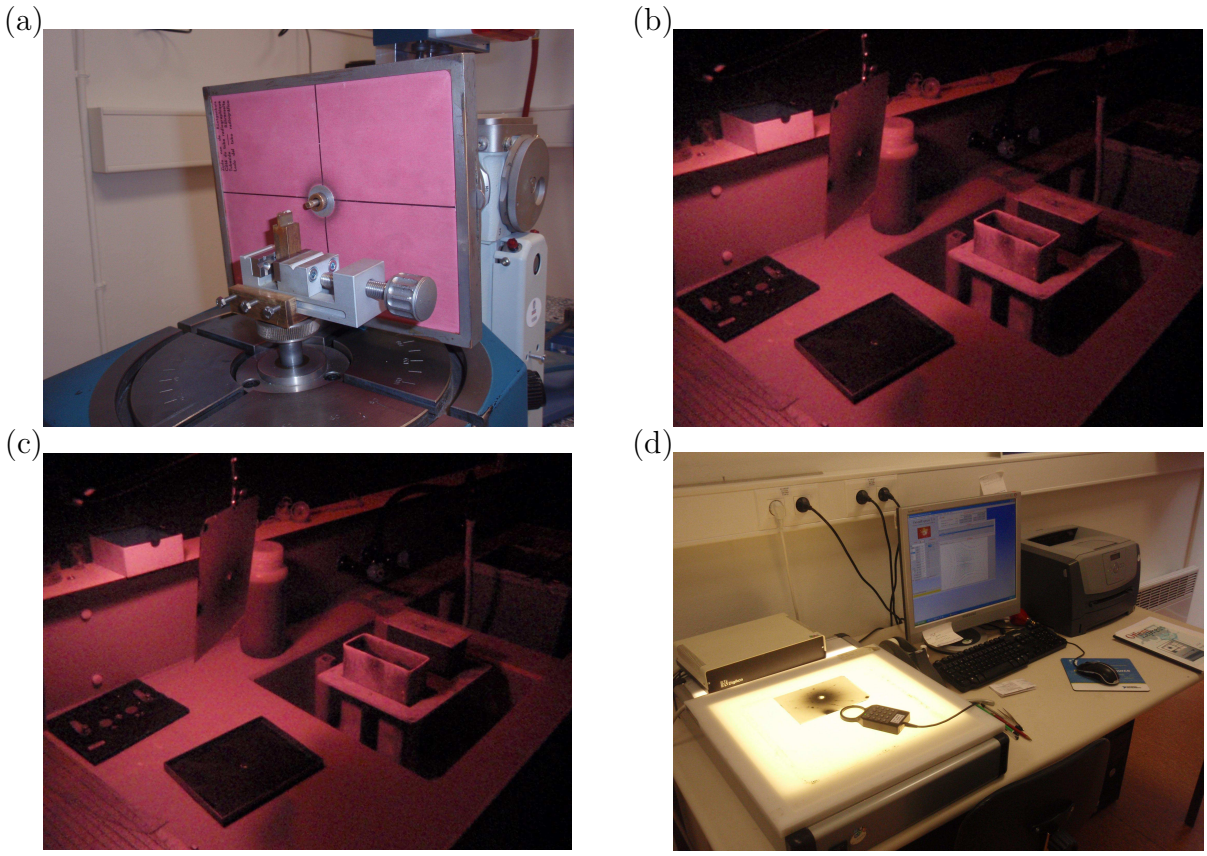

Figure 2.7: (a) X-ray experiment. (b) dark room with developer and fixer. (c). (d) digitizer table to identify the orientation with the software Orientexpress. The photographer for (a)(b)(d) is Tristan Combier.

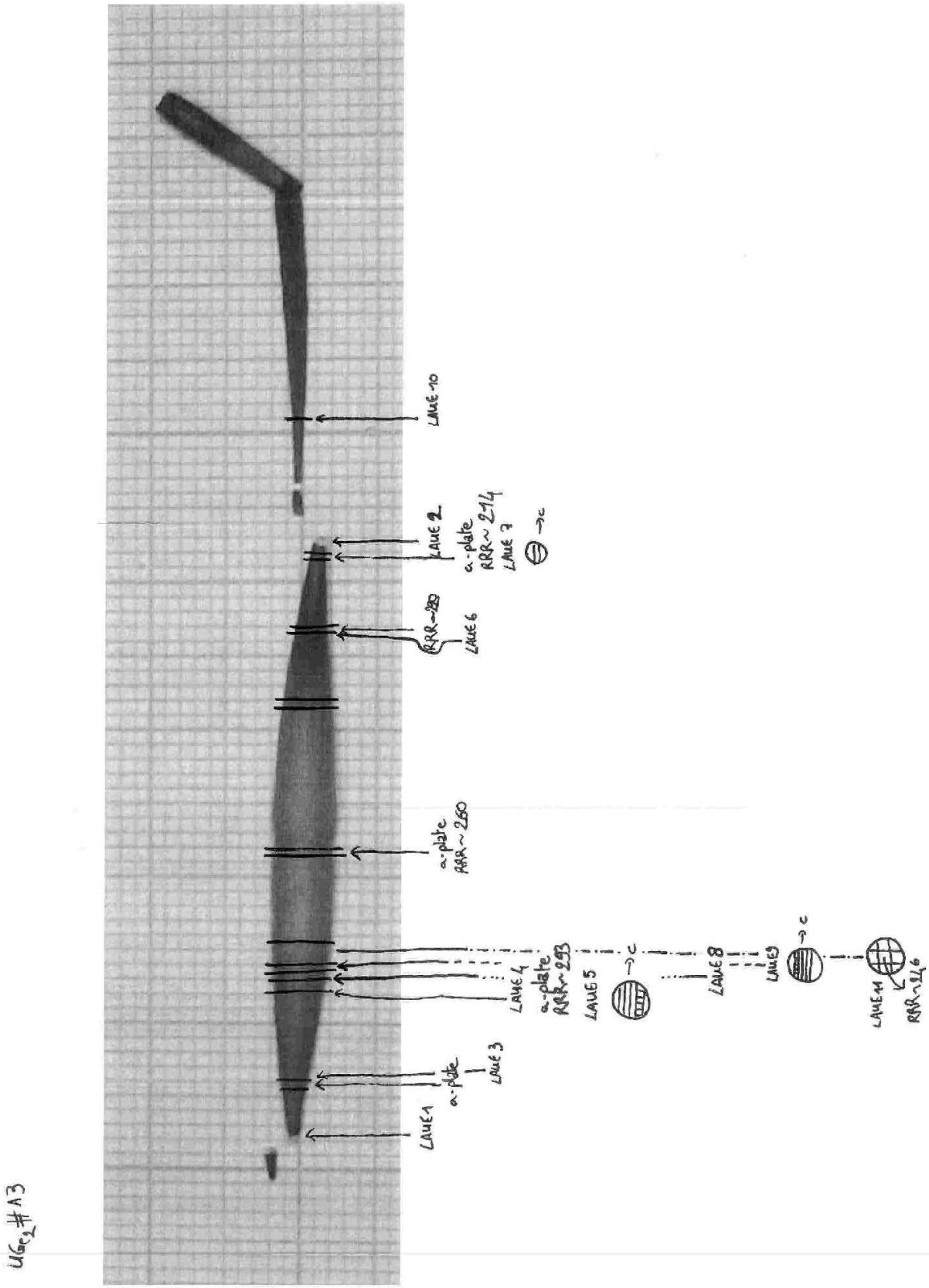

Figure 2.8: Copy of the lab book for UGe_2#A3 grown along the a axis using a seed from UGe_2#A1.

Cutting and RRR measurements at different parts of the ingot. In the case of UGe_3#A3 grown along the a axis, the quality of the crystal is very good for almost the whole ingot (RRR> 200) and the crystallinity remains good from the neck to the tail. It was not the case of UGe_2#A2 grown along the b axis. This indicates that the growth along the a axis is easier for this compounds, by comparison to the b axis. In UGe_2#A3, the quality increases when approaching the tail. Once the best part of the ingot is located, crystals are selected for different experiments.

2.1.5 Electro-Erosion Cutting

A goniometer with the sample mounted on it is placed in a oil bath. The sample is cut by electro-erosion with a copper wire whose electro potential can be set up to 100 or 300 V. The radioactive dust resulting from this cutting remain in the oil which is therefore contaminated. This spark-cutter is under a hood in a protected area room.

The copper wire, whose diameter is 50 μm, allows for the cutting of a slice with a width as small as $\sim$ 200 μm. Smaller sample widths are achieved by polishing (see section 2.1.6).

The copper wire is eroded as well as the sample during the cutting, but it is renewed thanks to a motor. During this study, I participated to add a relay to automatically stop the motor at the end of the cutting. This avoids the consumption of the (3N) copper wire, which is boring and wasteful.

2.1.6 Sample Polishing

The sample polishing requires careful manipulation, since it creates powder of radioactive materials. Thus, this process is realized in a hood under water. The water retains the powder, so that it cannot be inhaled.

Sample polishing is done to adjust the thickness of a sample to fit in pressure cells. I also polished a URu_2Si_2 sample (see fig. 2.9) to obtain two nice parallel faces in order to perform inelastic neutron scattering experiment with uniaxial pressure (measurements performed by Frédéric Bourdarot). For UGe_2, Stephane Raymond wanted to confirm, by X-ray scattering at ESRF, some results on the phonon spectrum previously obtained by neutron scattering [Raymond06]. It was not clear if a cleaved surface was better than a polished surface. I selected a cleaved sample with two plateaus and polished the upper plateau (see fig. 2.10). The experiment revealed no difference between the cleaved and the polished plateaus. The experiment was performed in reflexion, and the penetration depth is about 6 μm at 21.74 keV, which is approximatively the mean size of the sandpaper's particles. The results of this experiment on the phonon spectrum of UGe_2 are being analyzed by Stephane Raymond.

2.2 Low Temperatures

Different cryostats have been used in this study.

The thermal expansion measurements have been performed in He^4 cryostat designed for neutron measurements, often called a orange cryostat. The scheme of this cryostat is presented in fig. 2.11.

The other measurements were performed in a commercial Quantum Design cryostat PPMS. Different set ups (options) are available to measure resistivity or specific heat. It is also possible to use a He^3 cryostat to reach 0.4 K. The sample holder (puck) can be

Figure 2.9: URu_2Si_2 sample from growth #4. The left picture shows a c plane and the right one a polished a plane. This sample is prepared for an inelastic neutron scattering experiment under uniaxial pressure. The RRR is around 20 which is not very good for this material, but the rocking curve revealed only one grain, which is remarkable for such a big sample.

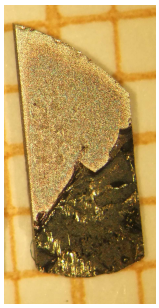

Figure 2.10: b plane of UGe_2. The sample has been cleaved, and the upper plateau has been polished. It has been used for X-ray at ESRF.

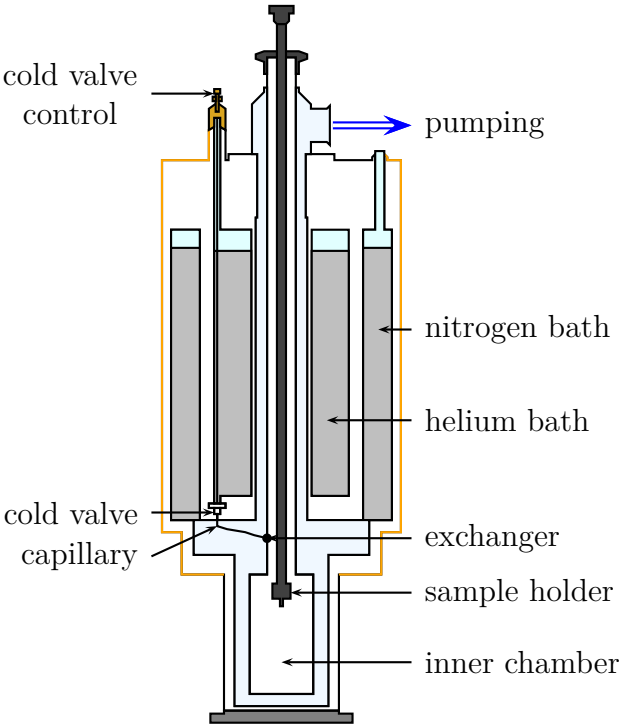

Figure 2.11: Simplified scheme of an orange cryostat. A liquid nitrogen bath at 77 K serves as a thermal screen. The cold valve allows regulation of the He^4 flux in a capillary which is pumped. The end of the capillary, which is a cold point, is in contact with the chamber containing exchange gas and the sample. A heater and thermometers (platinum and carbon resistors) lie on the exchanger. This type of cryostat was developed for the Institute Laue Langevin in 1975 by Dominique Brochier and Serge Pujol. The nitrogen bath and helium bath are not in the neutron beam. There is no copper, inox or superinsulator in the neutron beam. The part in the neutron beam is in aluminum which is transparent to neutrons in most cases. Since 1982, it is commercialized by Scientific Abingdon. It costs around 26000 euros.

modified to hold a pressure cell. It is also possible to use external electronics to measure AC calorimetry, or AC susceptibility.

Similarly, a commercial quantum design cryostat MPMS allows one to measure the magnetization. During this study, I collaborated with Rikio Settai and Tristan Combier to develop a pressure cell which can fit in a MPMS with pistons and anvils in zirconium oxide. The target was to measure the magnetization of UGe_2 under pressure above 1.5 GPa as in ref. [Tateiwa01a, Pfleiderer02] with a magnetic field to confirm the wing structure obtained by resistivity (see section 4.1). However, the availability of the MPMS and experimental hazards (broken piston) slowed the development and we were not able to perform this experiment.

Measurements under pressure below 2 K, were realized in He^4-He^3 dilution refrigerators down to 50 mK and at magnetic field up to 16 T. Depending on their availability or on their magnet, 3 dilution fridges have been used, with the help of Jean-Michel Martinod, Dai Aoki, or Georg Knebel at the beginning. High field measurements were also realized with a resitive magnet at LNCMI Grenoble up to 22 T in a dilution fridge with a plastic mixing chamber with Liam Malone.

2.3 High Pressure

Different kinds of pressure cells have been used, depending on the experimental requirements and the availability in the laboratory.

2.3.1 Piston Cylinder Cell

The use of the piston cylinder cell is the most common to produce a high hydrostatic pressure. The advantage of this type of cell is that it is rather simple to set up and that the pressure chamber is quite large (diameter 4-6 mm). These cells are thus useful for neutron scattering experiments[3] when big samples are required, or for thermal expansion measurements because of the large size of the strain gauges.

A scheme of the CuBe pressure cell used for the thermal expansion experiment on UGe_2 is presented on fig. 2.12. The one used for URu_2Si_2 was similar. This cell was designed by Georg Knebel in the laboratory. Other piston cylinder cells made from NiCrAl and CuBe have been used for other experiments up to 2 GPa.

The sample is in the pressure chamber, inside a Teflon cap, filled with a pressure transmitting medium. Usually, Daphne 7373 was used, but in case of neutron experiments, Fluorinert was used[4].

A leakproof way of the wire through the feed through is realized thanks to epoxy resin (Stycast 2850FT).

To determine the pressure, the superconducting transition temperature T_{sc} of lead is measured by AC susceptibility[5]. Indeed, T_{sc} of lead varies with pressure so that it can be used as a manometer [Bireckoven88]. Pressure steps as small as 0.01 GPa have been measured.

Piston cylinder pressure cell can reach 1.5-2 GPa. This value is fixed by the elastic

[3]CuBe is ideal for neutron scattering experiments : the transmitivity is more than 50%.

[4]Fluorinert does not contain hydrogen, so that it can be used in a neutron beam.

[5]It is also possible to measure the resistivity instead of the AC susceptibility, but it is more sensible to the pressure gradient since one filamentary path of superconductor is enough to observe zero resistivity.

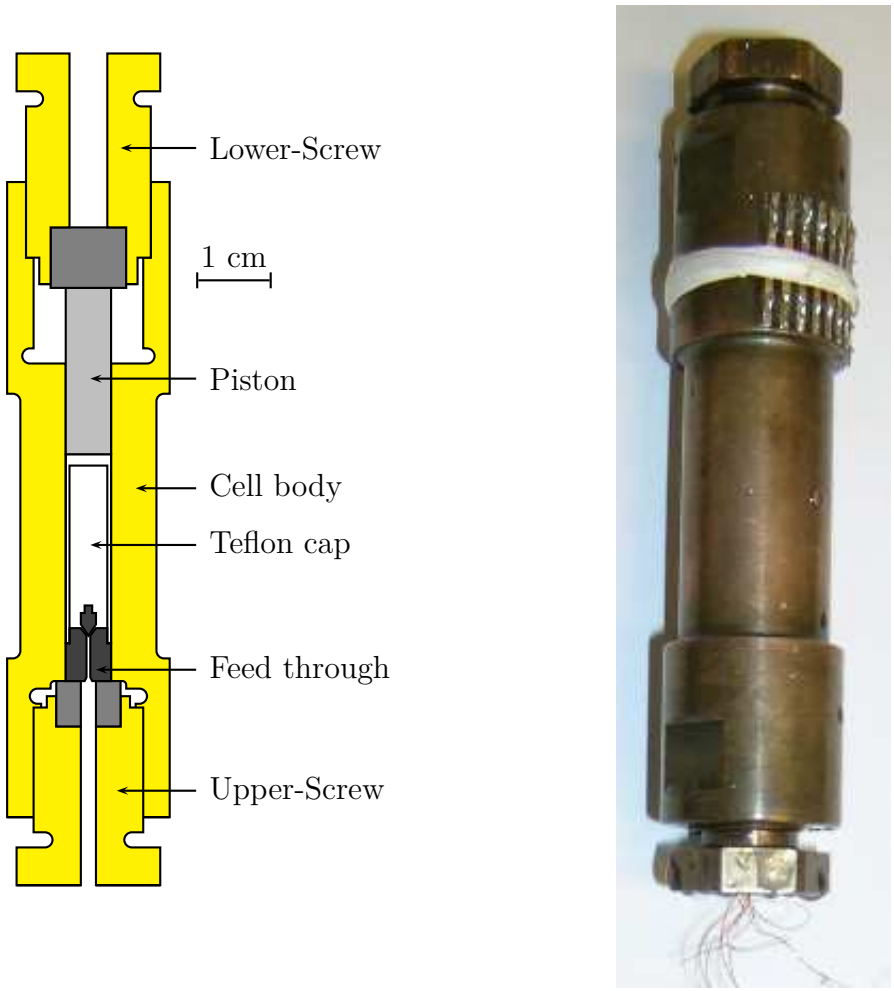

Figure 2.12: Piston cylinder cell used for thermal expansion on UGe_2 [Taufour11, Hardy09]. The cell used for URu_2Si_2 [Villaume08] was similar.

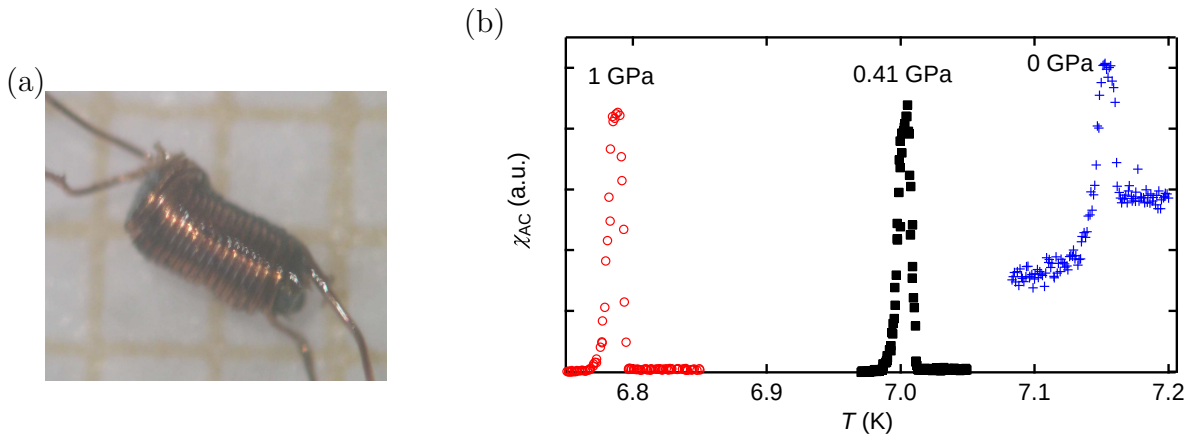

Figure 2.13: (a) Home made lead manometer for AC susceptibility measurement. (b) Signal of the superconducting transition of lead at different pressure measured by AC susceptibility in a Physical Properties Measurement System (PPMS). To avoid the effect of a small remanent field, a small error in the calibration of the thermometer, or a shift due to the definition of T_{sc}, the pressure is determined by comparing with the value at ambient pressure and using the pressure variation given in [Bireckoven88]. No significant broadening of the transition is observed, indicating that the pressure gradient is smaller than 0.04 GPa.

limit of the material[6]. But when the deformation is too large, the pressure tightness is not preserved. Indeed, the more the applied force, the more the cell body is expanded, so that the sealing between the piston and the body is difficult.

The use of hybrid body with NiCrAl alloy allows one to reach around 3 GPa at low temperature.

2.3.2 Diamond Anvil Cell

To reach higher pressure, it is necessary to use anvil cells. Indeed, in this type of cell, the more the force is applied, the more the pressure tightness is efficient : the gasket is squeezed more and more by the anvil.

The first anvil cell was made by Bridgman who was awarded the Nobel Prize in 1946. Bridgman cells can reach pressures as high as 30 GPa with anvils made from sinterer diamond (the sintering makes the anvil magnetic), or 10 GPa with a tungsten carbide WC anvil non magnetic. In this type of cell, pressure gradients are due to the pressure transmitting medium which is solid : most of the time steatite.

This cell has been improved to the diamond anvil cell. Monocrystaline diamond is the hardest known material : it allows one to reach very high pressures, above 300 GPa. Diamond anvils are transparent, so that optical measurements are possible. In particular, the determination of pressure by ruby fluorescence is a precise technique and is possible at any temperature [McCumber63, Barnett73, Piermarini75]. The metallic gasket allows the use of liquid as pressure transmitting medium. In particular, liquid helium is known to be the most hydrostatic liquid. Liquid argon is also very good (see also [Tateiwa09]). However, the size of the pressure chamber is limited by the size of the diamond, i.e. by the price. In practice, all the measurements are realized on a sample with $100 - 300$ μm length and a few 10 μm width.

Since the gasket is metallic, the wires have to be electrically isolated from the gasket. The gasket preparation is a critical stage of the experimental set up and has been improved for years in the laboratory (see in particular [Thomasson97, Thomasson98]). The metallic gasket is initially a sheet of stainless steel of 500 μm. It is squeezed in the anvil so that the width is reduced to 120 μm (typically applying 8000 N). In the center of the diamond print, a hole of diameter 500 μm is produced with a chamfer on both sides of the gasket. The insulation is realized by depositing an epoxy resin on the gasket. It is saturated with alumina powder (1 μm) in order to reinforce the hardness. This preparation is polymerized at 70 $^\circ$C for 8 minutes. Then, the hole is re-made. The typical width of the insulation film at this stage is 100 μm. If it is less, the wires might be grounded to the metallic gasket. If the width is too large, it might become too much deformed and fill the inside of the pressure chamber. It is possible to reduce the width of the film with a drill. The polymerization is then completed for 1 hour at 70 $^\circ$C with a small pressure (typically 2000 N) exerted by the diamond anvils (grease on the diamond prevent the film from gluing). Then the hole and chamfers are re-made. The typical width of the insulation film at the end is $50 - 60$ μm.

The pressure setup is fragile because of the weakness of the electrical contacts on the sample, the wires and their way through the gasket. Breaking of the wires or short circuits can occur at several stages :

- the loading

[6]In fact, it is possible to reach around 1.5 times the elastic limit of the material.

- when the pressure is changed
- the successive heating-cooling processes

In this work, a diamond anvil cell has been set up successfully for resistivity measurements (see fig. 2.14). The results are presented in section 4.1.6. The ruby fluorescence has been used to determine the pressure (see fig. 2.15). Argon was used as a pressure transmitting medium. An attempt to set up another cell for AC susceptibility measurement has been done (see fig. 2.16), but the wires were grounded after the pressure loading.

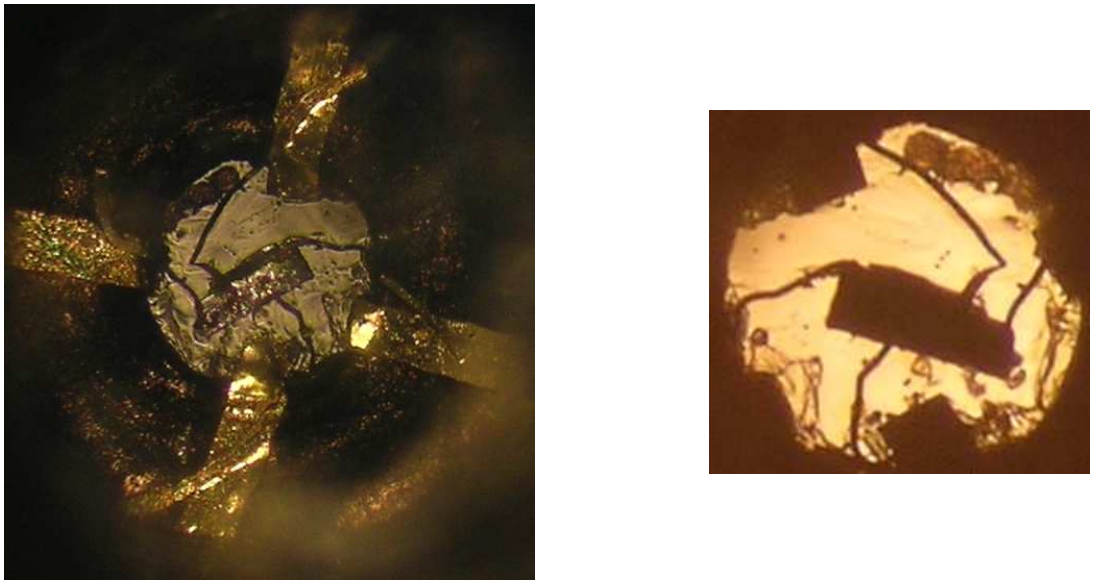

Figure 2.14: Inside view of the diamond anvil cell for resistivity measurement on UGe_2. The gold wires (diameter 10 μm) are spot welded on the sample on one side, and squeezed on flattened gold wire (initial diameter 25 μm) going through the gasket.

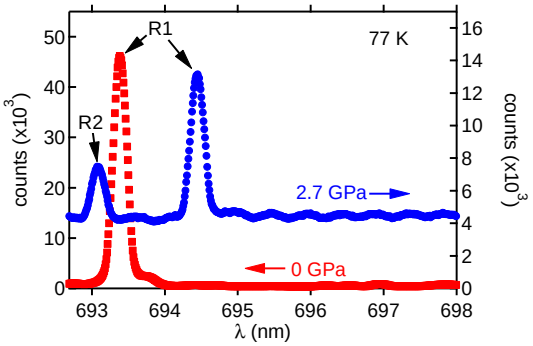

Figure 2.15: Ruby spectra at 77 K at ambient pressure and at 2.7 GPa in a diamond anvil cell for resistivity measurements on UGe_2. The background in the spectra under pressure is unexpectedly high, but the determination of the pressure is possible.

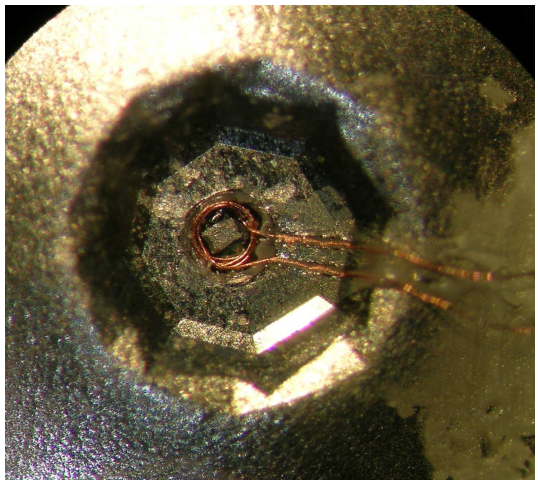

Figure 2.16: Inside view of the diamond anvil cell for AC susceptibility measurement on UGe_2. In addition to the ruby, a small piece of tin (Sn) has been used to determine the pressure. The home-made pick-up coil consists of 10 loops of copper wire whose diameter is 14 μm. The excitation coil (not visible here) is outside the pressure chamber.

2.4 AC Calorimetry under Pressure

Under pressure, the sample is thermally coupled to the pressure medium so that adiabatic and relaxation techniques are not possible. However, these techniques can be used to measure the specific heat of the system (pressure cell + sample). The subtraction of the specific heat of the (pressure cell alone) allows one to obtain the specific heat of the sample. This has been done to determine the specific heat of UGe_2 in the pressure induced superconducting state by Tateiwa *et al.* [Tateiwa01b, Tateiwa02, Tateiwa04] on single crystals and by Vollmer *et al.* on polycrystals [Vollmer02]. Their results are presented in section 3.11.1. Despite the rather small specific heat jump at the transition, and the discrepancy of the p-T phase diagram with resistivity experiments, no other specific heat measurements have been reported, as a consequence of the experimental difficulty.

The AC calorimetry method is adapted to small samples and pressure conditions. This technique will be presented in a first section. Then, a first comparison with the measurements will done and the validity of the results will be discussed.

2.4.1 Principle

This technique consists of transmitting AC power (P_0 with a frequency ω) to the sample so that the temperature of the sample T_{AC} oscillates at the same frequency. By definition, the specific heat is the amount of energy necessary to increase the temperature by 1 degree for an isolated sample :

$$C_p = \frac{\delta Q}{dT}$$

where a heat quantity δQ induces an increase of the temperature of the sample dT. In the case of AC calorimetry, if the sample is big or has a large heat capacity, the temperature variation T_{AC} is small. Conversely, if the sample is small or has a small heat capacity, T_{AC} will be larger. In a first approximation, one can consider that $T_{AC} \propto \frac{1}{C}$. However, this is not always correct depending on the frequency ω of the excitation.

A model has been developed in ref. [Sullivan68]. Neglecting all the time constants between the sample, the heater and the thermometer, the model can be simplified so that :

$$T_{AC} \approx \frac{P_0}{\omega C} \frac{1}{\sqrt{1 + \left(\frac{\kappa_B}{\omega C}\right)^2}} = \frac{P_0}{\sqrt{\kappa_B^2 + (\omega C)^2}} \tag{2.1}$$

where κ_B is the thermal conductivity to the bath (see fig. 2.17). To select a correct frequency for the measurement, it is convenient to consider the quantity $\log(\omega T_{AC})$. Several regions are presented.

- At low frequency, $\omega << \frac{\kappa_B}{C}$, it becomes $T_{AC} \approx \frac{P_0}{\kappa_B}$.
  This is region 1 of fig. 2.18 where $\log(\omega T_{AC}) \approx$ const + $\log(\omega)$.

- At higher frequency, $\omega >> \frac{\kappa_B}{C}$, it becomes $T_{AC} \approx \frac{P_0}{\omega C}$.
  This is region 2 of fig. 2.18 where $\log(\omega T_{AC}) \approx \log(\frac{P_0}{C})$. The measurements have to be performed in that region when it exists.

At much higher frequency, the sample has no time to reach a thermal equilibrium. The model has to consider the characteristic time of internal diffusion in the sample τ_{int} and the thermal conductivity of the sample κ_s [Sullivan68] :

$$T_{AC} \approx \frac{P_0}{\omega C} \frac{1}{\sqrt{1 + \left(\frac{\kappa_B}{\omega C}\right)^2 + (\omega\tau_{int})^2 + \frac{2\kappa_B}{3\kappa_s}}}$$

- At high frequency, $\omega >> \frac{1}{\tau_{int}}$, it becomes $T_{AC} \approx \frac{P_0}{\omega C}\frac{1}{\omega\tau_{int}}$.
  This is region 3 of fig. 2.18 where $\log(\omega T_{AC}) \approx \text{const} - \log(\omega)$.

- Further increasing the frequency, T_{AC} will decrease and will reach a noise level which is frequency independent.
  This is the region 4 of fig. 2.18 where $\log(\omega T_{AC}) \approx \text{const} + \log(\omega)$. This regime is also observed if the signal is cut off by the transformer, filters, pre-amplifier....
  If the regions 2 and 3 are not observed experimentally, there is no way to separate region 1 from region 4.

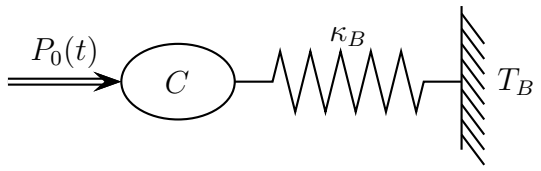

Figure 2.17: Simplified model for the AC calorimetry. The sample with a specific heat C is coupled to a thermal bath at the temperature T_B through a thermal leak of conductivity κ_B.

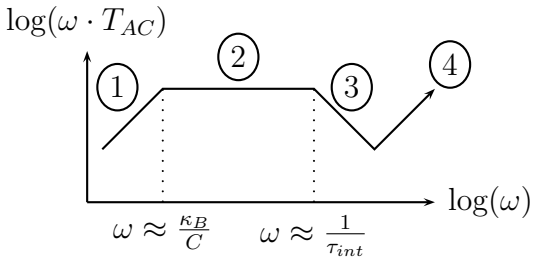

Figure 2.18: Frequency characterization of the signal in the case of a simple model of AC calorimetry. The different regions are discussed in the text.

2.4.2 Comparison with the Experiment

During this work, AC calorimetry measurements have been performed on UGe_2 under pressure in a piston cylinder cell. Four gold wires (I^-, V^-, V^+ and I^+) are spot welded on the sample for resistivity measurements.

In addition, an iron doped gold wire Au-Fe(0.07%) is spot welded on a gold wire (I^+) to constitue a thermocouple (see fig. 2.19). The thermocouple is used to follow the temperature variation of the sample T_{AC}. The sensitivity of the thermocouple has been calibrated by D. Jaccard (see fig. 2.20). The AC part of the thermocouple voltage is measured by a Lock-In amplifier after being amplified by a factor 100 with a low noise transformer and by a factor 100 by a pre-amplifier.

The field dependence of the thermocouple sensitivity is expected to be rather large. The thermopower of Au-Fe(0.07%) indeed changes with magnetic field [Chiang74], however no measurements have been done below 4 K. Recently, the thermocouple Chromel-AuFe(0.07%) has been measured under magnetic field. A variation as high as 30% at 1.6 K and 3 T is reported [Stockert11]. However, it might also arise from the Chromel. Moreover, in our measurement the contribution of the 99.99% Au wire is neglected, even though it contain Fe (less than 20 ppm).

However, it has to be noted that this technique has been successfully used to study $CeRhIn_5$ under pressure at field up to 7.5 T [Knebel06](see fig. 2.21). No significant

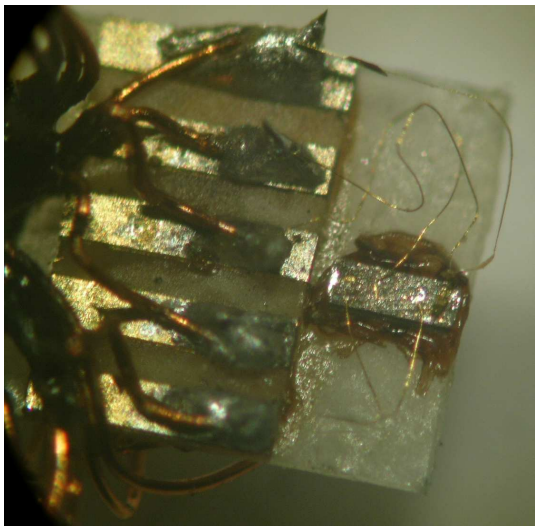

Figure 2.19: Experimental setup of the resistivity and AC calorimetry measurement under pressure on UGe_2.

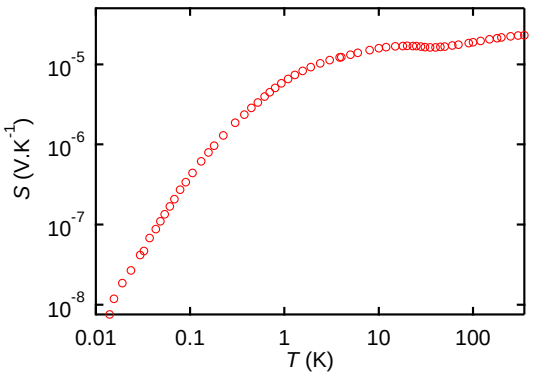

Figure 2.20: Sensitivity of Au/Au-Fe(0.07%) measured by D. Jaccard.

change of the slope has been observed below the transition temperature, so that it can be concluded that the field dependence of the thermocouple does not modify significantly the physical result obtained in this measurement. Our set up is similar to the one used successfully to detect the superconducting transition by AC calorimetry and resistivity in $CeIrSi_3$ (see fig. 2.22).

In the set up presented in fig. 2.19, an electrical current through two contacts constitute a heater. It is assumed that the resistivity of the sample and the wires is negligible compared to the contacts resistance estimated around 10 mΩ by a direct measurement. Since an excitation at a frequency ω will induce a joule effect at a frequency 2ω, the response has to be measured at the second harmonic (2ω).

The frequency dependence of the measured signal is presented in fig. 2.23. The observed behavior is roughly the same as the schematic prediction of fig. 2.18. However, the region of interest (region 2) with a plateau is not observed. This is certainly due to the cut off arising from the internal diffusion. Therefore, the measurements above 2 K have been performed at a low frequency (4.3 Hz). Even if it is not possible to consider $T_{AC} \propto \frac{1}{C}$, the observed anomaly at the Curie temperature in UGe_2 can be attributed to the change of specific heat at the transition (see fig. 2.24).

At low temperature, the frequency characterization shows a plateau as expected from the simple model (see fig. 2.25). It means that equation 2.1 should be valid. The anomaly at the superconducting transition can be observed at different frequencies of the excitation (see fig. 2.26). Using equation 2.1, measurements at several ω allows one to extract the temperature dependence of C/T. The different values of ω have to been chosen in the range where the simple model seems to be valid, and not too close, so that the specific heat part is not canceled. For the measurements presented in chapter 5, the chosen frequencies are 37 and 87 Hz. It is possible to have an idea of the validity of this procedure by measuring at another frequency : the results should not depend on the choice of ω. Experimentally, this is not the case as visible on fig. 2.27. However, this is usual in measurements with the AC calorimetry technique. Moreover, the shape in arbitrary units remains unchanged.

Another difficulty with the measurement under pressure is that the environment of

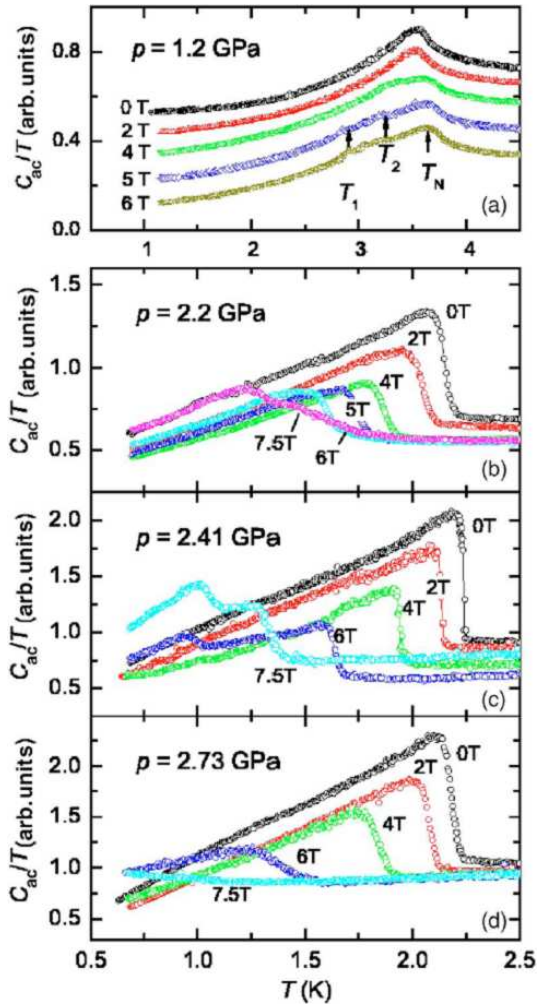

Figure 2.21: C_{AC}/T versus the temperature of $CeRhIn_5$ at different pressures for various magnetic fields $H//ab$. Data in (a) are shifted for clarity [Knebel06].

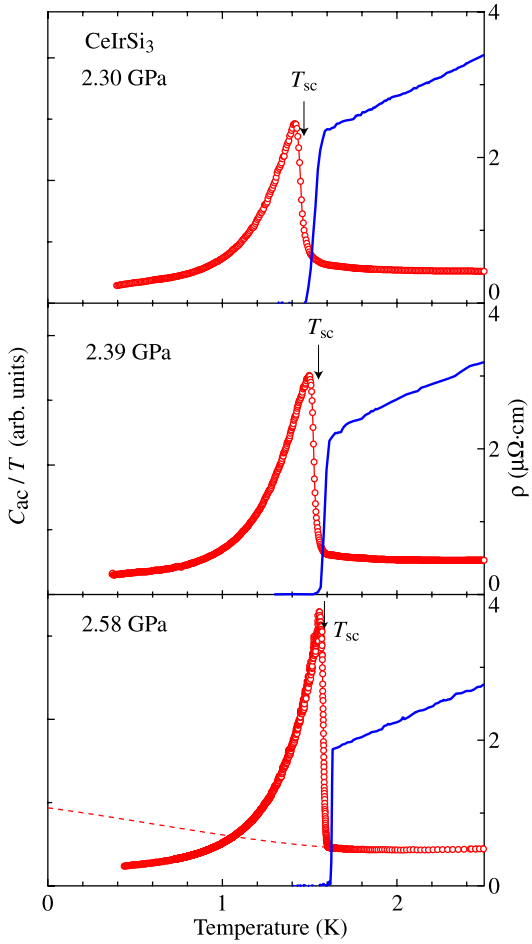

Figure 2.22: Temperature dependence of the AC heat capacity C_{ac} (circles, left side) and electrical resistivity ρ (lines, right side) at 2.30, 2.39, and 2.58 GPa in $CeIrSi_3$. The dotted line indicates the entropy balance below T_{sc} at 2.58 GPa [Tateiwa07].

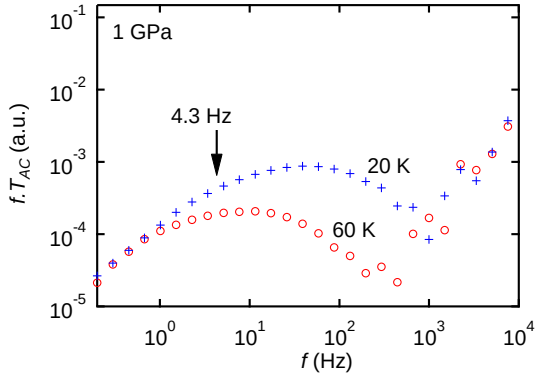

Figure 2.23: Frequency caracterisation of the AC calorimetry experiment at 1 GPa at different temperature.

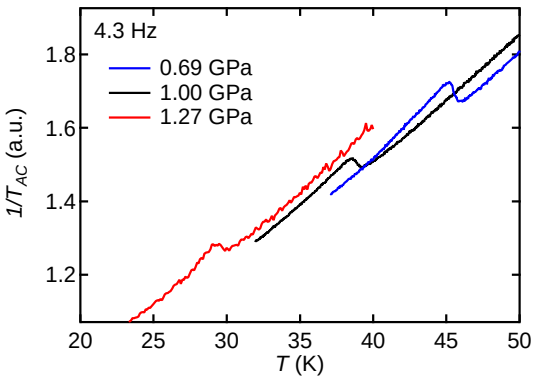

Figure 2.24: Temperature dependence of $1/T_{AC}$ measured at 4.3 Hz at different pressures for UGe_2. The anomaly at the Curie temperature is detected as a jump.

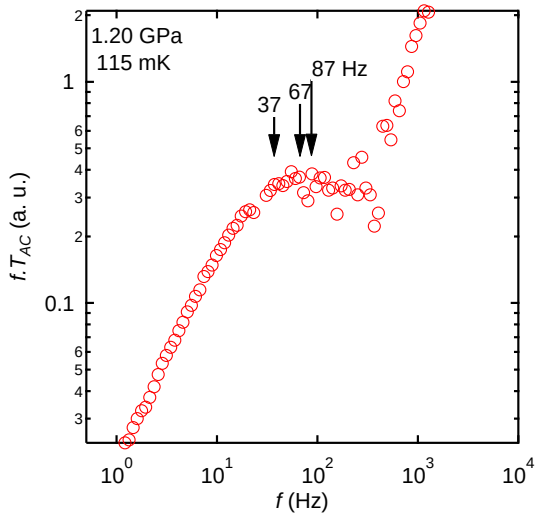

Figure 2.25: Frequency characterization of the AC calorimetry experiment at 1.20 GPa at 115 mK.

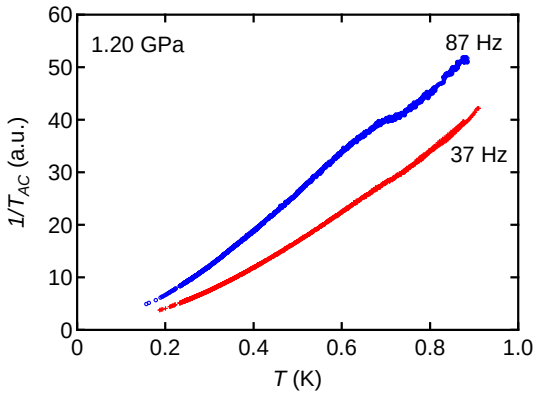

Figure 2.26: Temperature dependence of $1/T_{AC}$ measured at different frequency of the excitation at 1.20 GPa for UGe_2. The anomaly at the superconducting transition can be observed around 0.7 K.

the sample contributes to the measured specific heat. This effect is considered to be more important at low frequency. However, the increase of the frequency gives rise to the problem of internal thermalisation in the sample. By subtracting the signal at two different frequencies, it can be assumed that the effect of the environment is canceled in the first approximation.

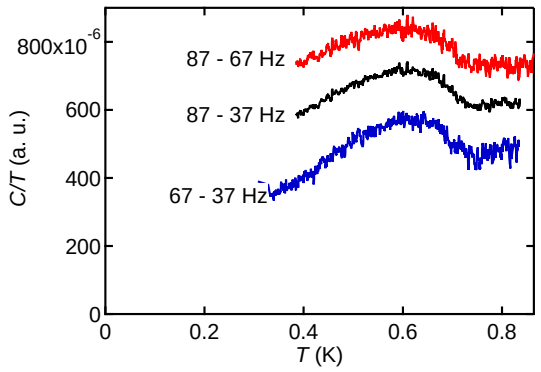

Figure 2.27: Temperature dependence of C/T determined using equation 2.1 and measurements at several ω.

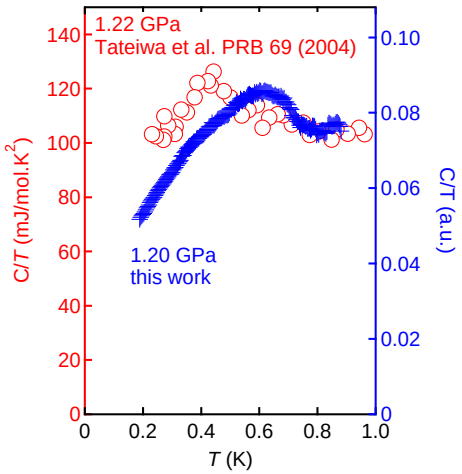

Figure 2.28: Comparison of the temperature dependence of C/T measured at 1.22 GPa by Tateiwa *et al.*[Tateiwa04] and at 1.20 GPa in this work.

Such a temperature dependence at a superconducting transition could appear to be disappointing when compared to other superconducting transitions measured under pressure with the same technique [Tateiwa07] (see fig. 2.22 page 35). However, it has to be remembered that this work constitutes the first report of the superconducting transition in UGe_2 by AC calorimetry. Moreover, it has to be compared to the only previous report of specific heat on single crystal of UGe_2 performed by Tateiwa *et al.* by the adiabatic technique. The biggest anomaly is reported in ref. [Tateiwa04] and is similar to our result (see fig. 2.28). This indicates that our signal is very close to the specific heat.

2.5 Thermal Expansion under Pressure via Strain - Gauges

The principle of thermal expansion measurements via strain gauges is relatively simple. It consists of measuring the electrical resistivity of a wire glued on the sample. When the sample expands, the wire's length increases as well and it becomes thinner. Since the diameter is reduced (the cross-section S decreases), the electrical current flow is more difficult, i.e. the resistance R of the wire increases.

$$R = \rho \frac{L}{S}$$

The measurement is improved with increasing the wire's length L. In practice, the wire is folded over in a coil shape as can be seen on fig. 2.29 which shows a commercial strain gauge glued on a sample of $CeRhIn_5$.

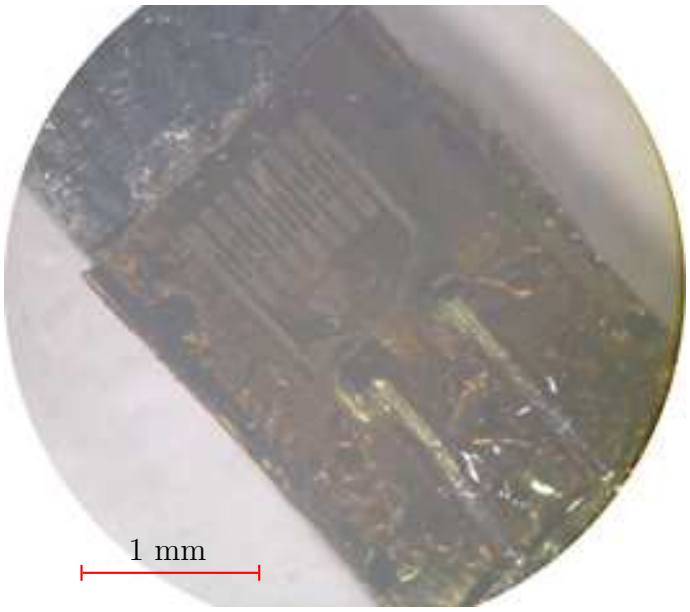

Figure 2.29: Commercial strain gauge glued on a sample of $CeRhIn_5$.

This measurement technique is not possible at the present time in a diamond anvil cell, since the size of the sample is too small (less than 600 μm). Such a small strain gauge does not exist yet.

If the principle is simple, the practice is more complicated. The strain gauge has to be perfectly glued on the sample with a very small amount of glue, so that the expansion to be measured is not absorbed. The glue Kyowa PC-6 is adapted to strain gauges. Since that glue does not seem to work on $CeRhIn_5$ (the strain gauge does not follow the thermal expansion of the sample), I tested other types of glue, but no other glue available in the laboratory could resist down to 2 K (the strain gauges pop off at low temperature). Up to now, no results of thermal expansion under pressure of $CeRhIn_5$ have been reported.

The second difficulty is to measure the change in the strain gauge resistance. The usual method is to use a Wheatstone bridge. I used resistances whose changes with the fluctuations of the ambient temperature are small (less than 10 ppm/ $^\circ$ C). The signal was amplified by a factor 100 with a low noise transformer (Signal Recovery Model 1900) and measured with a lock-in. The excitation was 80 mV rms at 17 Hz.

The second resistance of the Wheatstone bridge is a strain gauge glued on a reference material. For measurements on $CeRhIn_5$ and URu_2Si_2 [Villaume08], silicon has been used. For the one on UGe_2, it was tungsten carbide. These materials have small thermal expansion coefficients (less than 10^{-7} K^{-1} below 40 K). In order to compare measurements at different pressures, the strain gauge on the reference material must be inside the pressure cell. Indeed, the pressure changes the sensitivity of the strain gauge but this effect is canceled between the two strain gauges. However, for the second measurements on URu_2Si_2, the samples were so big that the reference strain gauge was outside the pressure cell. This was sufficient since the point was only to detect the phase transitions from the paramagnetic to the hidden order state (HO) and then from HO to the antiferromagnetic state.

The precision on the relative expansion $\frac{\Delta L}{L}$ is about 10^{-7}. This can be compared with X-rays (10^{-5}). It is also possible to use a capacitive cell with a very high precision (10^{-10}). This technique can also be used under magnetic field, but not under hydrostatic pressure.

2.6 Main Results Obtained with the New Crystals

In this section, the new results which have been obtained with the new crystals grown in the tetra-arc furnace are briefly presented. More information about the results can be found in the references.

2.6.1 URu_2Si_2

The p-T phase diagram of URu_2Si_2 is presented in fig. 2.30. At ambient pressure, a transition occurs at $T_0 = 17.5$ K [Palstra85] to a state which has not yet been identified ; this phase is called the hidden order phase (HO). Under pressure, the hidden order state is changed into an antiferromagnetic phase above p_x. In the measurements just above p_x, two successive transitions are observed : the first one at T_0 from the paramagnetic state (PM) to HO and the second at T_x from HO to AF. Thus these measurements allow a comparison of the three states at the same pressure. However, p_x depends on sample quality [Motoyama03] and degree of hydrostaticity [Amitsuka08, Butch10]. Therefore, it is necessary to perform measurements on URu_2Si_2 to know if the three states exist at constant pressure. Compared to resistivity and AC calorimetry measurements which shows only fainted anomalies at T_x, the thermal expansion shows a clear change at both T_0 and T_x (see fig. 2.31).

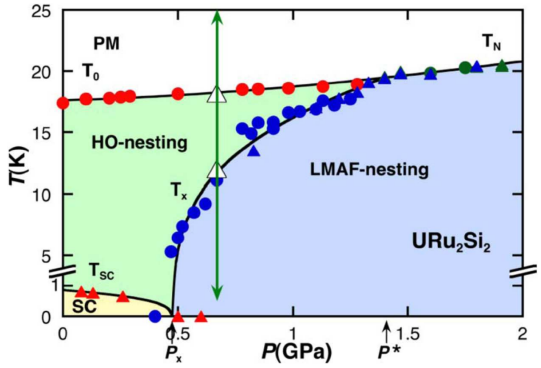

Figure 2.30: T-P phase diagram of URu_2Si_2 from resistivity (circles) and AC calorimetry (triangles) measurements [Hassinger08] with the low-pressure hidden order phase (HO) and the high-pressure antiferromagnetic phase (AF). Bulk superconductivity state is suppressed at P_x when antiferromagnetism appears. The open triangles correspond to the determination of T_0 and T_x at $P = 0.67$ GPa from thermal expansion [Villaume08].

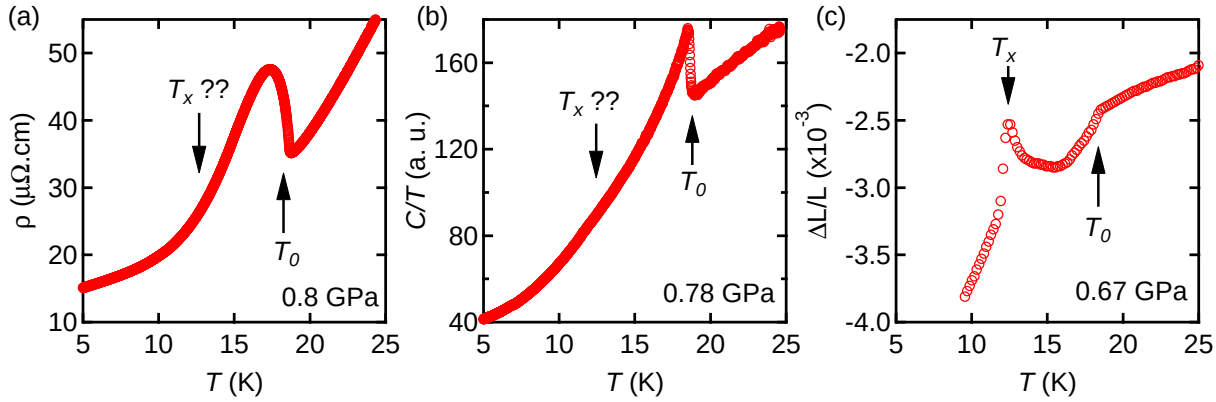

Figure 2.31: Comparison of the resistivity, AC calorimetry and thermal expansion measurements to detect the T_x anomaly at the transition from the hidden order state to the antiferromagnetic state in URu_2Si_2. The anomaly is clearly seen in the thermal expansion measurements. The thermal expansion data have been measured in ILL by Alain Villaume teaching me the technique [Villaume08]. Resistivity and AC calorimetry data have been measured by Elena Hassinger.

Performing inelastic neutron scattering at a pressure where the three states (PM-HO-AF) exist, a signature of the HO has been found : a low energy excitation at the wave vector $Q_0 = (1, 0, 0)$ [Villaume08].

The initial target was to obtain big single crystals for inelastic neutron scattering under pressure. The experiment required growth of the crystals along the c-axis using an oriented seed (see fig. 2.32). Considering the cost of neutron beam time in ILL (Laue Langevin Institute) and the difficulty of pressure experiments, two pressure cells have been set up in parallel by Dr. Dai Aoki and myself (see fig. 2.33).

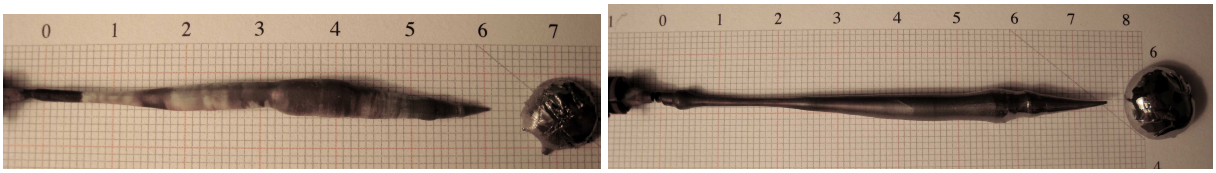

Figure 2.32: As grown ingots of URu_2Si_2 #G1 (left) and #G2 (right) in a tetra arc furnace using seeds oriented along the c-axis.

The experiment confirms that above p_x, i.e. in the AF state, the HO state is induced by a magnetic field applied along the c-axis. This is supported microscopically by neutron scattering and macroscopically by thermal expansion measurements [Aoki09a]. It is important to know the phase diagram of URu_2Si_2 under magnetic field (see fig. 2.34) because the Fermi surface studies with dHvA or SdH experiments are performed under magnetic field and that the knowledge of the ground state is necessary.

The big samples have been used for several neutron experiments. A precise study of the excitation at $Q_0 = (1, 0, 0)$ has been done [Bourdarot10b]. To investigate the link between the hidden order and the superconductivity, the excitation has been studied above and below T_{sc}. A weak but clear positive energy shift of ~ 40 μeV has been detected in the superconducting phase (at $T \approx 400$ mK) for the resonance at $Q_0 = (1, 0, 0)$. This result indicates that the wave-vector Q_0 is connected with the order parameters of the hidden order and of superconductivity [Bourdarot10a]. Before that experiment, I checked the superconducting transition by AC susceptibility (see fig. 2.36). A copper wire has been

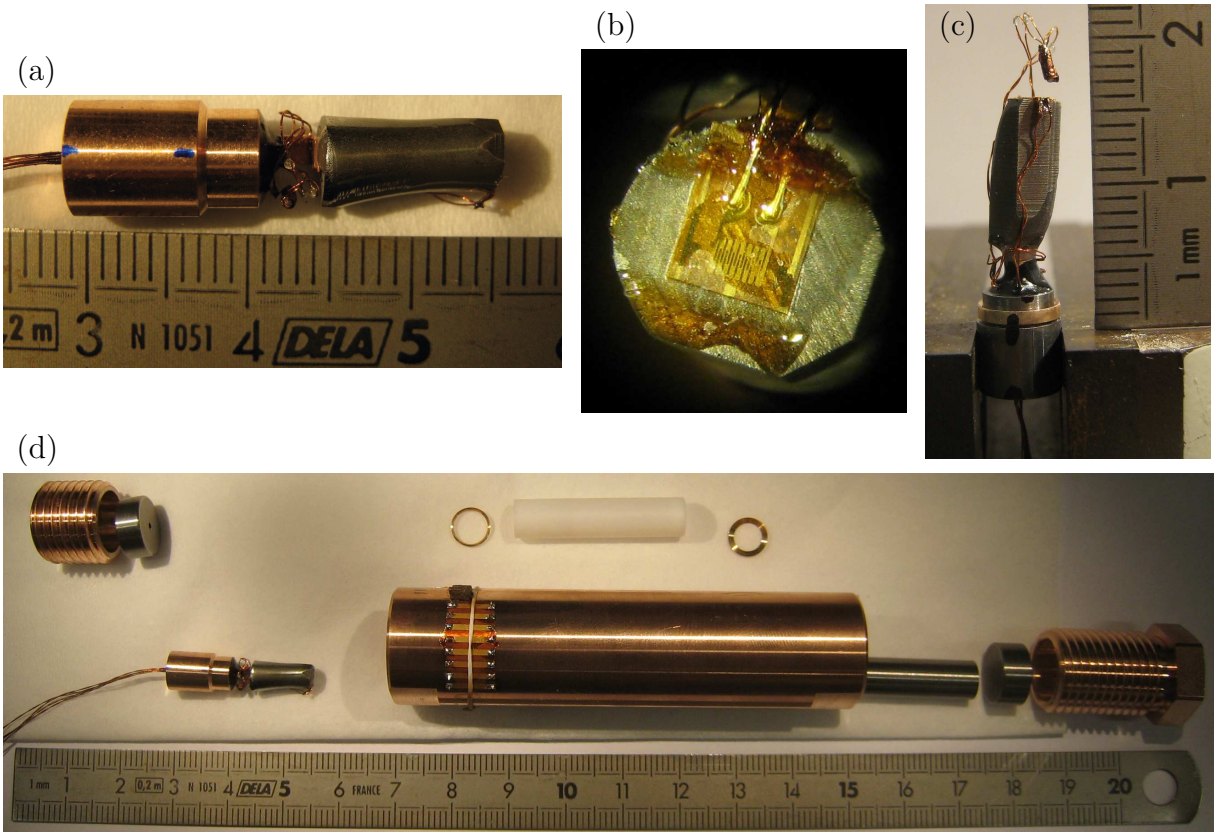

Figure 2.33: Experimental set up of two obturators (a) and (c) for two similar pressure cells (d). The big samples are single crystals of URu_2Si_2. A strain gauge is glued on top of each sample for thermal expansion measurement (b). A home-made Pb-manometer is used to determine the pressure.

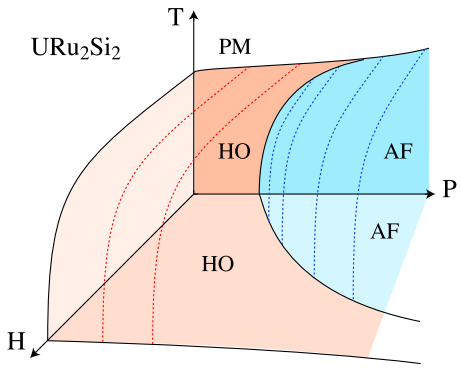

Figure 2.34: Schematic temperature - pressure - magnetic field phase diagram of URu_2Si_2 [Aoki10].

glued directly all around the big sample to create a pick up coil. An excitation coil has been specially designed and made with a winding machine. It is large enough to contain a big sample with a pick up coil, but small enough to fit in the He^3 PPMS refrigerator (see fig. 2.35). Since the current in the excitation coil is limited by the PPMS, an external lock-in has been used. The signal was amplified by a factor 100 with a low noise amplifier.

Figure 2.35: Excitation coil for AC susceptibility measurements in a He^3 PPMS refrigerator.

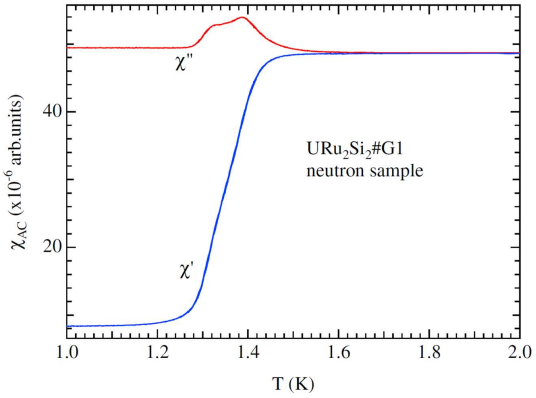

Figure 2.36: Temperature dependence of the AC susceptibility of a URu_2Si_2 sample used for neutron scattering experiment. This measurement has been published in [Bourdarot10a].

Small parts of the single crystal ingot were of very high quality. It has been possible to detect SdH oscillations [Aoki10] and to reinvestigate the Fermi surface properties. Elena Hassinger detected a new heavy branch η ($\sim 20m_0$) and it is shown that the previously detected heavy β branch splits into two branches when rotating the field from the c to the a axis. Under pressure for $H||c$ the Fermi surface shows only minor changes between the HO state and the AF state. These are strong indications that both phases have the same unit cell doubling and the same ordering vector [Hassinger10].

I have also grown (see fig. 2.37) and prepared a crystal for uniaxial pressure and inelastic neutron scattering (see fig. 2.9 page 27). The results of this experiments are being analyzed by Frédéric Bourdarot at the moment.

Figure 2.37: As grown ingots of URu_2Si_2 #G4 in a tetra arc furnace using a seed oriented along the a-axis. The c plateau can clearly be observed.

The temperature T_0 where the hidden order appears can be tuned from 17.5 to 0 K by applying a magnetic field of $H_m \approx 35$ T along the c axis. Various phases are observed in the proximity of this quantum critical point (QCP) [Sugiyama90, Sugiyama99, Harrison03, Kim03, Kim04]. As can be seen on fig. 2.30, T_0 increases with pressure, so that H_m is expected to increase as well. However, a negative pressure can be obtained with chemical substitution. If T_0 is reduced significantly, H_m will be reduced to below 15 T so that experimental study including neutron scattering experiments will be possible.

Thus, I have grown a single crystal of $URu_2(Si_{1-x}Ge_x)_2$ with $x \approx 9\%$ (the starting materials were in the stochiometry $URu_2Si_{1.82}Ge_{0.18}$, but the final stochiometry has not

yet been checked). During the pulling of the single crystal, the ingot accidentally droped down and melt again, but the arc discharges have been stopped almost instantaneously so that pieces of single crystals remain (see fig. 2.38). Dai Aoki has started to characterize the crystals in a PPMS (see figs. 2.39 and 2.40).

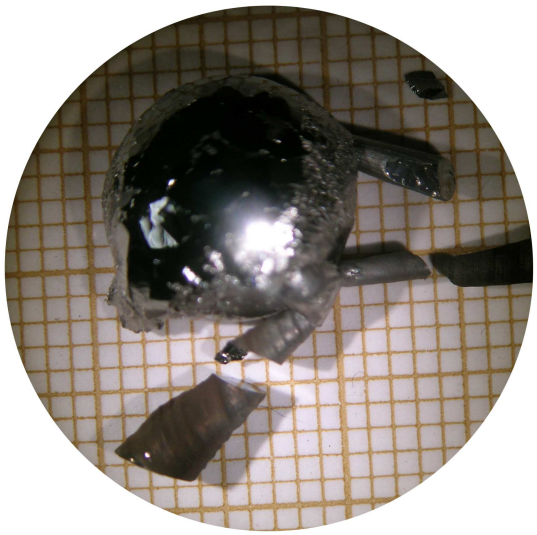

Figure 2.38: As grown $URu_2(Si_{1-x}Ge_x)_2$ with $x \approx 9\%$. During the pulling of the single crystal, the ingot accidentally droped down and melt again (spherical polycrystal in the picture), but the arc discharges have been stopped almost instantaneously so that pieces of single crystals remain.

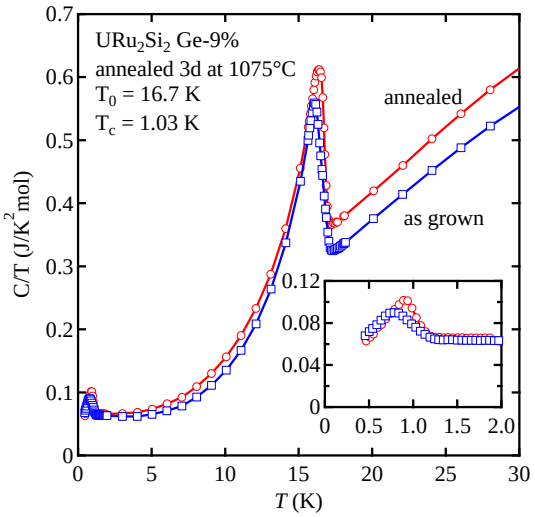

Figure 2.39: Temperature dependence of C/T of $URu_2(Si_{1-x}Ge_x)_2$ with $x \approx 9\%$.

Both resistivity and specific heat measurements show that the temperature T_0 of the transition to the hidden order state is reduced from 17.5 K in the pure system to 16.7 K in a 9% Ge doped sample. This confirm a previous report [Dhar92, Park94]. However, the specific heat jump at T_0 remain sharp compared to the measurement in ref. [Dhar92] (see fig. 2.41). Interestingly, the temperature T_{sc} of the superconducting transition is not suppressed and seems rather sharp even in the specific heat measurement.

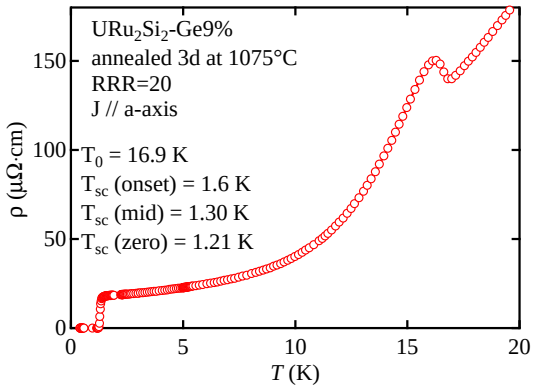

Figure 2.40: Temperature dependence of the resistivity of $URu_2(Si_{1-x}Ge_x)_2$ with $x \approx 9\%$.

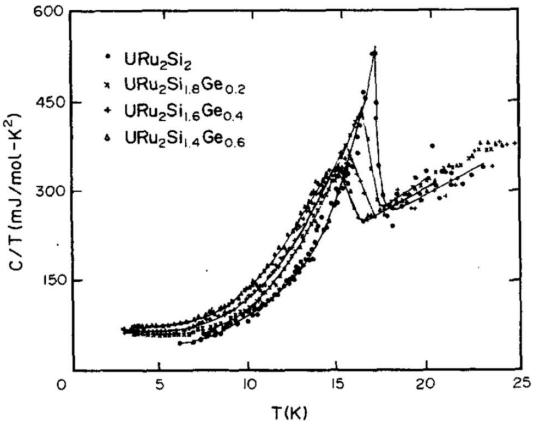

Figure 2.41: Temperature dependence of C/T of $URu_2(Si_{1-x}Ge_x)_2$. The lines are guides to the eye [Dhar92].

A higher percentage of Ge substitution has to be done to reduce T_0 even more significantly. Doing this, the evolution of the superconductivity has to be followed carefully.

It appears that the new crystals of URu_2Si_2 open many new experimental investigations. At the moment, the measurements performed on these crystals are not all finished. One can expect other interesting results from the thermo electric power measurement of Liam Malone, thermal expansion by Frédéric Hardy, neutron scattering by Frédéric Bourdarot and Eric Ressouche, Fermi surface study by Georg Knebel and Dai Aoki. . . .

2.6.2 UCoGe

High quality single crystals of UCoGe are more difficult to obtain. As explained in section 2.1.3, we have grown crystals of good quality so as to obtain new experimental results.

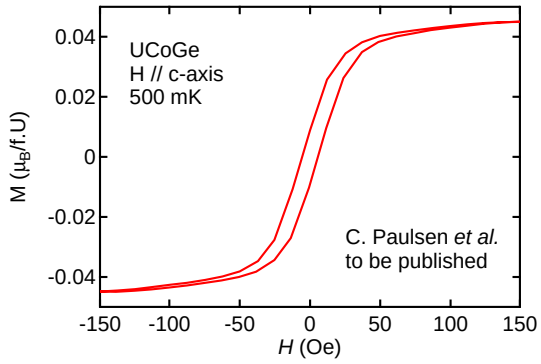

Figure 2.42: Magnetization curve of UCoGe for field along the c axis.

UCoGe is a ferromagnetic superconductor [Huy07]. It crystallizes in the orthorhombic TiNiSi-type structure (space group *Pnma*) [Canepa96] which is the same crystal structure as URhGe [Tran98] another ferromagnetic superconductor [Aoki01]. In UCoGe, a small ordered moment of $0.07\mu_B$ along the c-axis appears below the Curie temperature $T_C \approx 2.5$ K [Huy07, Huy08, Ohta10] (see figs. 2.42 2.43).

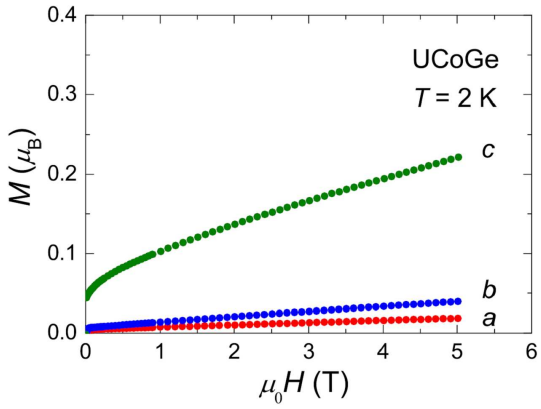

Figure 2.43: Magnetization of UCoGe for fields along the a, b, and c axis at $T = 2$ K. Ferromagnetic order is uniaxial with m_0 pointing along the c axis. In the limit, $T = 0$ K, $m_0 \approx 0.07\mu_B$ [Huy08].

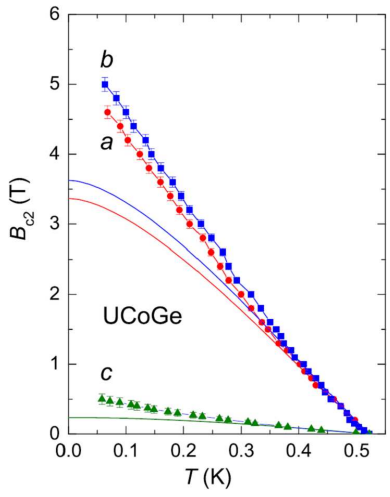

Figure 2.44: Temperature dependence of the upper critical field of UCoGe for B along the a, b, and c axis. The solid lines show the calculated dependence for a superconducting gap function with axial (along c) and polar symmetries (along a and b) (see [Huy08]).

Superconductivity is observed below $T_{sc} \approx 0.8$ K [Huy07]. A strong anisotropy of the upper critical field has been reported from resistivity measurements with current along

the a axis on a single crystal with RRR=30 (see fig. 2.44)[Huy08]. After obtaining a similar value for our single crystals, this experiment has been repeated. With a precise tuning of the magnetic field alignment, a much stronger anisotropy is observed (see fig. 2.45) [Aoki09b]. In addition to the fact that the measured critical field is higher than the previous report, a re-entrant behavior is observed for the field applied along the b-axis. As it will be presented in section 3.11.4, a similar behavior of the upper critical field has been observed in UGe_2 [Sheikin01, Huxley01] (see fig. 3.21 page 62) and in URhGe [Lévy05] (see fig. 5.18 page 102). This will be discussed in section 5.4 for the case of UGe_2. In UCoGe, the observed enhancement around 12 T seems to be linked to the tuning of the Curie temperature down to 0 K (see fig. 5.19 page 102)[Aoki09b]. However, it has to be confirmed by microscopic measurements.

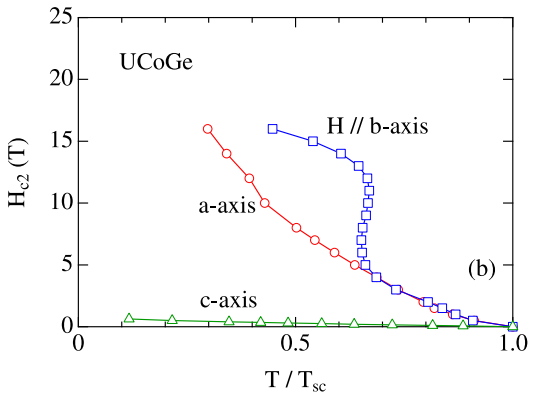

Figure 2.45: Temperature dependence of the upper critical fields for $H \parallel a$, b and c-axis. The temperature is normalized by the superconducting critical temperature T_{sc} at zero field [Aoki09b].

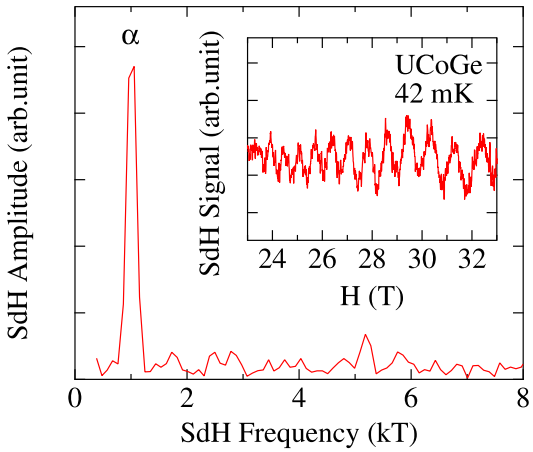

Figure 2.46: Typical FFT spectrum for the field tilted 10 ° from b to c-axis in UCoGe. The inset shows the corresponding SdH oscillation [Aoki11b].

Another result arises from the high quality of the crystals : the first observation of quantum oscillations in UCoGe (see fig. 2.46). The Shubnikov-de Haas signal is observed for the first time in a U-111 compound (UTGe, UTSi, T: transition metal). A small pocket Fermi surface ($F \approx 1$ kT) with large cyclotron effective mass $25m_0$ was detected at high fields above 22 T, implying that UCoGe is a low carrier system accompanied with heavy quasi-particles [Aoki11b].

One can expect other interesting results from the thermo electric power measurement of Liam Malone and Alexandre Pourret. Recently, bulk measurements of the thermal conductivity have been performed by Ludovic Howald. It confirms the unusual temperature dependence of the upper critical field. New measurements to higher field are scheduled by Mathieu Taupin. Dai Aoki continues to grow single crystals of UCoGe. Recently, he obtained samples with RRR=190, so that one may expect new results from these samples.

Chapter 3

Presentation of UGe_2

This chapter is a summary of the current status of research on UGe_2. New experiments are presented in chapters 4 and 5. For a rapid summary of the properties of UGe_2, see [Pfleiderer09].

3.1 The not so Simple Crystal Structure of UGe_2

The crystal structure of UGe_2 has been incorrectly identified for more than 46 years. In 1959, UGe_2 was reported to crystallize in a $ZrSi_2$ structure type (space group *Cmcm*) [Makarov59]. One year later, another crystallographic study led to the assignment of a distorted $ThSi_2$-type structure (space group *Amm2*) [Olsen60]. It is only in 1996 that the crystal structure of UGe_2 was reinvestigated and identified as a $ZrGa_2$-type structure (space group *Cmmm*) [Oikawa96]. This result was independently confirmed in 1997 [Boulet97] (and may actually be correct).

The crystal structure is shown in fig. 3.1 with the ferromagnetic moment (see section 3.2). The orthorhombic unit cell has dimensions $a = 4.0089$ Å, $b = 15.0889$ Å and $c = 4.0950$ Å [Oikawa96].

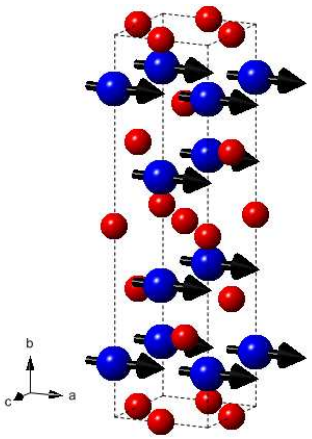

Figure 3.1: Unit cell of the crystal structure of UGe_2 with uranium atoms in blue and germanium in red. The arrows shows the magnetization orientation[Oikawa96].

The main consequence of the incorrect crystal structure assignment is that around 15 publications on magnetic and electrical properties of UGe_2 refer to the a axis instead of the c axis and vice versa. Band structure calculations were also performed with the wrong structure [Yamagami93].

3.2 Anisotropic Ferromagnet

Below $T_c = 52$ K, ferromagnetic ordering occurs. The saturated moment is given between $1.4 - 1.5\mu_B$/U along the a-axis (see [Olsen60][1] [Menovsky83][2] [Kernavanois01, Huxley01, Tateiwa01a] [Pfleiderer02, Sakon07]). The ferromagnetic structure has been confirmed by neutron scattering on powder samples[Boulet97]. A possible modulation of the magnetic structure has been explored by neutron scattering on a single crystal and they concluded that if an antiferromagnetic contribution occurs at a propagation vector situated along the a,b or c directions, it would be less than $0.06\mu_B$ [Kernavanois01]. Moreover, in synchrotron radiation x-ray diffraction experiments, charge density wave reflections have been investigated by means of the oscillation photographs covering the three-dimensional reciprocal spaces under several pressures up to 1.1 GPa. No superlattice Bragg peaks could be observed, resulting in an upper limit of intensity of $\sim 10^{-4}$ to the fundamental Bragg peak intensity [Aso06b].

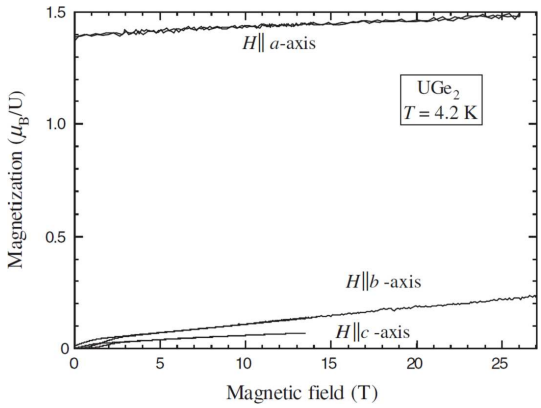

Figure 3.2: Magnetic field dependence of the magnetization. Measurements are carried out in a vibrating sample magnetometer (VSM) [Sakon07].

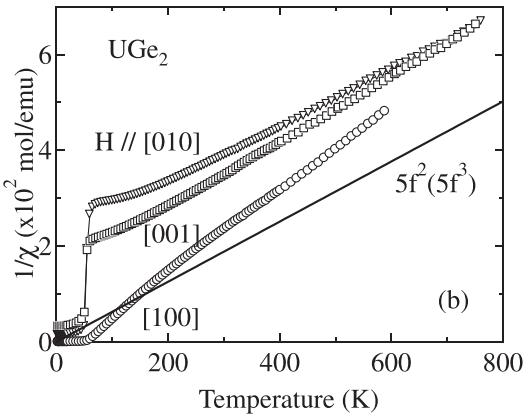

Figure 3.3: Temperature dependence of the inverse susceptibility. A solid line indicates the Curie law corresponding to a free ion ($5f^2$ or $5f^3$) [Galatanu05].

Susceptibility and magnetization measurements on single crystals revealed a strong anisotropy. The b and c axis are hard directions for the magnetization [Menovsky83, Sakon07][3]. This is illustrated in fig. 3.2 which shows the magnetization at 4.2 K under magnetic fields applied along the 3 crystallographic axis. For example the magnetization measured along the b-axis with a magnetic field up to 27 T remains less than 15% of the spontaneous magnetization along the a-axis. Only longitudinal fluctuations were observed from neutron scattering confirming the Ising nature of the system [Raymond04].

3.3 Itinerant Ferromagnet

To determine whether the f electrons are itinerant or localized is always difficult. UGe_2 is not an exception to this problem. Indeed, there are many conflicting experimental reports,

[1] In [Olsen60], a magnetic moment at saturation of $0.8\mu_B/U$ is reported from susceptibility measurements on a powder sample.

[2] I have no access to [Menovsky83], but according to [Onuki91] and later [Boulet97, Kernavanois01], the saturated moment is given as $1.43\mu_B/U$ along the a-axis.

[3] I have no access to [Menovsky83], but according to [Onuki91] and later [Boulet97, Kernavanois01], the magnetization along hard axis is less than 15% of the saturated moment at 21 T.

some of them arguing on the itinerant character and others on the localized one. In this section, the evidence for a degree of delocalization of the f electrons at low temperature is reviewed.

In standard heavy fermion behavior, the f electrons are localized at high temperature and below some characteristic temperature (sometimes called the *coherence temperature*) the f electrons behave no more independently which leads to strongly renormalized effective masses.

At high temperature, f electrons indeed appear localized :

- Above 450 K the reciprocal susceptibility shows the Curie-Weiss law for all the main crystallographic directions, with effective moments of 3.0, 3.6 and $3.4\mu_B$/U for [100], [010] and [001] directions, respectively[4] [Galatanu05][5] (see fig. 3.3). The effective magnetic moments are close to a free ion value[6] of $3.6\mu_B$.

- Above 160 K, the anomalous Hall coefficient R_s is 3 orders of magnitude larger than the ordinary Hall coefficient R_0 from which it is assumed that the scattering centers of the conduction electrons are the localized 5f electrons [Tran04].

- The results of measurements of positron annihilation radiation in the paramagnetic phase (around 60 K, i.e. above $T_C = 53$ K) are better explained by numerical calculation considering *5f* electrons as fully localized [Biasini03].

At low temperature, however, there is evidence for a degree of delocalization of the f electrons :

- Firstly, the value of the ordered moment of $1.4\mu_B$/U is smaller than the Curie-Weiss moment above the Curie temperature.

- The delocalization of the *5f* electron is also shown by the observation of carriers with high cyclotron masses of $(15-25)m_0$ by dHvA experiments [Onuki91, Satoh92, Terashima01, Settai02, Haga02]. These heavy masses suggest itinerant but strongly correlated *5f* electron states.

- Measurements of the optical conductivity also show that the effective mass starts to increase below T_C, suggesting an intrinsic coherence temperature $T^* < T_C$ [Guritanu08].

- In addition, the magnetization does not reach saturation at least up to 27 T applied along the easy magnetization a-axis (see fig. 3.2) [Sakon07][7].

[4]The corresponding paramagnetic Curie temperatures are 39, −310 and −210 K for [100], [010] and [001] directions, respectively [Galatanu05].

[5]See also [Onuki92, Saxena00, Huxley01] for values around 200 K.

[6]We can calculate the magnetic moment of an isolated free uranium ion for U^{3+} in the configuration $5f^3$: we have $S = \frac{3}{2}$, $L = 6$ and $J = |L - S| = \frac{9}{2}$. The Lande factor is $g_J = 1 + \frac{J(J+1)+S(S+1)-L(L+1)}{2J(J+1)} = \frac{8}{11}$. Thus, the magnetic moment for degenerate *5f* shell is $g_J\sqrt{J(J+1)}\mu_B = 3.62\mu_B$.

For U^{4+} in the configuration $5f^2$: we have $S = 1$, $L = 5$ and $J = |L - S| = 4$. The Lande factor is $g_J = \frac{4}{5}$. Thus, the magnetic moment for degenerate *5f* shell is $3.58\mu_B$.

Crystal electric field effect will split the *5f* level and can reduce the magnetic moment. However, no distinct evidence for crystal electric fields are reported, as common for uranium-based compounds. This is certainly because f-electrons of uranium are sufficiently itinerant to reduce the crystal field effect which occurs from localized charges. See also the Rhodes-Wohlfarth plot.

[7]A small field dependent ordered moment can also arise in the case of localized moments with a mixing of different crystal field levels (see [Huxley03b] and [Wang69]).

- The ordinary Hall coefficient changes its sign from negative to positive below ≈ 20 K and the carrier concentration starts to increase upon cooling. These results can be explained by a delocalization of some part of the 5f electrons [Tran04].

- Another argument is given in ref. [Huxley01] : "at ambient pressure, a degree of delocalization of the f electrons is suggested [Mohn89] by the moderate value of the low-temperature specific heat, $C/T = 32$ mJ.mol^{-1}K^{-2}, and the ratio of this to the step in C/T (200 mJ.mol^{-1}K^{-2}) at T_C." The same argument is reproduced in ref. [Pfleiderer09]. The given ref. [Mohn89] indeed compare the results of the Stoner model, which is the pure itinerant case, with a spin fluctuation model introduced by Murata and Doniach [Murata72] which assume fluctuation of a localized magnetization. It is shown in ref. [Mohn89] that the large specific heat jump at T_C in the Stoner model is reduced by the introduction of spin fluctuation. In the Stoner model, the excitations are single particles excitations, and $\Delta C_m = \frac{M_0^2}{\chi_0 T_C}$ where M_0 is the spontaneous magnetization and χ_0 the initial ferromagnetic susceptibility. It is reduced to $\Delta C_m = \frac{M_0^2}{4\chi_0 T_C}$ in the spin fluctuation model[8]. The T-linear magnetic contribution to the specific heat is $\gamma_m = -\frac{M_0^2}{2\chi_0 T_C^2}$ in the Stoner model which is increased to $\gamma_m = \frac{1}{5}\frac{M_0^2}{2\chi_0 T_C^2}$ in the spin fluctuation model[8]. Thus, it is qualitatively true that a degree of delocalization is suggested. However, none of these models can reproduce the experimental values[9].

- Finally, during the time of this study, simultaneous analysis of magnetization and heat capacity measurements in the framework of molecular-field theory allowed a derivation of the magnetic heat capacity [Hardy09] (see also section 4.2.3 page 86). The magnetic entropy at the Curie temperature is $S_{\text{magn}} = 0.8R\ln 2$, which is smaller than $R\ln 2$, but only by 20%.

The low temperature dependence of the magnetization has an intermediate behavior between itinerant and localized moments [Huxley03b], although the itinerant behavior can be observed if one restricts to the lowest temperatures [Hardy09].

High resolution photoemission spectroscopy PES indicates the presence of a sharp peak in the spectrum just below the Fermi level E_F. It is interpreted as the "coherent U 5f" peak originating from the itinerant 5f electrons. A broad shoulder is also attributed to the "incoherent U 5f" representing the localized 5f electrons [Ito02][10].

Finally, we note that the uranium spacing in UGe_2 is $d_{U-U} = 3.85$ Å which is above the Hill limit[11] of 3.6 Å. Therefore, without hybridization with other electrons, the f electrons would be localized.

[8]The parallel and transverse component of the fluctuating moment are considered equal. This is not true for UGe_2 where spin fluctuations shows Ising character.

[9]A comparison of the results from the Stoner model and the spin fluctuation model can be found in [Mohn02], chapter 18.

[10]Earlier photoemission experiments shows the presence of narrow peak in the density of states below E_F [Soda91, Ishii93]

[11]Hill has realized a systematic study of uranium compounds as a function of uranium spacing d_{U-U}. He found that for $d_{U-U} < 3.4$ Å, the ground state is paramagnetic which is interpreted by the overlap of the 5f orbitals. For $d_{U-U} > 3.6$ Å, the ground state is magnetic, which is interpreted by the result of local magnetic moments. The region 3.4 Å $< d_{U-U} <$ 3.6 Å, is the critical region

3.4 The T_x Anomaly at Ambient Pressure

In addition to the well defined anomaly observed at $T_C = 52$ K, a second feature is observed at lower temperature between 20 K and 35 K. For example in the temperature dependence of the specific heat represented in fig. 3.4, the discontinuity at 52 K is caracteristic of the second order transition from the paramagnetic (PM) to the ferromagnetic (FM) state. But there is also a marked hump around 28 K. In the fig. 3.5 is represented the thermal expansion coefficients along the a, b and c axis. The second order PM-FM transition is again detected as a discontinuity at 52 K. By contrast, the anomaly at T_x is found at 3 different temperatures between 20 to 28 K depending on the crystallographic axis. A summary of the experimentally observed effects is presented in the table 3.1. The variety of temperature has to be compared with the differences observed for the Curie temperature, which are less than 1 K. Thus, the feature at T_x is not a genuine phase transition[12]. No anomaly is detected in the magnetization data at ambient pressure [Tateiwa01a, Huxley01, Pfleiderer02].

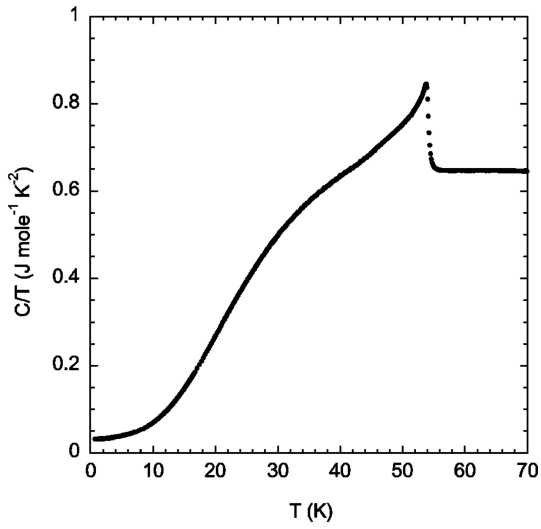

Figure 3.4: The temperature dependence of the specific heat C divided by the temperature T [Huxley01].

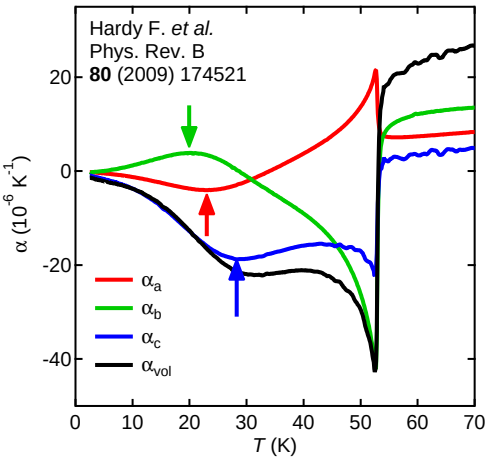

Figure 3.5: Temperature dependence of the thermal expansion coefficients along the a, b and c axis and volume. The anomaly at T_x is indicated by arrows for the 3 axis [Hardy09].

New information will arise from the p-T phase diagram together with magnetization measurements under pressure.

3.5 The p-T Phase Diagram

A historical evolution of the p-T phase diagram of UGe_2 is presented in fig. 3.6. We can see on this figure the phase diagram reported from the first pressure work in 1993 [Takahashi93]. The Curie temperature decrease with pressure and the ferromagnetic order disappears at a critical pressure p_c between 1.5 and 2 GPa. One year later, p_c is located between 1.8 and 2 GPa [Nishimura94]. The pressure evolution of the anomaly at T_x was first reported in 1998 [Oomi98]. In this report, the critical pressure p_c is however lower

[12]During the time of this study, thermal expansion measurements under pressure have been reported [Kabeya09]. The anisotropy of T_x at 1.1 GPa is much smaller than at ambient pressure : a minimum is observed at 6 K in the thermal expansion coefficient along the a and b-axis, and at 5 K along the c-axis.

T_x (K)	physical quantity	description	anisotropy	references
32	$d\rho/dT$	broad maximum	$J//c$	[Oomi95, Oomi98] [Tateiwa01b]
32		broad maximum	polycrystal	[Bauer01]
28	C	broad maximum		[Huxley01, Hardy09]
28	κ	maximum	$\Delta T//a$	[Misiorek05]
20		maximum	$\Delta T//c$	
		hardly detected	$\Delta T//b$	
35	R_0	sharp minimum		[Tran04]
23	α_a	minimum	a-axis	[Hardy09, Oomi93]
20	α_b	maximum	b-axis	
28	α_c	minimum	c-axis	
31	α	minimum	volume	
~ 30	c_{11}	broad minimum	$q//a$, $u//a$	[Kuwahara07]
	c_{66}	hardly detected	$q//a$, $u//b$	
	c_{55}	hardly detected	$q//a$, $u//c$	

Table 3.1: Dependence of the T_x temperature on the different physical quantities : $d\rho/dT$ is the temperature derivative of the resistivity, C is the specific heat, κ is the thermal conductivity, R_0 is the ordinary Hall effect coefficient, α is the thermal expansion coefficient, c_{ii} are the elastic constants for sound propagation along q and polarization along u.

than 1.5 GPa. Superconductivity was discovered under pressure in 2000 by S. Saxena *at al.* [Saxena00] inside the ferromagnetic phase just below the critical pressure p_c where the Curie temperature vanishes. In 2001, based on a study on polycrystals, the anomaly at T_x was found to disappear at the same pressure p_c [Bauer01]. However, other studies, on single crystals, found a lower critical pressure p_x for the T_x anomaly. The maximum of T_{sc}, the superconducting temperature, was found to be close to p_x. Measurements of the magnetization under pressure identified the T_x anomaly as a transition from a small moment phase FM1 to a large moment phase FM2. After 2002, refinements of the p-T superconducting phase diagram have been done and will be presented later. It is interesting to remark in the fig. 3.6 the differences in the determination of p_c. Due to its proximity with the superconductivity, the critical pressure in UGe_2 has been widely studied, allowing for comparison. Even in the recent studies, p_c is given between 1.5 and 1.6 GPa, depending on the authors. Despite the fact that it is possible to measure a change of pressure as small as 0.01 GPa (see fig. 2.13 page 29), systematic errors arise from the thermometry calibration, remanent fields, non-hydrostatic components....

Measurements of magnetization under pressure revealed that the ground state below the critical pressure p_x is a ferromagnetic phase with a magnetic moment of $1.5\mu_B/U$. This ground state is called FM2. Above p_x the saturated moment is only $0.9\mu_B/U$. This different ground state is called FM1. It was first measured in 2001 in a SQUID magnetometer (see fig. 3.7) [Tateiwa01a] and confirmed later [Motoyama01, Pfleiderer02], also by neutron diffraction (see fig. 3.8) [Tateiwa01a, Huxley01, Aso06a].

The transition at p_x is very sharp, as can be seen in fig. 3.9 [Pfleiderer02][13]. The

[13]In [Motoyama01], the change from FM2 to FM1 is rather continuous. Magnetization has been measured down to 0.35 K by VSM with fluorinert and with a sample of RRR $290 - 270$. However, such continuous change has never been confirmed.

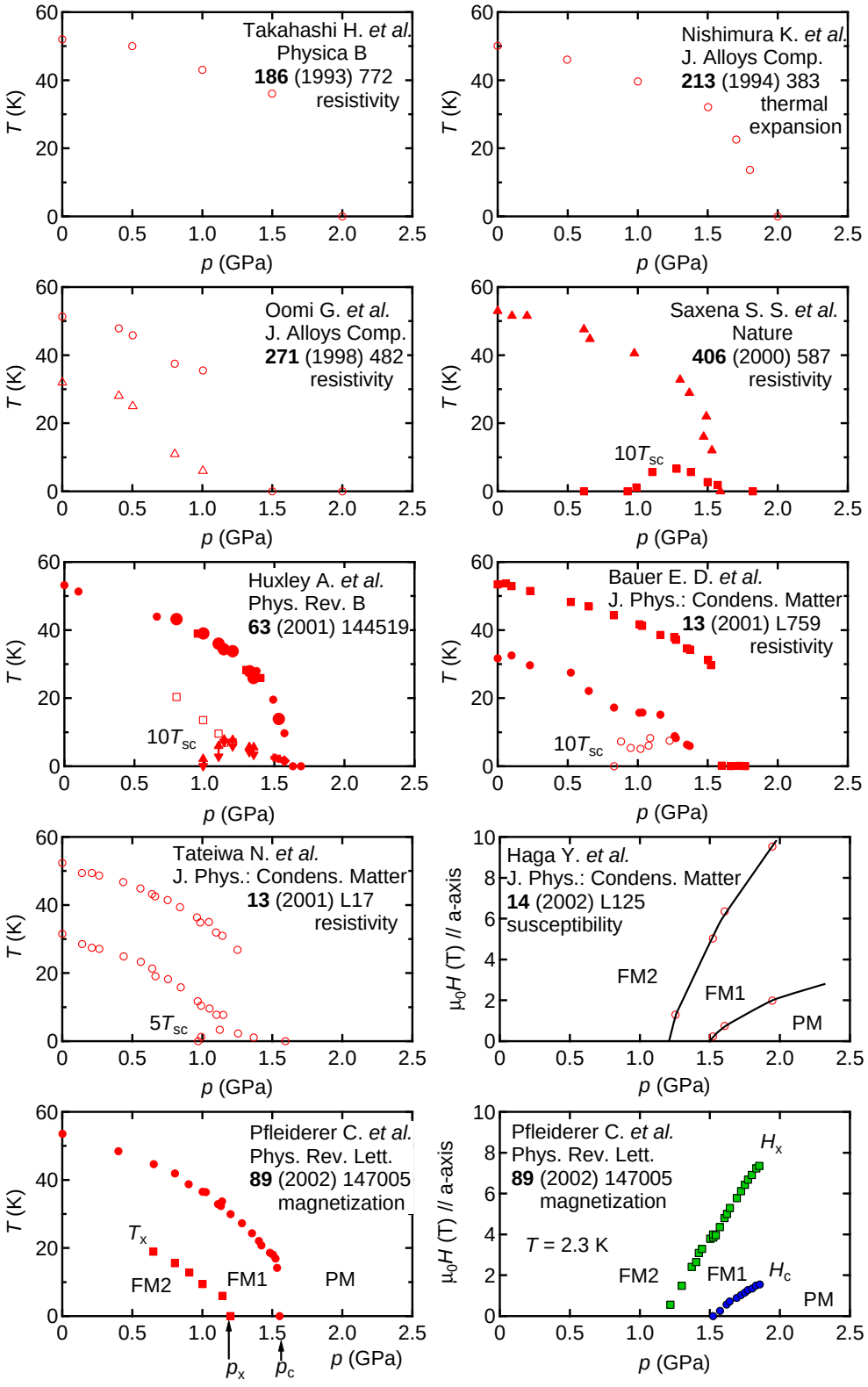

Figure 3.6: Historical evolution of the pressure-temperature phase diagram of UGe_2. The pressure evolution of T_x is reported since 1998, and the superconductivity has been discovered in 2000. In 2001, the anomaly at T_x is drawn carefully and disappears at p_x below p_c. In 2002, the transition at T_x was identified as a transition from a small moment phase FM1 to a large moment phase FM2. After 2002, refinements of the p-T phase diagram concerning the superconducting phase have been done and will be presented later.

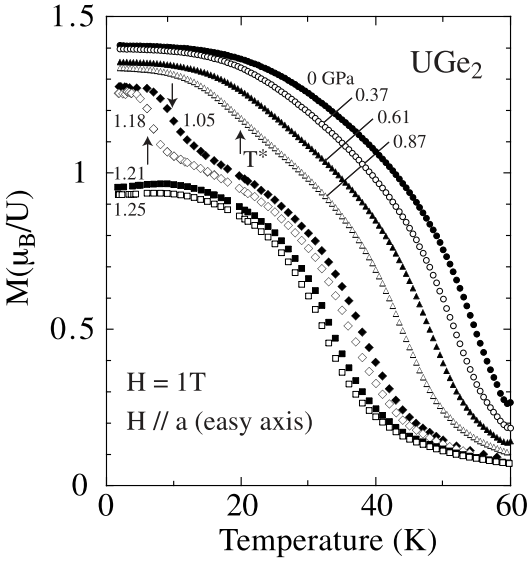

Figure 3.7: Temperature dependence of the magnetization at different pressure for a magnetic field of 1 T along a-axis. Measurements are carried out in a SQUID magnetometer [Tateiwa01a]. T^* is referred as T_x in the text.

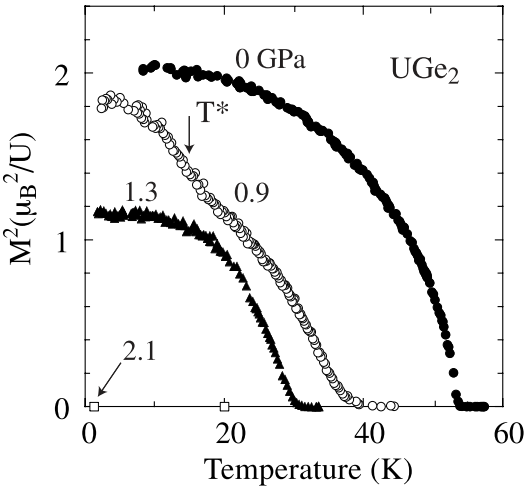

Figure 3.8: The temperature dependence of the squared magnetic moment measured by the (001) Bragg intensity of neutron scattering experiment [Tateiwa01a]. T^* is referred as T_x in the text. The same result was already reported in [Huxley01].

ordered magnetic moment reduces from $1.5\mu_B/U$ in the FM2 phase (below p_x) to $0.9\mu_B/U$ in the FM1 phase (above p_x). This discontinuity of the magnetization which is a first-order derivative of the free-energy ($M = -\frac{\partial F}{\partial B}$) lead to the conclusion that the FM1-FM2 transition is first order at low temperatures.

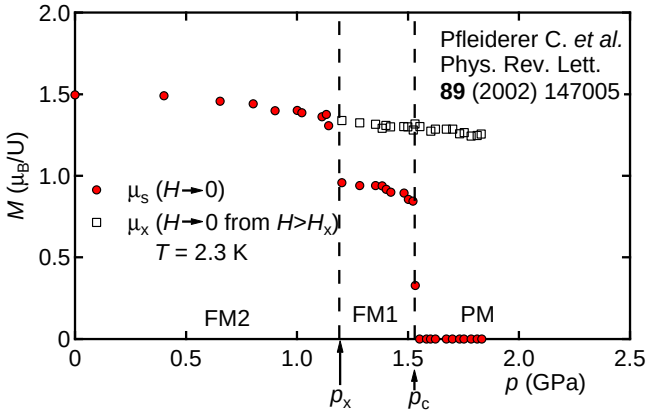

Figure 3.9: Pressure dependence of the magnetic moment at zero field at 2.3 K (full circles). The moment obtained by extrapolating the data from above H_x to zero field is also shown when it is different (open squares) [Pfleiderer02].

3.6 Metamagnetism Between p_x and p_c

In the FM1 phase, i.e. for pressure $p_x < p < p_c$, an applied magnetic field along the easy magnetization axis (a-axis) above a critical field H_x, will induce the FM2 phase (see figs. 3.9, 3.10 and 3.11) [Tateiwa01a]. Generically, a rapid increase of the magnetization

over a narrow region of applied field is called a metamagnetic transition. But in UGe_2 it can more precisely be called the FM1-FM2 transition.

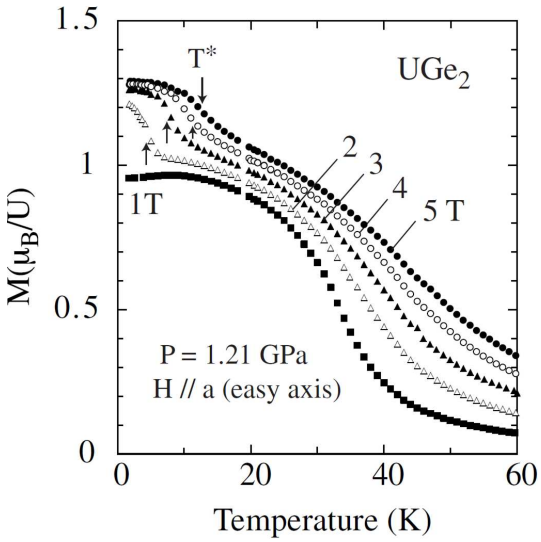

Figure 3.10: Temperature dependence of the magnetization at 1.21 GPa under various magnetic fields along the a-axis. Measurements are carried out in a SQUID magnetometer [Tateiwa01a]. T^* is referred as T_x in the text.

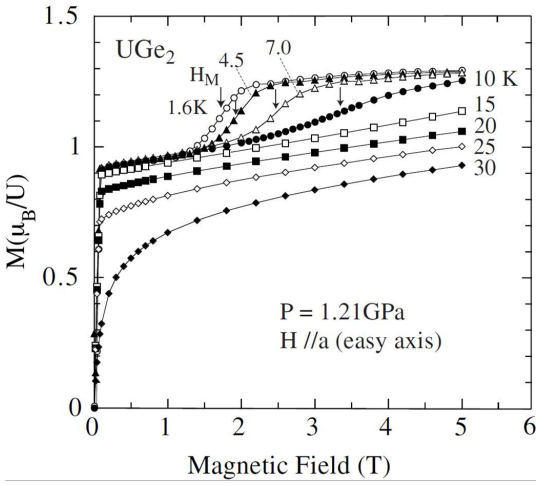

Figure 3.11: Magnetic field dependence of the magnetization at 1.21 GPa for different temperatures. Measurements are carried out in a SQUID magnetometer [Tateiwa01a]. H_M is referred as H_x in the text.

3.7 Different Scenarios for the T_x Anomaly

One scenario considers that the anomaly at T_x may be related to a coupled spin and charge density wave instability [Watanabe02]. This would create imperfect nesting of the Fermi surface. In the case where the majority spin band is located inside the nesting zone, an increase of the magnetization can be explained[14]. Moreover, the optical phonon are subject to the Kohn anomaly [Kohn59] due to the nesting. It can explain the T_x anomaly revealed in the specific heat by a broad hump. In this scenario, the superconductivity can be mediated by the coupled spin and charge density wave fluctuations. The nesting is supported by electronic structure calculations which predict a dominant cylindrical Fermi surface sheet with nesting around $(0.45\frac{2\pi}{a}, 0, 0)$ [Shick01].

However, no direct microscopic evidence of a density wave instability has been observed [Huxley01, Kernavanois01, Huxley03b, Aso06b]. In such a scenario a Kohn anomaly should occur in the phonon spectrum as observed for α-U [Marmeggi99]. However, no significant evolution of the lattice dynamics with temperature or evidence for a soft mode has been found in the phonon spectrum [Raymond06]. Similarly, large elastic softening was measured at the CDW-SDW transition in α-U [Fisher61], but it was not the case in UGe_2 [Kuwahara07].

[14]This can be understood as follows. In the case of perfect nesting, an energy gap opens on the whole Fermi surface. If the density of state $D(\epsilon)$ is symmetric with respect to the Fermi energy ϵ_F, the magnetization does not change. In the case of imperfect nesting, an energy gap opens only on the zone boundary transfered by the nesting vector Q. These part will not contribute to the magnetization change, as for the perfect nesting case. However, the part of the Fermi surface which deviate from the nesting zone boundary, i.e. the part where the gap does not open, will shift by the gap creation. The shift is downward if they are inside the nesting zone boundary, and upward if they are outside.

Another idea is that these two magnetic phases are related to singularities in the density of states [Sandeman03]. It is shown that the low dimensionality of the band structure necessarily induces two peaks in the density of states (see fig. 3.12) [Sandeman02]. Such sharp double peak in the density of states near the Fermi energy E_F can induce a first order Stoner-type phase transition in the spin magnetization (see fig. 3.13). The low dimensionality of the band structure is inspired by De Haas van Alphen (dHvA) quantum oscillatory studies and bandstructure calculations (see section 3.10). These studies reveal a quasi two dimentional Fermi surface. Futhermore there is the possibility that large sections of the quasi-two-dimentional Fermi surface may be parallel, making it almost one-dimentional.

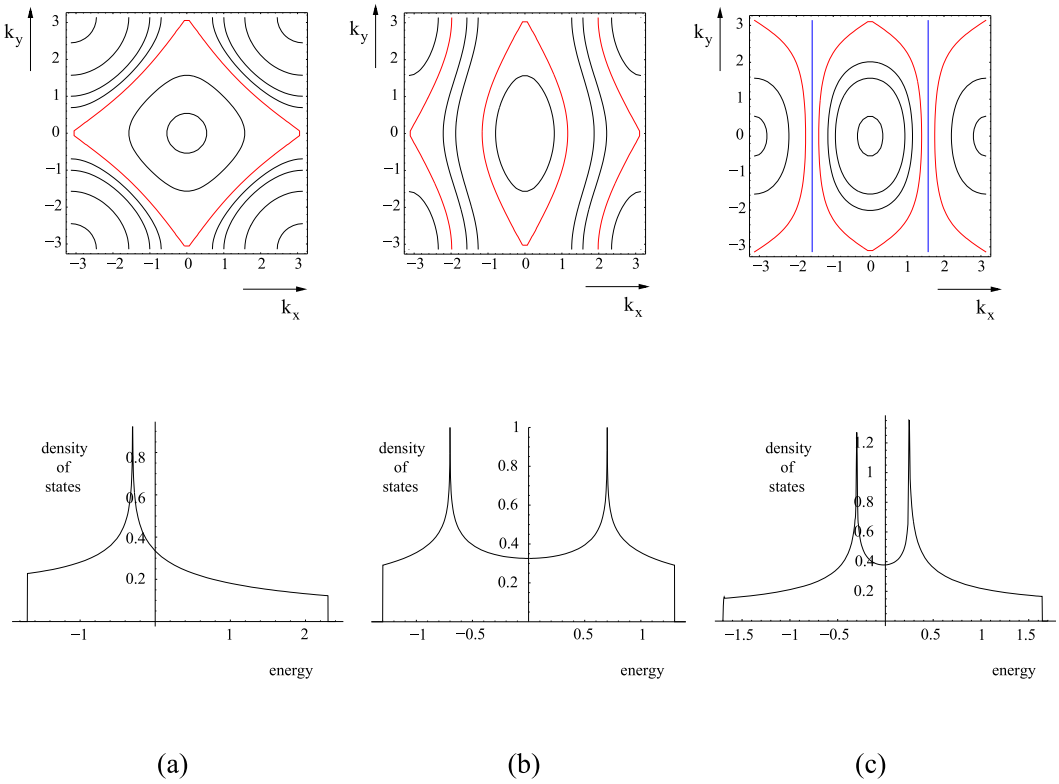

Figure 3.12: Two dimensional and quasi-one-dimensional tightbinding bandstructures : contour plots (top row of figures) with the van Hove contours shown in red and associated densities of states (bottom row). In (a) the two-dimensional structure used for some cuprates and given by $\epsilon(\mathbf{k}) = -\alpha_x \cos(k_x) - \beta \cos(k_x)\cos(k_y) - \alpha_y \cos(k_y)$ is shown with $\alpha_x = \alpha_y = 1$ and $\beta = -0.3$. In (b) the quasi-one-dimensional structure used for some organic superconductors and given by $\epsilon(\mathbf{k}) = -\alpha_x \cos(k_x) - \alpha_y \cos(k_y)$ is shown with $\alpha_x = 1$, $\alpha_y = 0.3$. In (c), higher harmonics in the principal direction are included $\epsilon(\mathbf{k}) = -\alpha_x \cos(k_x) - \beta \cos(k_x)\cos(k_y) - \gamma \cos(2k_x) - \delta \cos(3k_x)$ with $\alpha_x = 1$, $\beta = 0.7$, $\gamma = 0.03$ and $\delta = -0.03$. We see that in (a) there is one (degenerate) van Hove contour, but on going into quasi one-dimension, we lift this degeneracy and find two van Hove contours and hence two maxima in the density of states. Furthermore, the choice of bandstructure in (c) has an optimal nesting scenario (shown in blue) which is separate from both of the van Hove contours, due to the elimination of the $\cos(k_y)$ term in the bandstructure [Sandeman02].

The last scenario is based on the LSDA+U electronic structure calculations [Shick04]. These calculations result in two nearly degenerate solutions, which differ in terms of magnetic moment, as FM1 and FM2. In this picture, a competition between spin-orbit coupling and crystal-field effects leads to FM2 and FM1 respectively. The ordered moment is identified as the sum of opposing spin and orbital contributions, with a large orbital

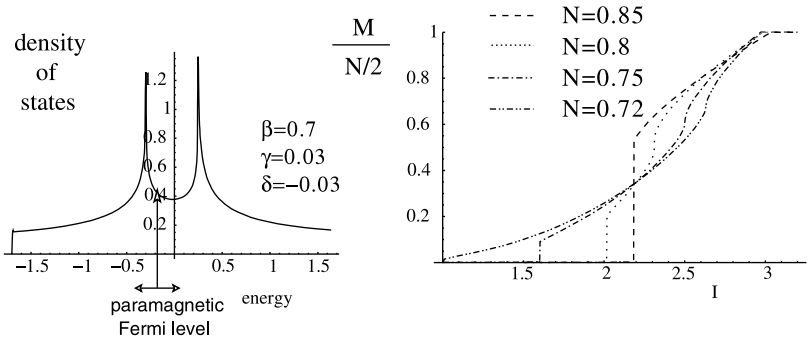

Figure 3.13: Calculated density of states for the tight-binding bandstructure $\epsilon(\mathbf{k}) = -\alpha_x \cos(k_x) - \beta\cos(k_x)\cos(k_y) - \gamma\cos(2k_x) - \delta\cos(3k_x)$ with $\alpha_x = 1$, $\beta = 0.7$, $\gamma = 0.03$ and $\delta = -0.03$ (see fig. 3.12(c)). The calculated graphs of magnetisation as a function of I, the Stoner exchange parameter for various levels of band-filling, below half-filling is presented on the right panel. Two magnetic transitions are visible. Ref. [Sandeman02] contains examples for further DOS parameters [Sandeman03].

part. In this scenario, the superconductivity can be mediated by orbital (and spin) wave fluctuations.

3.8 First Order Transition at p_c

The first-order nature of the transition at p_c is confirmed by the discontinuity of the magnetization, which is a first-order derivative of the free-energy ($M = -\frac{\partial F}{\partial B}$) (see fig.3.9 [Pfleiderer02]). Further evidence is provided from a phase separation observed at 1.5 GPa, very close to p_c [Kitaoka05], although this can also be the result of a pressure gradient. Quantum oscillatory studies reveal a discontinuous change of the Fermi surface across p_c [Terashima01, Settai02].

Critical magnetic fluctuations associated with a second-order QCP do not exist in UGe_2 near p_c. Fermi liquid behavior is observed by a T^2 dependence of the resistivity even near p_c [Takahashi93, Huxley01, Terashima06][15]. No clear enhancement of ρ_0 is observed near H_x and H_c [Terashima07] although it is theoretically expected near a quantum critical point [Miyake02].

3.9 Metamagnetism above p_c

In the paramagnetic phase above p_c, an applied magnetic field along the easy magnetization axis (a-axis) above a critical field H_c, will induce the FM1 phase (see fig. 3.14) [Huxley00, Terashima02, Pfleiderer02, Haga02]. The transition at H_c is similar to the one at H_x (see sec. 3.6), namely a rapid increase of the magnetization over a narrow region of applied field. Therefore, it is also called a metamagnetic transition, but in UGe_2 it can more precisely be called the PM-FM1 transition.

Note that above H_c, the FM1-FM2 transition is still visible at H_x.

Usually, no hysteresis is observed at H_x or H_c [Terashima06] but a hysteresis of a few mT at both H_x and H_c is mentioned in [Pfleiderer02].

[15]Early measurements in [Oomi98] reported a critical behavior (divergence of the A coefficient of the T^2 term of the resistivity), but the pressure steps were too large.

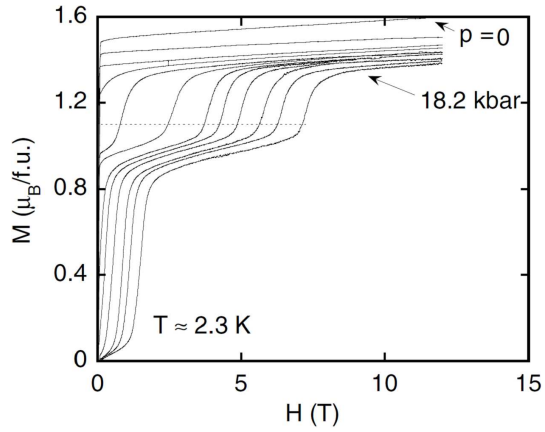

Figure 3.14: Magnetic field dependence of the magnetization at 2.3 K for different pressures [Pfleiderer02].

3.10 Fermi Surface Studies under Pressure

De Haas-van Alphen (dHvA) quantum oscillatory studies have been carried out under pressure for magnetic fields applied along the b axis [Terashima01, Settai02], along the a axis [Terashima02, Haga02] and along the c axis [Settai03] in a field range between 5 to 17 T. All these studies revealed a drastic change of the Fermi surface between the ferromagnetic state and the paramagnetic state.

In the FM2 state, the main Fermi surfaces are highly corrugated but cylindrical along the b axis. This is not surprising considering the anisotropic crystal structure which is long along the b axis (see section 3.1), implying a flat Brillouin zone which can easily be touched by the Fermi surface. The measured cyclotron masses are in the range $15-23m_0$ and slightly increase under pressure (see fig. 3.15(b)). In the FM1 state, the dHvA signal disappears completely for a field applied along the b axis [Settai02, Settai03], and two branches with small dHvA frequencies are detected with cyclotron mass $8-11m_0$ for field applied along a axis [Haga02] (see fig. 3.17). The difficulty in observing dHvA oscillations in the FM1 phase is explained by the large γ term of the specific heat (see section 3.11.4) which suggests high cyclotron masses that are difficult to detect. Moreover, it could be due to the Fermi surface becoming open, in agreement with the scenario of the double peak in the density of states (see fig. 3.12)[Sandeman02].

The process by which the small dHvA branches in the FM1 phase are connected to those in the FM2 phase has not been identified [Haga02], which is not surprising considering the first order nature of the transition. The same observation is made for the transition between the FM1 and the PM state.

In the PM state, the measured cyclotron masses for field applied along the b axis are in the range $40-65m_0$ [Terashima01, Settai02]. As visible in fig. 3.15, the measured dHvA frequencies and cyclotron masses do not connect with the one measured in the FM state. It reveals a drastic change of the Fermi surface. However, no angular dependence has been performed under pressure.

Band structure calculations indicate a quasi-two-dimensional geometry of the Fermi surface with mostly spin majority character [Shick01]. By performing calculations for different values of the lattice constant, two nearly degenerate states have been obtained, providing a new scenario for the FM1-FM2 transition (see section 3.7).

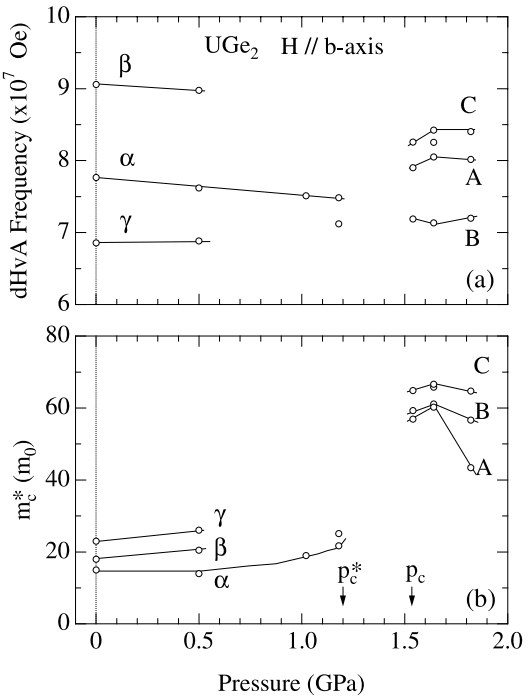

Figure 3.15: Pressure dependence of (a) the dHvA frequency and (b) the cyclotron mass detected for field along b axis [Settai02]. p_c^* is refered to as p_x in the text. The dHvA signal disappears completely in the FM1 phase between p_x and p_c.

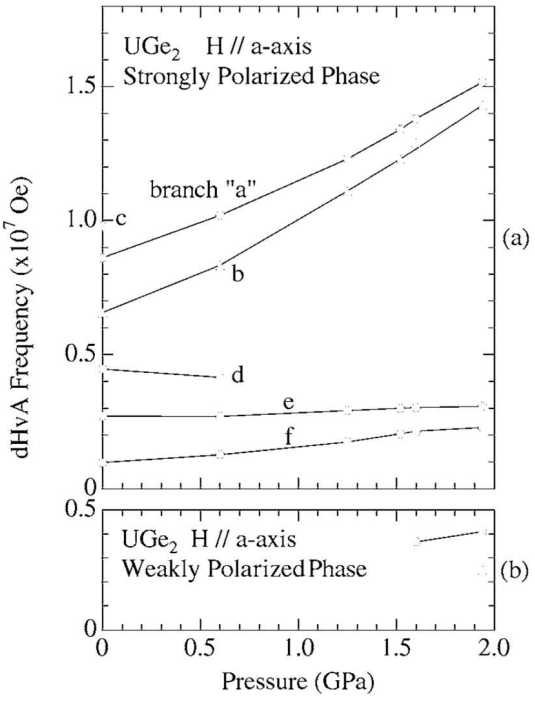

Figure 3.16: Pressure dependence of the dHvA frequency in (a) the strongly polarized phase FM2 and (b) the weakly polarized phase FM1 for field along a axis [Haga02]. These phases can be observed at high pressure because they are induced by the magnetic field along a axis.

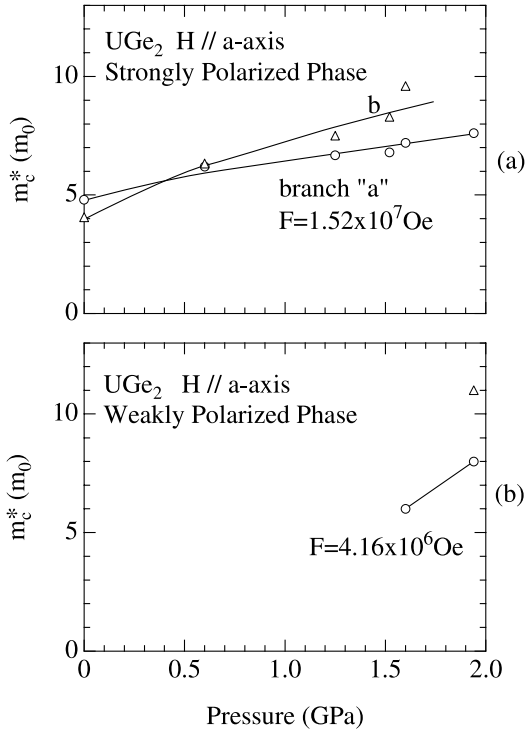

Figure 3.17: Pressure dependence of the cyclotron mass in (a) the strongly polarized phase FM2 and (b) the weakly polarized phase FM1 for field along a axis [Haga02]. These phases can be observed at high pressure because they are induced by the magnetic field along a axis.

3.11 The Superconducting Phase

Inside the ferromagnetic phase from ~ 0.9 GPa to p_c, the resistivity and AC susceptibility show a superconducting transition : a sudden and complete loss of resistivity below T_{sc} in the millikelvin range and the AC susceptibility tends to the limit of -1 (in SI units) [Saxena00].

3.11.1 Bulk Superconductivity

The critical current density $j_c \approx 0.1$ A.cm^{-2} is two orders of magnitude smaller than for heavy-fermion systems such as UPt_3 [Kambe99]. Above the critical current, a linear response of the voltage versus current measurements was obtained, with a differential resistance $r = \frac{dV}{dI}$ well below the resistance r_N of the normal state[16] [Huxley01]. This is expected for a bulk flux flow resistivity[17] [Hu72]. The flux lattice is expected to form spontaneously even at ambient field due to the internal field (the ordered moment corresponds to ~ 0.2 T)[18].

Less ambiguous evidence for bulk superconductivity in UGe_2 was provided by the specific heat, which shows a small yet distinct anomaly (see fig. 3.18). The biggest anomly can be observed in fig. 3.18(d) in the measurement at 1.22 GPa. The fig. 3.18(f) shows the pressure dependence of the superconducting transition temperature T_{sc} determined by resistivity. It is compared to the pressure dependence of the heat capacity anomaly in the form $\frac{\Delta C}{\gamma_n T_{sc}}$. We can see that in contrast to the resistivity (and the AC susceptibility), the specific heat anomaly is found in a very narrow pressure range around p_x [Tateiwa04]. This feature will be discussed in section 3.11.4. The anomaly is also rapidly suppressed under magnetic field (see fig. 3.18(e)) [Tateiwa02]. Since new measurements of the specific heat will be reported in this manuscript, an exhaustive compilation of all reported measurements of specific heat at the superconducting transition is shown in fig. 3.18. The specific heat measurements were performed on two single crystals from the same ingot with $RRR \approx 600$ with the adiabatic heat pulse method in a CuBe piston-cylinder cell with a Daphne oil (7373) as a pressure-transmitting medium [Tateiwa01b, Tateiwa02, Tateiwa04] or on a polycrystal with a methanol/ethanol mixture as pressure-transmitting medium [Vollmer02].

Finally, the superconducting signal has been observed in ^{73}Ge-NQR experiments (see [Kotegawa05, Harada05, Harada07] and fig. 3.19).

[16] For filamentary superconductivity, a linear response is not expected but instead an increase with the current since it would exceed the critical value for successive filaments. The normal state resistance would be rapidly approached.

[17] A current in a superconductor in the mixed state will induce a Lorentz force on the vortices $F_{L_V} = J \wedge B$ per unit volume or $F_{L_l} = J \wedge \Phi_0$ per unit length of vortex. If the vortices can move with a velocity v, it will induce an electrical field $E = v \wedge B$ and thus a resistance. If the vortices can be prevented from moving and become pinned, no resistance is induced. The critical current is the value of the current at which the vortices will begin to move, i.e. when the Lorentz force F_L will overcome the pinning force F_p. The flux flow resistance is lower than the normal state resistance.

[18] It can be calculated with $\mu_0 M = \mu_0 \frac{N_U}{V} m$ where $N_U = 4$ is the number of uranium atom in a unit cell, $V \approx 2.48 \times 10^{-28}$ is the volume of the unit cell calculated from ref. [Oikawa96], m is the magnetic moment. It gives 0.28 T in the FM2 phase where $m = 1.5\mu_B$/U and 0.17 T in the FM1 phase where $m = 0.9\mu_B$/U

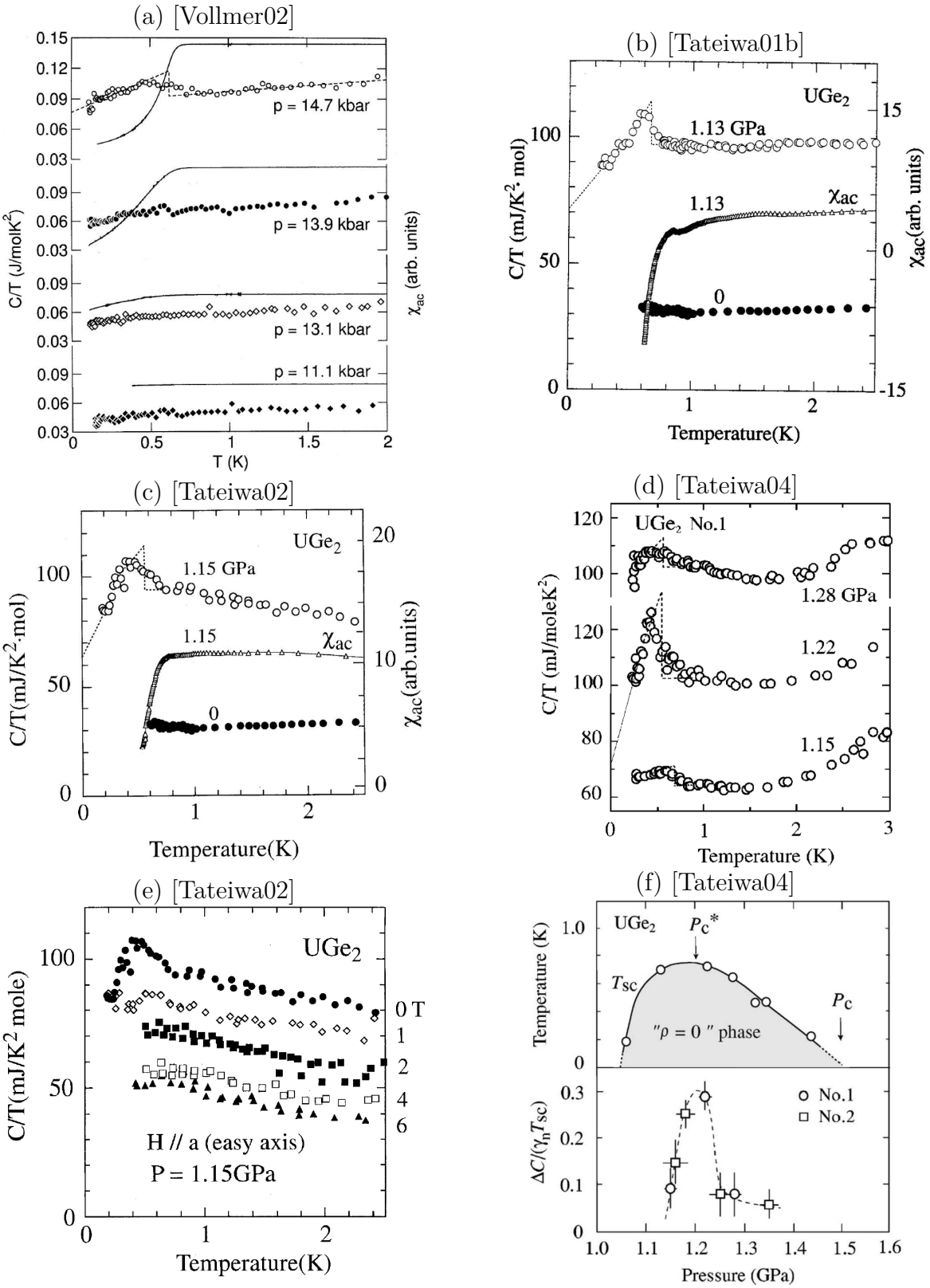

Figure 3.18: All published data concerning the specific heat anomaly at the superconducting transition. The temperature dependence of C/T is plot at different pressures and in (a) to (d), and at different magnetic field applied along the a-axis at 1.15 GPa in (e). The AC susceptibility is also shown in (a) to (c). In (f) is plot the pressure dependence of the superconducting transition temperature T_{sc} determined by the resistivity measurement (upper panel) and the value of $\frac{\Delta C}{\gamma_n T_{sc}}$ (the lower panel). The P_c^* is referred as p_x in the text.

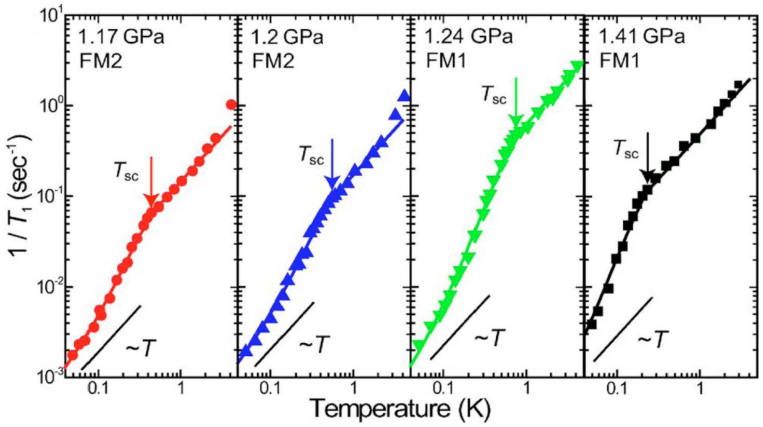

Figure 3.19: Temperature dependences of $1/T_1$ for FM2 at $p = 1.17$ and 1.2 GPa measured at $f = 7.68$ MHz and for FM1 at $p = 1.24$ and 1.41 GPa measured at 7.09 and 7.07 MHz, respectively [Harada07].

3.11.2 Evidence for the Coexistence of Ferromagnetism and Superconductivity

Despite the fact that the superconductivity is a bulk property, the persistence of ferromagnetism in the superconducting phase was observed by neutron diffraction [Huxley01, Huxley04, Aso05][19].

In addition, the evidence of the homogeneous coexistence of ferromagnetism and superconductivity is given by the observation of the superconducting signal at the ferromagnetic site in ^{73}Ge-NQR experiments. The spin-lattice relaxation rate shows a change in slope at T_{sc} [Kotegawa05, Harada07]. The signal was observed at $f = 7.68$ MHz corresponding to the Ge1 site in FM2 phase for $p < p_x$ and at $f = 7.07 - 7.09$ MHz corresponding to the Ge1 site in FM1 phase for $p > p_x$ (see fig. 3.19).

3.11.3 Non-BCS Superconductivity

Whatever the pairing mechanism, odd-parity spin triplet superconductivity is expected since the spin majority and minority Fermi surfaces are strongly split in the ferromagnetic state.

In ^{73}Ge-NQR experiments, the decrease of the spin-lattice relaxation rate $1/T_1$ below T_{sc} without any indication of a coherence peak has been interpreted with a line-node gap model [Kotegawa05]. In [Harada07], the experimental results are well described by a nonunitary spin-triplet pairing model [Ohmi93, Machida01, Linder08], where the superconducting energy gap opens only in the majority spin band parallel to the magnetization, but not in the minority spin band which remains gapless.

The jump of specific heat ΔC at T_{sc} is : $\frac{\Delta C}{\gamma_n T_{sc}} \approx 0.2 - 0.3$ [Tateiwa04]. This value is small compared to a BCS value of 1.45. A reduced jump can occur for several reasons [Huxley04] :

- the presence of nodes in the order parameter.
- the presence of a finite field due to ferromagnetism (the ordered moment corresponds to ~ 0.2 T).

[19] In the FM2 phase in [Huxley04].
In the FM2 phase at 1.1 GPa and in the FM1 phase at 1.25 GPa in [Aso05].

- the jump results in the contribution of 2 bands of different polarization of the spins. One of the spin band can be almost ungapped, i.e. a small gap value. The minority spin band is often proposed [Huxley04, Kotegawa05, Harada07].
- extrinsic pair breaking due to non-magnetic impurities and defects.
- intrinsic pair breaking due to some part of the electron-electron scattering which is significant in heavy-fermions.
- spatial inhomogeneity of the superconductivity due to magnetic domain boundaries. The superconducting anomaly is rapidly suppressed under magnetic field applied along the magnetization axis (see fig. 3.18(e)) [Tateiwa02]. However, our results presented in chapter 5 show that the superconducting transition is still visible at fields up to 1.3 T (at 1.27 GPa for example), which is much higher than the field necessary to align magnetic domains (< 0.02 T [Pfleiderer02]).

So far, the strongest evidence supporting p-wave superconductivity comes from studies of the upper critical field H_{c_2} [Sheikin01]. Unusual positive curvatures of $H_{c_2}(T)$ have been observed for a field applied along the c-axis [Sheikin01] and the b-axis [Kobayashi02]. Such feature can be described in the strong-coupling scenario with high values of the coupling parameter λ. A simplified model of the pairing spectrum [Bulaevskii88] neglecting the gap anisotropy can fit the experimental data for $H^c_{c_2}$ only if the Pauli limit[20] is excluded in the calculation [Sheikin01]. Such absence of the Pauli limit in UGe_2 is consistent with certain spin triplet states. Indeed, there are 3 possible triplet states (total spin $S = 1$) : $S_z = 1$, $|\uparrow\uparrow\rangle$; $S_z = 0$, $|\uparrow\downarrow\rangle + |\downarrow\uparrow\rangle$ and $S_z = -1$, $|\downarrow\downarrow\rangle$. The equal spin pairing corresponds to $|\uparrow\uparrow\rangle$ and $|\downarrow\downarrow\rangle$ as the A phase or planar phase of He^3. The A1 and β phases would also be possible in a fully polarized case.

Superconductivity has been observed in polycrystalline samples, but the purity of these samples remains high enough so that the mean free path is not significantly smaller than the coherence length [Bauer01]. A heat capacity anomaly has also been observed in polycrystals (see fig. 3.18(a) [Vollmer02]). The dependence of the superconducting temperature T_{sc} on sample quality is indicated by resistivity measurements on single crystals : for sample with RRR=60 at 1.26 GPa, $T_{onset} = 0.5$ K and $T_{\rho=0} = 0.1$ K which is compared to $T_{onset} = 0.55$ K and $T_{\rho=0} = 0.45$ K for RRR=600 [Tateiwa01b].

3.11.4 Influence of the FM1-FM2 Transition

As already mentioned, the specific heat anomaly is found in a very narrow pressure range around p_x [Tateiwa04] see fig. 3.18(f). In addition, the superconducting transition temperature T_{sc} shows a maximum around p_x. This is the reason why it has been often argued that the FM1-FM2 transition occurring at p_x plays an important role in the occurrence of the superconductivity. Moreover, the superconducting region follows the critical pressure p_x under a magnetic field [Nakane05]. However, not only p_x but also p_c plays a crucial role in the occurrence of superconductivity, since precise pressure tuning shows that T_{sc} increases on approaching p_c (see fig. 3.20)[Ban07].

[20]The Pauli limit also called paramagnetic limit or Clogston-Chandrasekhar limit [Clogston62, Chandrasekhar62], predicts a critical field $\mu_0 H_{p_0} = \frac{\sqrt{2}\Delta_0}{g\mu_B}$ where Δ_0 is the superconducting gap at $T = 0$ K and μ_B is the Bohr magneton : $\mu_B = \frac{e\hbar}{2m}$ where e is the elementary charge, $\hbar$ is the reduced Planck constant and m is the electron mass. In the case of BCS isotropic weak coupling, $\Delta_0 = 1.764 k_B T_{sc}$. Then assuming 2 for the g-factor, we obtain $\mu_0 H^{\mathrm{BCS,s}}_{p_0} = 1.86 T_{sc}$.

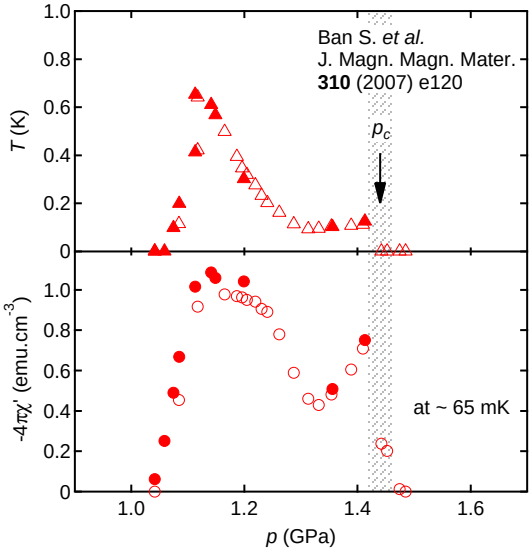

Figure 3.20: (a) Superconducting transition temperature T_{sc} as a function of pressure. T_{sc} is defined as a peak in the imaginary part of the AC susceptibility χ''. (b) $-4\pi\chi'$ at $\sim$ 65 mK as a function of pressure. Open (closed) symbols denote the measurements in increasing (decreasing) process of pressure[Ban07].

Below p_x, the coherence lengths derived from H_{c_2} are fairly isotropic and of the order of 100 Å. In contrast, above p_x, a marked anisotropy becomes apparent : at 1.5 GPa, $\xi_a \approx 210$ Å, $\xi_b \approx 140$ Å, and $\xi_c \approx 700$ Å[Sheikin01][21].

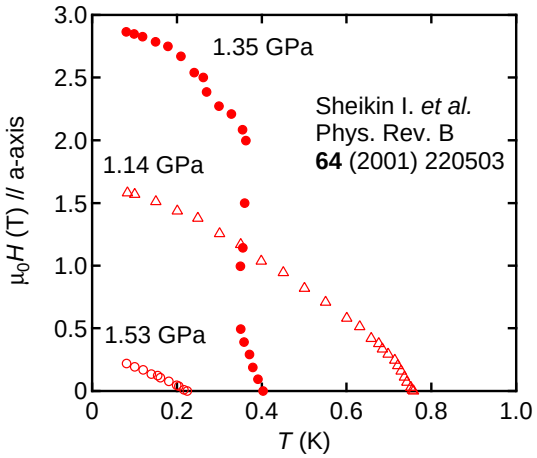

Figure 3.21: Upper critical field for an applied field parallel to the a axis at 3 different pressures. [Sheikin01, Huxley01]

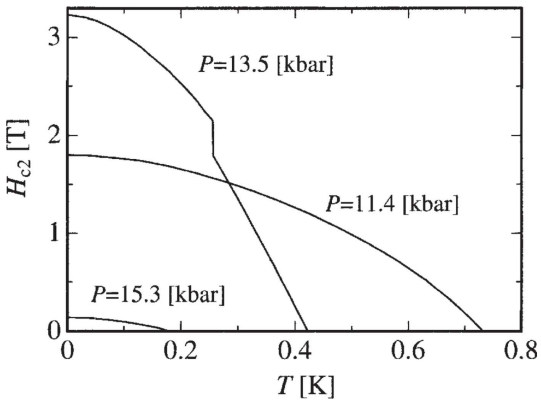

Figure 3.22: Upper critical field for an applied field parallel to the a-axis at 3 different pressures calculated on the basis of the strong coupling formalism. [Watanabe02]

For a magnetic field applied along the easy axis of the magnetization, a-axis, a reentrant behavior is observed in $H^a_{c_2}$. It is observed at a pressure above the critical pressure p_x (see fig. 3.21) and corresponds to the field induced FM1-FM2 transition at H_x. A reentrant-like behavior has also been observed in AC susceptibility [Nakane05] and during the time of this study [Kabeya09].

It has been interpreted as follows : if it is the fluctuations associated to the FM1-FM2 transition that drive the superconductivity, they will strengthen the superconductivity at H_x and thus explain the reentrant behavior. The coupled CDW and SDW fluctuations which mediate the pairing interaction have been proposed (see fig. 3.22) [Watanabe02].

Alternatively, the behavior can also be understood if there is a discontinuous change of T_{sc} between the FM1 and FM2 (see fig. 3.23) [Huxley03b]. In such a case, T_{sc} is expected to be higher in the FM2 phase than in the FM1 phase as drawn in the schematic

[21] For $p = 1.26$ GPa, $J//c$ and $H//a$, $T_{sc} = 0.45$ K and $Hc_2 = 1.9$ T from which $\xi = 130$ Å[Tateiwa01b].

phase diagram (see fig. 3.24) which has often been reproduced [Huxley03a, Hardy09]. Such a discontinuity has never been observed, but we note that an anomalous double transition is observed in AC susceptibility in refs. [Nakane05, Ban07] around p_x. However, during the time of this study, the same author group reported on new AC susceptibility measurements and concluded that the superconductivity is very likely extrinsic in the FM2 phase, probably induced by pressure inhomogeneity (see fig. 3.25) [Kabeya09].

The idea that the superconductivity has a higher T_{sc} in the FM2 phase and correspondingly a higher critical field is contradictory to the idea of an extrinsic nature of superconductivity in FM2.

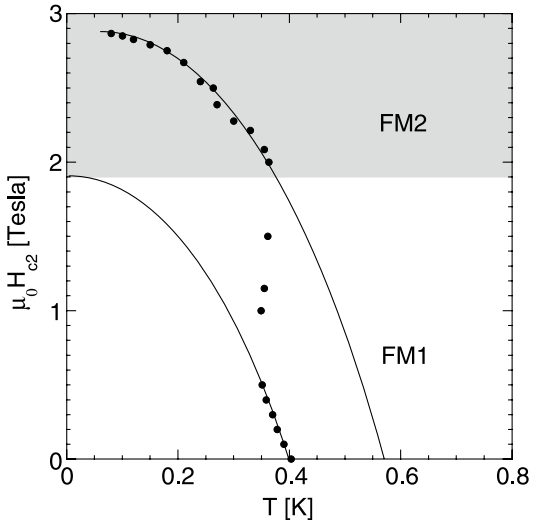

Figure 3.23: Upper critical field for applied field parallel to the a-axis from the mid-points of the superconducting transitions measured by resistivity at 1.35 GPa in [Sheikin01, Huxley01]. The position of the onset of the bulk FM1-FM2 transition seen in the resistivity in the normal phase at 1 K is also indicated as the lower limit of the shaded region. The lines serve only to guide the eye. [Huxley03b]

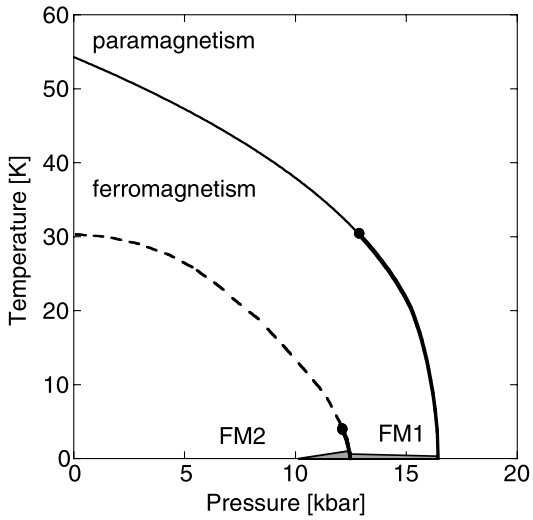

Figure 3.24: Schematic pressure versus temperature phase diagram of UGe_2. The thick curves represent first order transitions, thin curves second order transitions and the dashed curve a cross-over. The pressure-temperature region where superconductivity occurs is shaded [Huxley03b].

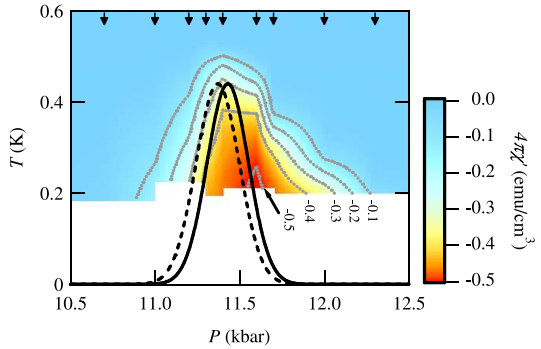

Figure 3.25: Real part of the AC magnetic susceptibility shown as a color-scale plot on the T-p plane. Dotted gray lines indicate contours. The solid and broken lines denote a pressure distribution function centered at p_x estimated from the AC magnetic susceptibility and the forced magnetostriction coefficient, respectively. Arrows indicate the pressures at which the susceptibility experiments were done [Kabeya09].

Another remarkable feature is that the superconductivity is observed in a pressure range where the γ_n term of the normal state is higher, also in agreement with the A coefficient of the resistivity. This indicates that a large mass enhancement of the quasiparticules is related to the superconductivity as observed for many heavy fermion compounds.

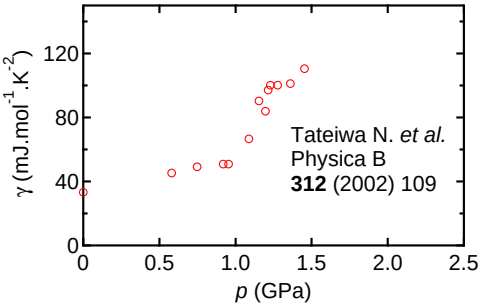

Figure 3.26: Pressure dependence of the γ term of the specific heat $C = \gamma T$ [Tateiwa02].

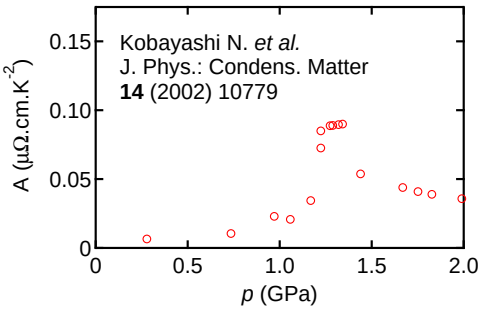

Figure 3.27: Pressure dependence of the A coefficient of the resistivity ρ obtained assuming a Fermi liquid behavior $\rho = \rho_0 + AT^2$ [Kobayashi02]. See also [Tateiwa01b, Bauer01, Terashima06].

3.11.5 No Superconductivity in the Paramagnetic Phase ?

Superconductivity has been theoretically predicted to occur on both sides of the critical pressure p_c, with a critical temperature T_{sc} reduced to 0 at the quantum critical point of a three-dimensional Heisenberg ferromagnet [Fay80]. A non zero value at the quantum critical point has been obtained in a more complete Eliashberg treatment using a three-dimensional Ising ferromagnet [Roussev01]. However, the early measurements has claimed that superconductivity is observed only in the FM side [Saxena00]. Different theories have explained an enhanced superconductivity in the ferromagnetic state, including the coupling of spin density and charge density wave [Watanabe02], special features of the density of states [Sandeman03] and coupling of the magnons to the longitudinal magnetic susceptibility [Kirkpatrick01].

Here the experimental evidence for such non observation of superconductivity in the paramagnetic phase is reviewed.

From AC susceptibility measurements, T_{sc} is claimed to be reduced to 0 K above p_c although careful examination of the curves reveals that T_{onset} is still visible at 1.56 GPa in χ'' and even at 1.61 GPa in χ' [Nakane05].

At a pressure $p = 1.5$ GPa, a phase separation is observed in the spectra of ^{73}Ge-NQR. Indeed, a peak at 8.51 MHz corresponding to the Ge1 site in the PM state is observed together with one at 8.37 MHz corresponding to the Ge1 site in the FM1 state[22]. This phase separation can occur from the first order nature of the PM-FM transition, but a pressure gradient cannot be ruled out [Harada05]. Interestingly, the superconducting signal indicated by a decrease in $1/T_1$ below T_{sc} is observed at the FM1 site but not at the PM one down to 40 mK (see fig. 3.28).

No superconductivity above p_c has been confirmed in ref. [Terashima06] from resistivity measurements with a sample of RRR_a=96 and down to 0.3 K.

No superconductivity was found down to 65 mK by AC susceptibility above p_c and up to $p_c + 0.4$ GPa [Ban07].

[22] Careful analysis of T_1 is required at 8.37 MHz because the spectra of FM1 overlap with those arising from the Ge1 and Ge2 sites remaining in the paramagnetic state [Harada05].

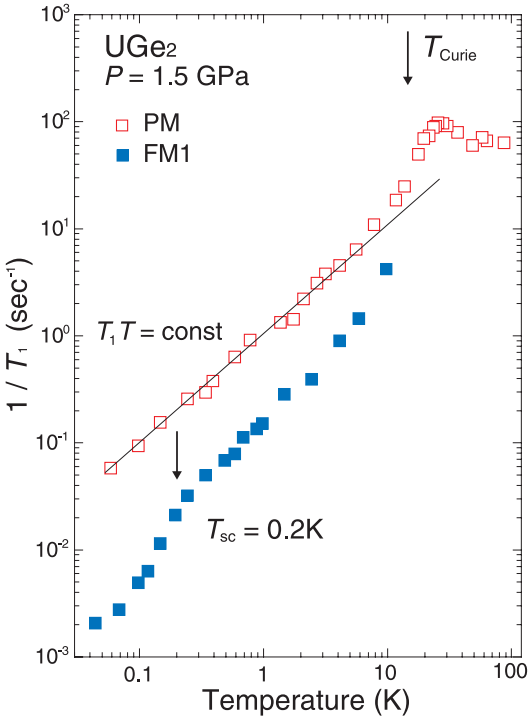

Figure 3.28: The temperature T dependence of $1/T_1$ for the paramagnetic (PM) phase (open squares) and FM1 phase (solid squares). The long components in $1/T_1$ for FM1 indicate that the superconductivity (SC) sets in at $T_{sc} = 0.2$ K, but the short components for PM do not [Harada05].

Chapter 4

Results on the Ferromagnetism of UGe_2

4.1 The Tricritical Point and the Wing Structure

Interest in UGe_2 arises from the coexistence of two usually competitive phenomena : superconductivity and ferromagnetism. However, in this section, only the ferromagnetic properties of UGe_2 will be discussed. Experimentally, it has been revealed that the paramagnetic (PM) to ferromagnetic (FM) transition becomes first order when the Curie temperature is driven to 0 K by tuning with pressure, chemical doping or magnetic field[1]. UGe_2 is one example as described in section 3.8. But the same observation can be made in $ZrZn_2$ [Uhlarz04]. In CoS_2, the Curie temperature can be tuned from 122 K to 0 K by Se doping and the PM-FM transition becomes first order in $Co(S_{1-x}Se_x)_2$ [Goto97]. This is also observed by tuning with pressure[2]. In $SrRuO_3$, the Curie temperature of 160 K can be reduced by Ca substitution [Khalifah04] and a first order transition is observed in $Sr_{1-x}Ca_xRuO_3$ [Uemura07]. Also in the helimagnet MnSi, the transition becomes first order before being suppressed under pressure [Uemura07]. In the helimagnet FeGe the transition is first order at ambient pressure [Lebech89] and suppressed around 19 GPa [Pedrazzini07].

This apparently generic result is in contrast with the theoretical prediction by Hertz [Hertz76][3] that the quantum ferromagnetic transition in metals should be of second order. The contrast is even more marked considering that the PM-FM transition usually serves to illustrate and explain a second order transition.

Different theories have been proposed to explain a first order PM-FM transition, including magneto-elastic coupling, effects of excitations at the Fermi surface, particular shape of the density of states and singularities of the Fermi surface. Theories dealing with the magneto-elastic coupling or with excitations at the Fermi surface seem more general than the ones considering special features of the density of states or the Fermi surface. However, the general behavior of the change from second to first order of the PM-FM transition is associated to a large diversity of fascinating phenomena. For example, ferromagnetic superconductivity is observed in UGe_2 [Saxena00], non-Fermi liquid behavior in $Sr_3Ru_2O_7$ [Grigera01] and MnSi [Pfleiderer97], a nematic phase in $Sr_3Ru_2O_7$ [Borzi07]....

4.1.1 Direct Consequence of a First Order Transition

In this section, it is shown that a wing structure phase diagram is a direct consequence of the first order nature of the PM-FM transition.

[1] In the case of the use of a magnetic field as a tuning parameter, the field direction must be perpendicular to the magnetization axis.

[2] During the time of this study, the critical pressure has been found around 4.8 GPa [Sidorov11].

[3] The paper [Hertz76] is not easy to read and this statement is extracted from [Belitz07].

The point where the transition changes from second order to first order is called a tricritical point (TCP). One consequence of the change of order at the TCP is that, at low temperature, the first order PM-FM transition is field induced above p_{TCP} if the magnetic field is applied along the easy magnetization axis. This can be easily understood with the help of fig. 4.1. This would not be observed for a second order phase transition since the applied magnetic field itself breaks the time reversal symmetry that normally reveals the second order transition (see fig. 4.1). Thus it is clear that the metamagnetism observed above p_{TCP} arises from the first order nature of the PM-FM transition.

At higher temperature, the field induced first order PM-FM transition terminates at a critical end point (CEP) above which a crossover regime is observed. The temperature evolution of the CEP with pressure and magnetic field can be predicted from the different theories of a first order PM-FM transition. These theories predict the existence of a quantum critical end point (QCEP) where the CEP will occur at $T = 0$ K. A QCEP differs from a QCP by the absence of spontaneous symmetry breaking [Grigera01]. The typical phase diagram is symmetric with respect to $H = 0$, and the two surfaces of first order transition are called "wings" [Griffiths73].

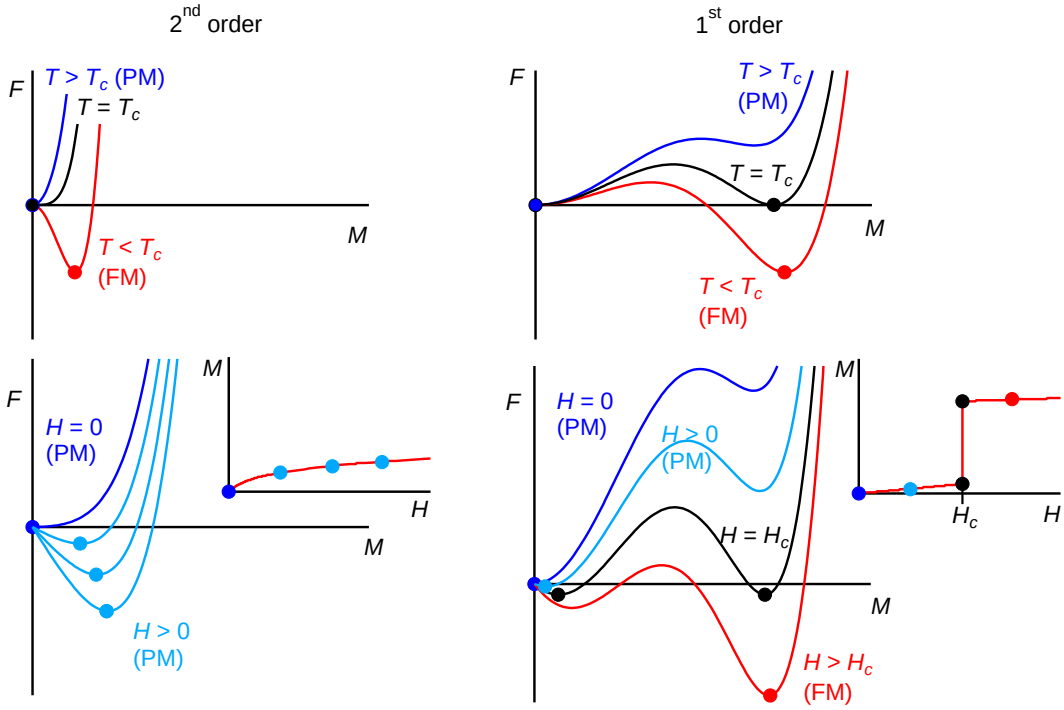

Figure 4.1: Free energy F as a function of the order parameter M in different situations of temperature T and conjugate of the order parameter H (magnetic field applied parallel to M). The dots indicates the stable state : paramagnetic (PM) or ferromagnetic (FM). In the 1^{st} order case at the critical temperature T_c, two stable states coexists. In the PM phase close to a 2^{nd} order transition, H does not induce any transition. However, in the PM phase close to a 1^{st} order transition, H induce a transition.

4.1.2 Motivations

Therefore, the experimental determination of the evolution of the CEP with pressure and magnetic field is necessary to test the different theories of first order PM-FM transitions. In addition, it allows the determination of the coordinates of the QCEP. Since it requires

precise experimental tuning of the temperature, the pressure and the magnetic field at the same time, it has been rarely performed and also constitute an experimental challenge.

4.1.3 Two Ways to Determine the Wing Structure Phase Diagram

The main result of this section is drawn in fig. 4.2. The *T*-*p*-*H* phase diagram presents the first determination of the line of critical points from the TCP to the proximity of the QCEP.

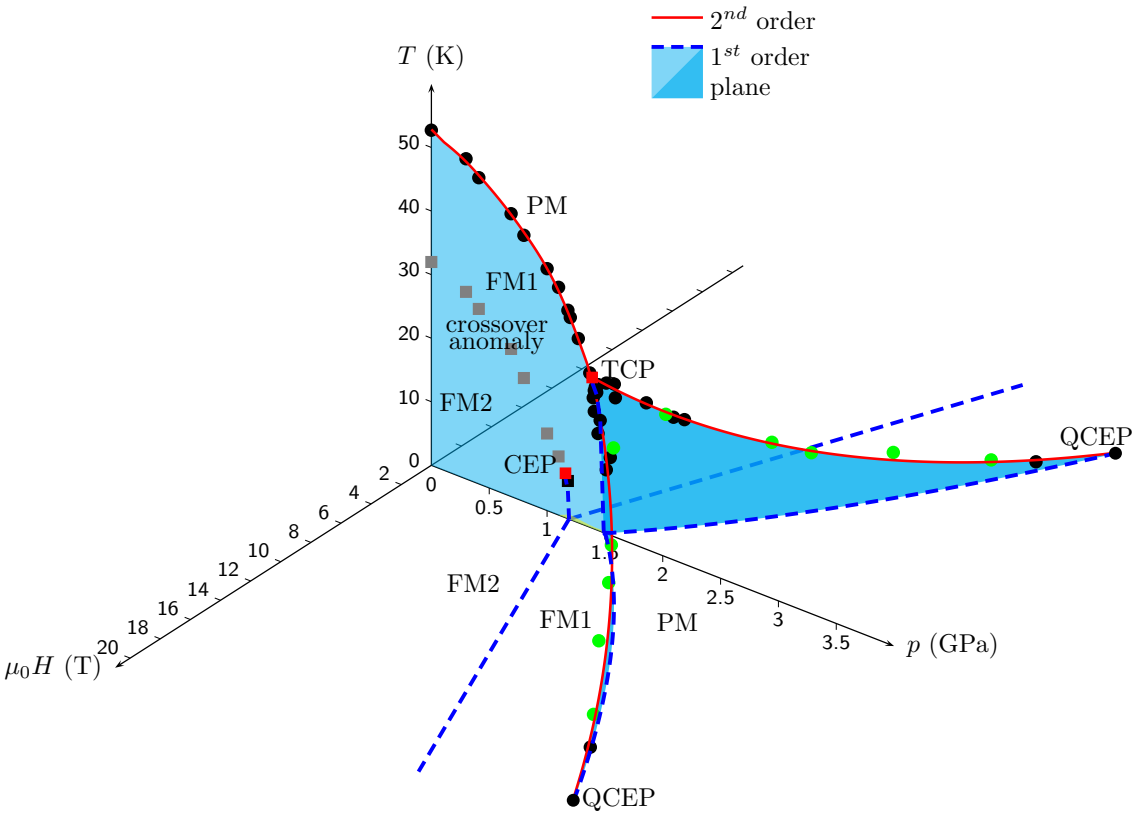

Figure 4.2: Temperature-pressure-magnetic field phase diagram of UGe_2 drawn from resistivity (black and gray dots) and Hall resistivity (green dots) measurements. The quantum critical end point (QCEP) has not been reached experimentally and its position is estimated by extrapolation.

Such determination can be done by two techniques : a determination by field sweep at constant temperature or by temperature sweep at constant magnetic field. The point is to distinguish between three type of anomalies :

- a transition when crossing the surface of first order transition (in blue in fig. 4.2)
- a transition when crossing at the CEP, the boundary of second order transition (in red in fig. 4.2)
- a crossover when crossing over the CEP

In the field sweep, the difference between these anomalies is not marked, especially in resistivity measurements. It is slightly easier with Hall resistivity data and this is presented in section 4.1.5. Using temperature sweeps, the difference is revealed by a

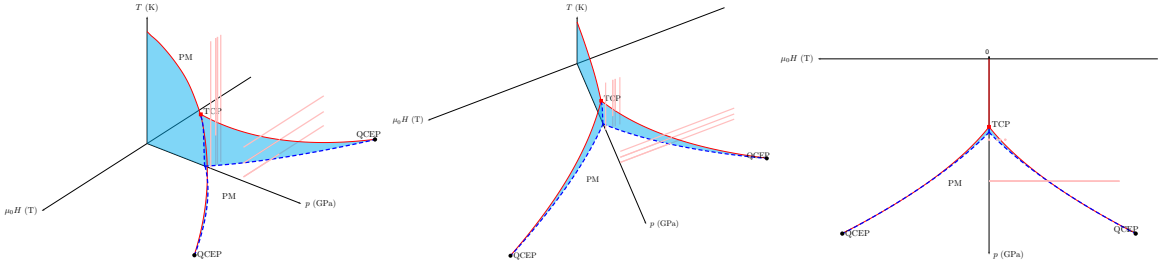

Figure 4.3: Different views of the same phase diagram for a complete visualization. Pink lines represent several experimental paths, temperature sweeps or field sweeps, to determine the position of the wing boundary (red line).

change in the anomaly at the transition. This is the reason why it was discovered first using temperature sweeps and is presented in the following section 4.1.4.

4.1.4 Results of the Resistivity Measurements by Temperature Sweep

Determination of the TCP by Resistivity

The temperature dependence of electrical resistivity at zero field is presented in Fig. 4.4(a). The different cases are clearly observed : -at 0.30 GPa we detect only the Curie temperature T_C; -at 1.18 GPa, the transitions PM-FM1 at T_C and FM1-FM2 at T_x; -at 1.27 and 1.46 GPa, only the PM-FM1 transition; -above $p_c \approx 1.49$ GPa, only the PM regime. The phenomena are more obvious taking into account the temperature derivative of the resistivity $d\rho/dT$ (Fig. 4.4(b)). The most striking point is the change of the anomaly at T_C going from a sharp positive maximum of $d\rho/dT$ at low pressure to a small negative minimum close to p_c.

The sharp positive maximum of $d\rho/dT$ indicates that the resistivity is abruptly suppressed below T_C. This is usually observed in ferromagnetic metals where the resistivity due to the spin disorder scattering is scaled by the bulk magnetization as $1 - [M(T)/M(0)]^2$ [Fisher68b]. Conversely, the negative peak of $d\rho/dT$ at T_C is indicative of a hump of resistivity. The anomaly in the temperature dependence of $d\rho/dT$ changes drastically and indicates the switch at the TCP from a second order to a first order transition.

Evolution of the TCP with Pressure and Magnetic Field

We will now focus on the field dependence of the resistivity anomaly. Three different cases are presented in Fig. 4.5 : $p < p_{TCP}$, $p_{TCP} < p < p_c$ and $p_c < p$.

In Fig. 4.5(a), $p < p_{TCP}$, the second order PM-FM1 transition is observed as a positive peak in $d\rho/dT$. An applied magnetic field smears the anomaly out, since the applied magnetic field itself breaks the time reversal symmetry, and the peak of $d\rho/dT$ at T_C is quickly broadened. T_C is determined by the maximum of $d\rho/dT$ and it slightly increases under magnetic field (Fig. 4.5(d)), as usual for conventional metallic ferromagnets.

In contrast, Fig. 4.5(b) shows $p_{TCP} < p < p_c$. At zero field the minimum in $d\rho/dT$ indicates the first order transition. But increasing H to $H_{CP} \approx 0.3$ T leads to the recovery of the second order like anomaly which broadens at higher fields.

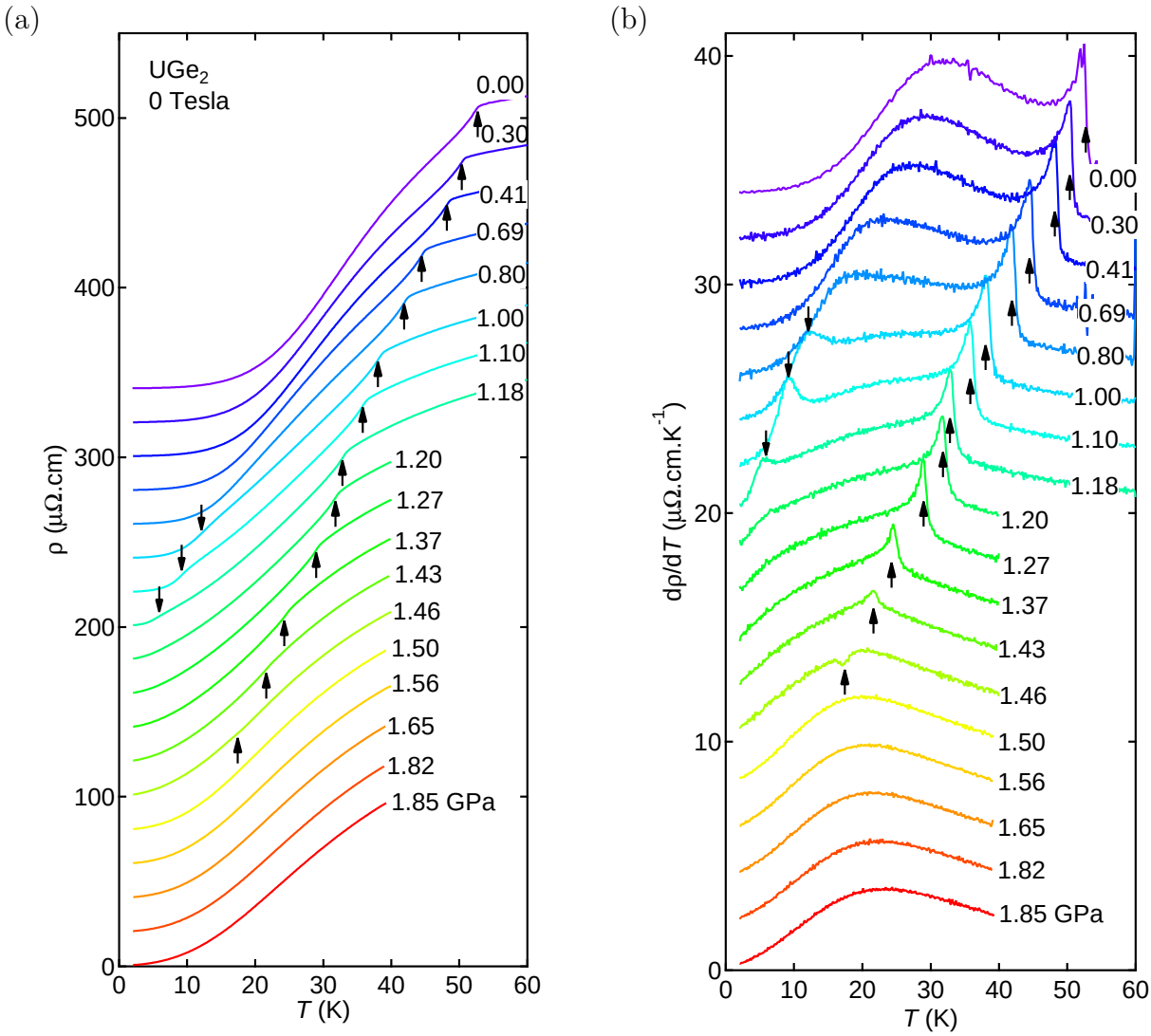

Figure 4.4: Temperature dependence of the electrical resistivity (a) and its temperature derivative (b) at different pressures. Down and up Arrows indicate T_x and T_C respectively. The data are offset for clarity.

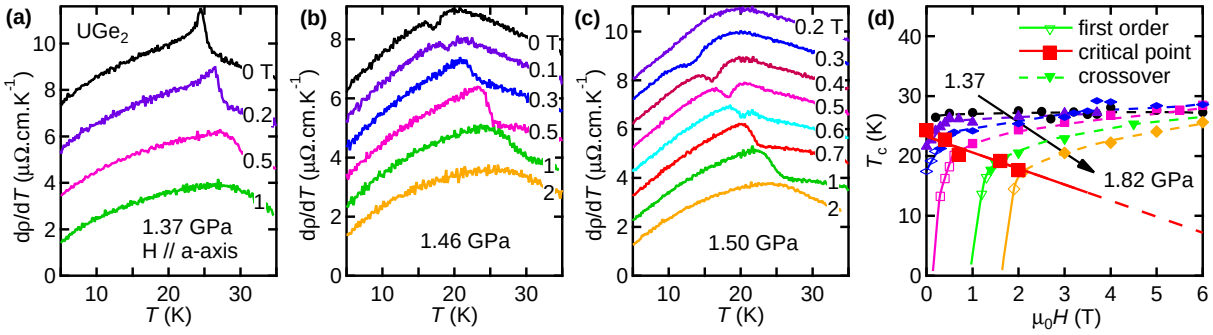

Figure 4.5: Temperature derivative of resistivity $d\rho/dT$ for three typical pressures : (a) : $p < p_{\mathrm{TCP}}$; (b) : $p_{\mathrm{TCP}} < p < p_c$ and (c) : $p > p_c$. The data are offset for clarity. See text for discussion. (d) : Magnetic field dependence of T_C at different pressures (1.37, 1.43, 1.46, 1.50, 1.65 and 1.82 GPa). T_C is defined at the optimum of the positive or negative anomaly. The line of critical point $H_{\mathrm{CP}}(T,p)$ separates the different regimes. The PM-FM1 transition will occur only below H_{CP} : full lines, open symbols, negative anomalies. For $H > H_{\mathrm{CP}}$ (crossover) : dashed lines, full symbols, positive anomalies. The $H_{\mathrm{CP}}(T,p)$ line can be extrapolated to 0 K at the QCEP.

Above $p_c \approx 1.49$ GPa, no anomaly is detected for $H < H_c = 0.2$ T at 1.50 GPa (paramagnetic state) : see Fig. 4.5(c). With applied magnetic field above H_c, a minimum appears (first order PM-FM1 transition), but above $H_{CP} \approx 0.7$ T, this negative anomaly suddenly becomes positive, indicating the change from a first to a second order transition.

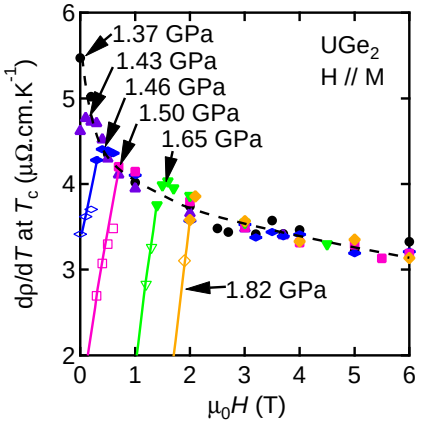

Figure 4.6: Magnetic field dependence of $d\rho/dT$ at the Curie temperature T_C. Full symbols indicate the evolution when the anomalies are positive. For $H > H_{CP}$, $d\rho/dT$ decreases smoothly with magnetic field, as a crossover of the PM-FM1 transition. Open symbols draw the evolution when the anomalies are negative. Lines are guide for the eyes. Lines are continuous in the case of the first order transition and dashed in the case of the crossover.

We conclude that there are two different anomalies with different behavior under magnetic field. The positive peak is broadened and disappears under magnetic field. The associated T_C increases slowly under magnetic field. In contrast, the minimum is more visible and the associated T_C increases rapidly. As we have already mentioned, a PM-FM second order transition is changed to a crossover under magnetic field parallel to the magnetization. But as soon as the PM-FM transition is of first order, the magnetic field parallel to magnetization does not supress the first order transition. These behaviors are presented for different pressures in Fig. 4.5(d) and 4.6, where full lines draw the evolution of the negative anomalies (minimum) and dashed lines follow the positive ones (peak). The boundary between the negative anomaly (open symbols) and the positive peak (full symbols) allows us to draw the second order transition line which limits the first order surfaces. Thus, the "wings" are experimentally plotted (see Fig. 4.2), in good agreement with the schematic phase diagram [Uhlarz04, Kimura04, Pfleiderer01, Belitz05, Yamada07, Rowley10] for weak itinerant ferromagnets.

In ref. [Taufour10], we estimated the position of the QCEP "around $10 - 15$ T and $3 - 4$ GPa" from a linear extrapolation of the data up to 1.85 GPa. We also mentioned that "higher pressure measurements are required for more accurate determination." As it will be presented in the following, the QCEP seems indeed to be located at higher magnetic field than 16 T, the maximum available in this study. Measurements in very high field facilities are required.

4.1.5 Results of the Hall Effect Measurements by Field Sweep

By looking at fig. 4.3, it is clear that the determination of the wing boundaries by temperature sweeps is more and more difficult as the pressure increase. This is due to the fact that the plane of first order transition is more and more vertical (parallel to

the temperature axis), so that the observation of a negative anomaly in $d\rho/dT$ becomes impossible.

To continue the work at higher pressure, two different experiments have been set up in parallel. One experiment was to measure the Hall resistivity and the other to continue the same measurement as in section 4.1.4, i.e. the electrical resistivity with $J//H//a$-axis, by field sweep in another pressure cell.

The later experiment is more difficult and less efficient :

- in field sweeps, the change in resistivity from a first order transition to a crossover is not marked
- to obtain $J//H$, the pressure cell has to be rotated 90 ° so that it does not fit in a PPMS cryostat
- in consequence, the measurements have to be performed in a larger magnet such as the one used with dilution refrigerator, but a regulation up to 30 K is necessary

For these reasons, only one pressure measurement was performed in collaboration with Georg Knebel in his cryostat with a 13 T magnet. At the same time, the Hall resistivity measurements started in collaboration with Dr. Hisashi Kotegawa gave faster results.

The details and full discussion of this experiment are given in [Kotegawa11]. Here, the determination of the "wing" phase diagram is described in a few steps and illustrated at one pressure in fig. 4.7 :

- The PM-FM anomaly in Hall resistivity ρ_{xy} measured with field sweeps is revealed by a step like jump (fig. 4.7(a)).
- It shows a peak in the derivative $d\rho_{xy}/dH$ used to define H_c (fig. 4.7(b)).
- To characterize this anomaly, it is convenient to determine the width of this peak. It can be estimated using the crossing point of linear guidelines (fig. 4.7(b)).
- The main observation is that the transition width is temperature independent for $T < T_C$ and increases continuously for $T > T_C$ (fig. 4.7(d)). The behavior at low temperature is associated to the first order transition, and the behavior at high temperature corresponds to the associated crossover. Thus, the separation at T_C between the two regimes is the critical end point (CEP) of the first order transition.
- Following the CEP at different pressures draws the "wing" phase diagram (fig. 4.8 and 4.9).

It is possible to check the consistency between the present determination of T_C and the previous report from $d\rho/dT$ (section 4.1.4). For example, $d\rho/dT$ indicates T_C of 18 K at 1.82 GPa, while the present estimation using $d\rho_{xy}/dH$ indicates T_C of 18 K at 1.80 GPa.

These results present the first determination of the wing structure phase diagram from the TCP to the close proximity of the QCEP. As will be presented in section 4.1.7, it is possible to compare this experimental result to some of the theories. T_{CEP} on the second-order line is suggested to become zero at $p_{QCEP} \sim 3.5 - 3.6$ GPa and $H_{QCEP} \sim 17 - 19$ T from extrapolations presented in section 4.1.7. Because of the large pressure and field extensions of the first-order plane, UGe_2 will be a good test for theories of the FM phase diagram.

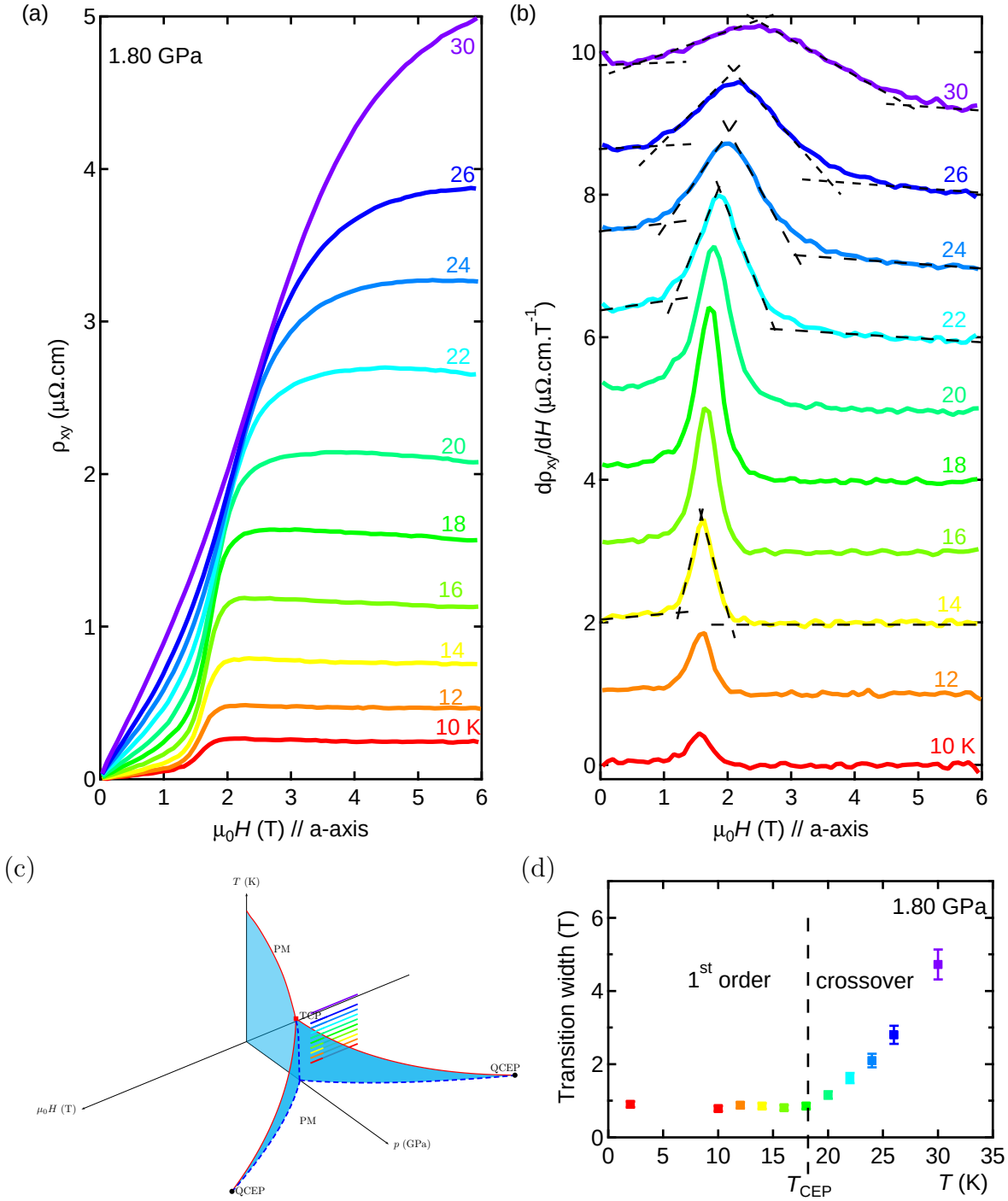

Figure 4.7: Magnetic field dependence of the Hall resistivity ρ_{xy} at 1.80 GPa (a) and of its derivative $d\rho_{xy}/dH$ (b). The experimental path are shown by lines on the phase diagram in (c). The width of the transition determined by the cross point of linear guidelines as illustrated in (b) is plotted as a function of temperature in (d). All these data are similar to those published in ref. [Kotegawa11] for which other pressures have been selected.

4.1.6 Critical Behavior on Approaching the QCEP

Primarily Results from Hall Resistivity Measurements

In the Hall effect experiments, the electrical resistivity ρ_{xx} can be obtained by averaging the measurements at positive and negative field. Then, assuming a Fermi liquid behavior

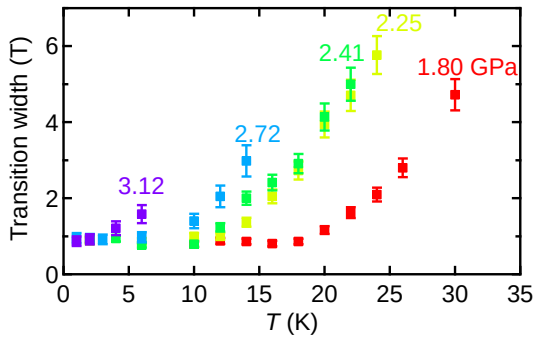

Figure 4.8: Temperature dependence of the transition width determined as described in fig. 4.7 for different pressure [Kotegawa11].

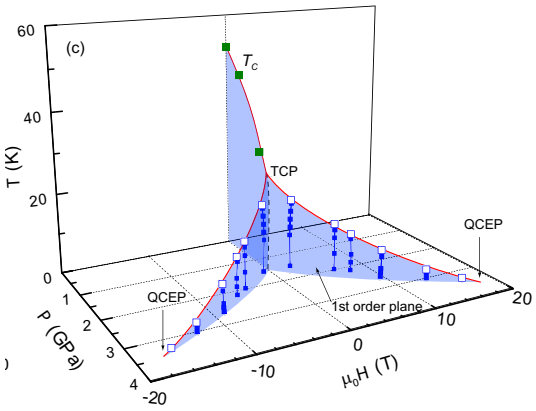

Figure 4.9: Three dimensional phase diagram of UGe_2 determined by Hall resistivity measurements [Kotegawa11].

$\rho_{xx} = \rho_0 + AT^2$ between curves at 1 K and 2 K, H. Kotegawa obtained the field dependence of the A coefficient. It reveals a characteristic change when approaching the QCEP :

- At low pressure, far from the QCEP, the A coefficient shows a step jump at the PM-FM transition, characteristic of a first order behavior.
- At 3.12 GPa, the A coefficient shows a peak at the PM-FM transition, characteristic of the proximity to a second order transition. It is indeed expected that A diverges at a quantum critical point (QCP). However, a QCEP might induce different behavior.

A direct measurement of the electrical resistivity at low temperature is necessary to confirm this observation because in the Hall experiment, the measurement of ρ_{xx} arises from the misalignment of the Hall contacts. Moreover, when measuring the "wing" boundary, measurements in the K range are necessary, so that a good regulation in the mK range at the same time is not possible (it requires to increase the thermal coupling with the mixing chamber).

Results from Resistivity Measurements at Low Temperature in a Diamond Anvil Cell

To investigate the A coefficient of the T^2 of the resistivity, a resistivity measurement in a diamond anvil cell has been set up. The use of a diamond anvil cell is necessary to reach higher pressures and to fit in a high field facility laboratory such as the LNCMI in Grenoble. However, in this section, only results below the available field of 16 T are presented.

The results of the measurements are shown in fig. 4.10. The experimental paths consist of field sweeps at constant temperature such as for the Hall resistivity measurement illustrated in fig. 4.7(c) but only at low temperature : apart for 3.3 GPa, the wing boundary is not reached.

The observation of superconductivity at 1.67 GPa (see fig. 4.10 at 1.67 GPa, curve at 0.1 K) is not expected since no superconductivity has been reported above the critical pressure p_c, i.e. in the paramagnetic phase. This is certainly due to pressure inhomogeneities. However, the pressure gradient with the use of argon as a pressure transmitting medium is usually smaller than 0.1 GPa (see for example [Hardy04, Tateiwa09]). Therefore, this feature deserves a careful checking and a new experiment is scheduled in the

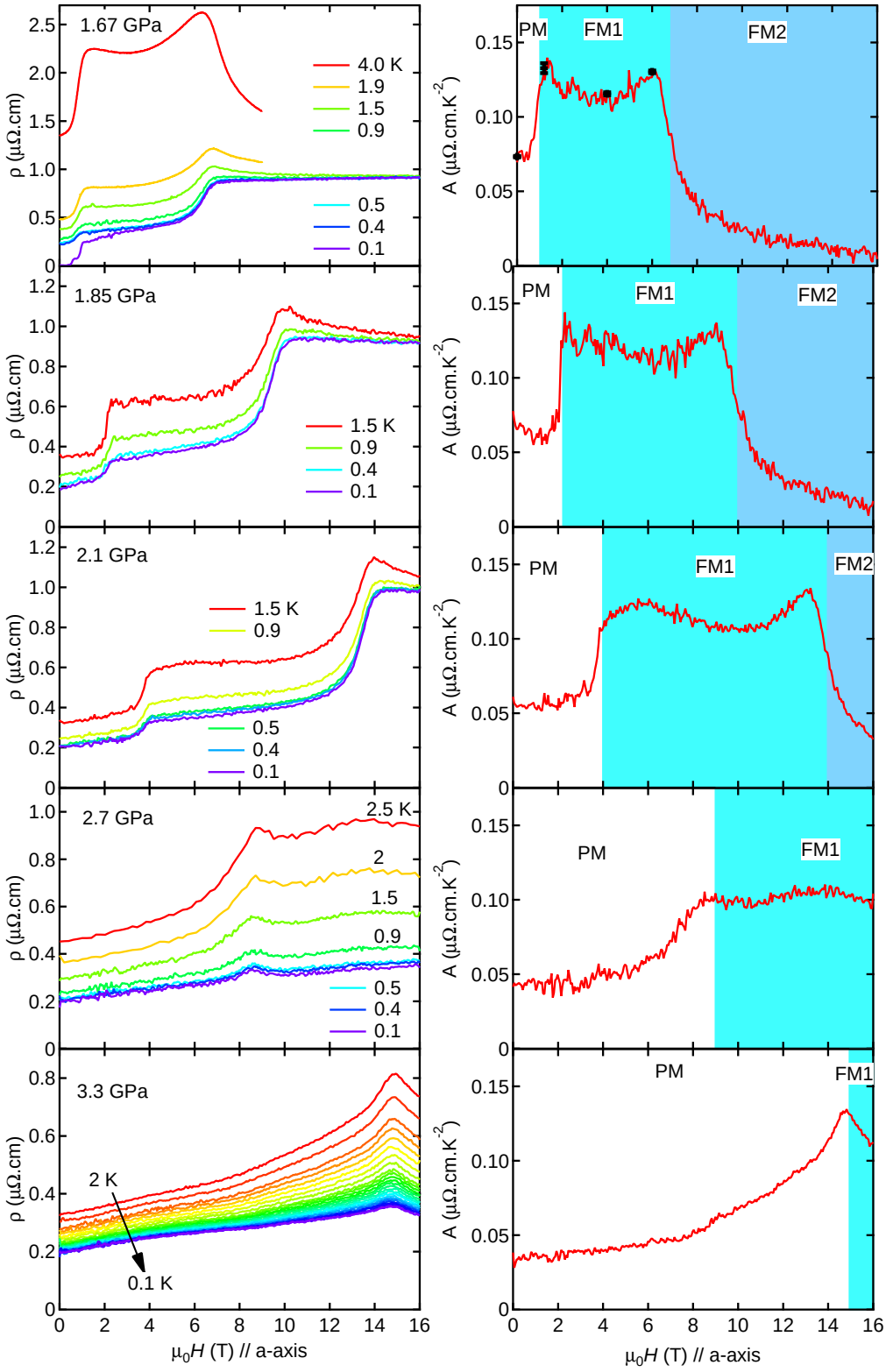

Figure 4.10: Magnetic field dependence of the resistivity at different temperature at different pressures. 2 successives anomalies of the resistivity are observed corresponding to the successives paramagnetic PM, FM1 and FM2 phases. The A coefficient is obtained from fitting these curves with a Fermi liquid law $\rho = \rho_0 + AT^2$ by using only few temperatures. A set of $\rho(T)$ data have been measured at 1.67 GPa (see fig. 4.11), and the obtained A coefficients are shown by black dots. At 1.33 GPa, a large number of temperatures has been measured, allowing us to check the validity of the Fermi liquid behavior (see fig. 4.13). The A coefficient is higher in the FM1 phase than in the PM phase also higher than in the FM2 phase.

laboratory in collaboration with Amalia Fernandez and Daniel Braithwaite. This experiment will require a new experimental technique currently in development : the possibility to change pressure at low temperature in a dilution refrigerator. That kind of apparatus already exists in our laboratory in a ^{4}He crystat. Its realization in a dilution refrigerator will allow a precise tuning of the pressure around p_c with a diamond anvil cell. The choice of UGe_2 as a test sample is also reinforced by the fact that $p_c \approx 1.5$ GPa is not too high for a diamond anvil cell, so that the electrical contacts will more likely survive the application of pressure. First, the use of argon as a pressure transmitting media will be used, but the use of helium could also be an important improvement.

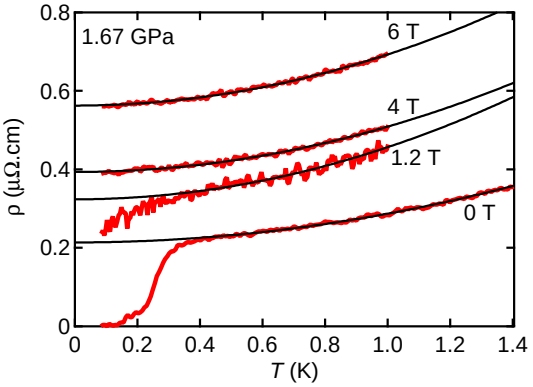

Figure 4.11: Temperature dependence of the resistivity at 1.67(5) GPa. Fits of the data with a Fermi liquid law $\rho = \rho_0 + AT^2$ are also shown. The obtained A coefficients are shown in fig. 4.10, in good agreement with the results inferred using only few temperature points. The validity of the Fermi liquid behavior is also checked at 3.3 GPa (see fig. 4.13).

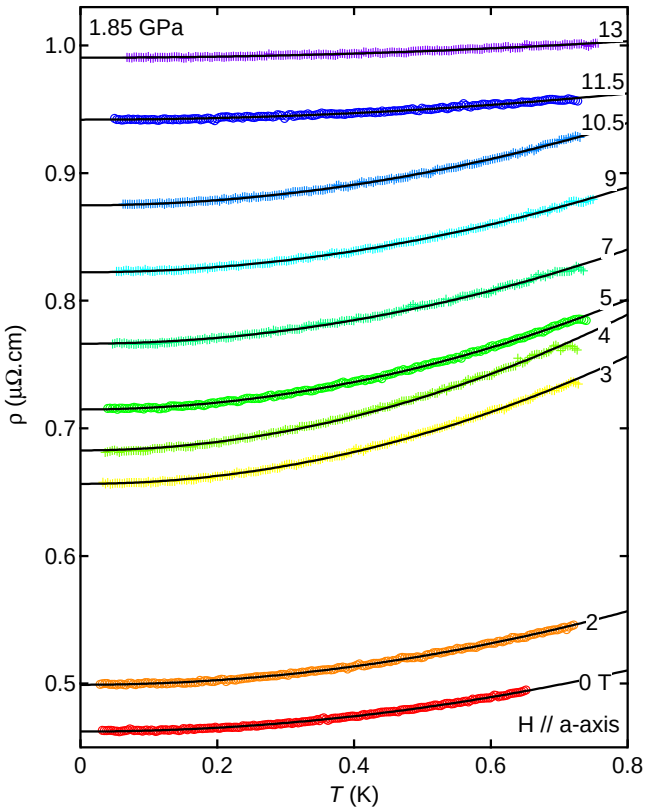

Figure 4.12: Temperature dependence of the resistivity at 1.85(5) GPa. Fits of the data with a Fermi liquid law $\rho = \rho_0 + AT^2$ are also shown.

The temperature dependence of the resistivity is different in the 3 phases : paramagnetic (PM), FM1 and FM2. As directly visible from the $\rho(H)$ curves, it is larger in FM1 than in the PM and FM2 state (see figs. 4.11 and 4.12). For a set of fixed H points (300 points between $0T$ and 16 T), a fit of all measured temperature points is realized assuming a Fermi liquid behavior ($\rho = \rho_0 + AT^2$). A larger A coefficient is obtained in the FM1 phase (see fig. 4.10). The increase of the A coefficient from the PM to FM1 phase is in contrast with the usual decrease observed in other field induced ferromagnets. For example in UCoAl, the γ term of the specific heat decreases at the PM-FM transition [Matsuda00]. As visible in fig. 4.14, the residual resistivity shows a maximum at the PM-FM1 transition. A bigger increase due to critical fluctuations can be expected closer to the QCEP [Miyake02].

The validity of the Fermi liquid behavior can be checked by fitting with $\rho = \rho_0 + AT^n$. As illustrated at 3.3 GPa in fig. 4.13, the exponent n does not deviate significantly from the Fermi liquid value of 2. Thus, Fermi liquid behavior is confirmed.

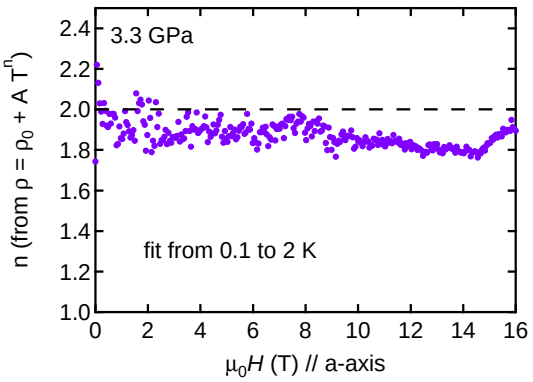

Figure 4.13: Magnetic field dependence of the n exponent obtained by fitting the resistivity ρ with $\rho = \rho_0 + AT^n$.

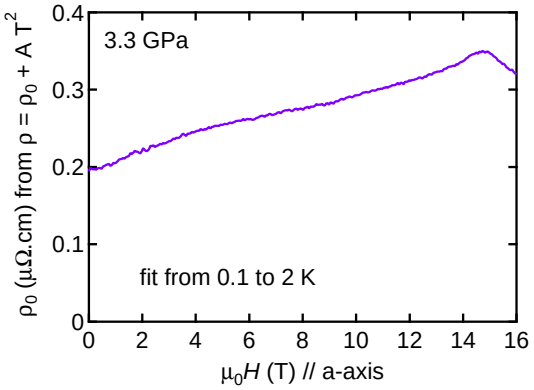

Figure 4.14: Magnetic field dependence of the residual resistivity obtained assuming a Fermi liquid behavior of the resistivity $\rho = \rho_0 + AT^2$.

As was suggested from Hall resistivity measurements, when approaching the QCEP, the step-jump of the A coefficient at the PM-FM transition changes to a peak (see fig. 4.10 and 4.15(a)). The figure 4.15(b) shows the enhancement of the A coefficient at the transition when this transition evolves from first order towards second order at the QCEP. A bigger enhancement can be expected with further increases of pressure. It is also possible that a non-Fermi liquid behavior will be observed at the QCEP.

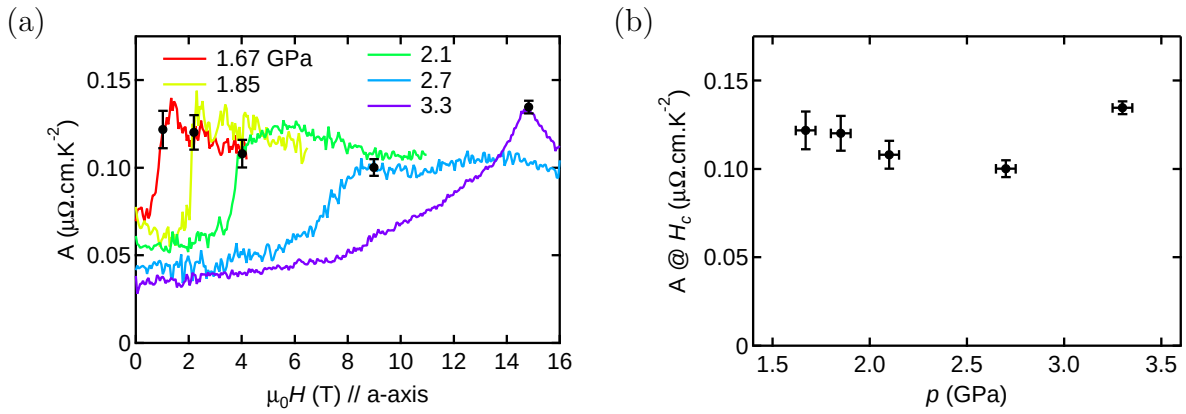

Figure 4.15: (a) Magnetic field dependence of the A coefficient obtained assuming a Fermi liquid behavior of the resistivity $\rho = \rho_0 + AT^2$ at different pressure. The values at the PM-FM transition are marked with a circle. (b) Pressure evolution of the value of the A coefficient at the PM-FM transition. The error are estimated from the noise level which depend on the number of points used for fitting.

First Results up to 29 T

The last experiment realized in this study was to measure the resistivity at low temperature up to 29 T in LNCMI Grenoble. The pressure was measured to be 3.7 GPa. Using a top loading refrigerator in collaboration with Ilya Sheikin and Liam Malone, it was possible to cool the diamond anvil cell down to 26 mK at 0 T, and 50 mK up to 29 T. The measurement consists of field sweep at constant temperature similar to the one presented in the previous section 4.1.6. The results are presented in fig. 4.16. The A coefficient shows a maximum at the PM-FM1 transition. However, the value of this maximum is slightly lower than the value at 3.3 GPa. It can be understood if we assume that 3.7 GPa

is above the quantum critical end point. In this case, we expect a broadening of the anomaly as a crossover from PM to FM1.

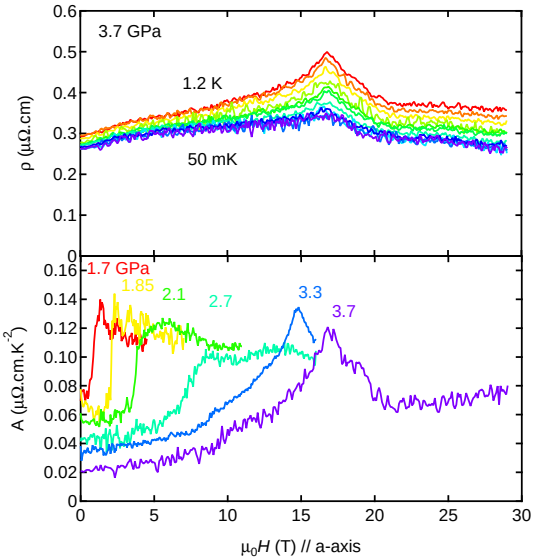

Figure 4.16: Magnetic field dependence of the resistivity at 3.7 GPa (top panel) and of the A coefficient at different pressures (bottom panel). The A coefficient is obtained by taking few temperature points from the $\rho(H)$ data and fitting assuming a Fermi liquid behavior ($\rho = \rho_0 + AT^2$). The maximum value of the A coefficient is higher at 3.3 GPa and reduced at 3.7 GPa.

Here, we can see that such measurement under high pressure, high field and low temperature is possible. A careful checking of the validity of the Fermi liquid behavior remains to be done, as well as measurements at several pressures to follow the evolution of the anomaly in the crossover regime. If it is really a crossover, the maximum in the A coefficient should disappear. Measurements around 4, 4.5 GPa are necessary.

4.1.7 Theories

It has already been shown in fig. 4.1 that if the PM-FM transition is first order, then a PM-FM transition can be induced with a magnetic field applied along the magnetization axis. Thus, the observation of the wings is a direct consequence of the fact that the transition is first order above the TCP pressure p_{TCP}.

The theories of first order PM-FM transition include magneto-elastic coupling, effects of excitations at the Fermi surface, particular shape of the density of states and singularities of the Fermi surface.

Influence of the Magneto-Elastic Coupling

Since the pressure indeed has an effect on the Curie temperature T_{C}, it necessarily means that the magnetic energy is coupled to the lattice.

A PM-FM transition can be of first order because of magneto-elastic coupling. It was shown that in a two-dimentional Ising lattice, the transition will become of first order if the exchange interaction is a function of lattice spacing and that the lattice is deformable [Rice54, Domb56, Bean62, Mattis63, Garland66][4]. However, the assumption that the heat capacity at constant volume C_v becomes infinite is not generally true, and it was shown that it is the heat capacity at constant pressure C_p that becomes infinite [Fisher68a], and the transition remains of second order.

[4]In [Mattis63], sometimes referred to as the magnetothermomechanical theory (MTM), all bond lenghts are assumed to be the same, which correspond to a compressible crystal with infinite rigidity. In [Larkin69], the more realistic case of finite compressibility and finite rigidity is considered.

Taking into account the compressibility and interaction with acoustic phonons, it is shown in [Larkin69] that the transition will be of first order if :

$$\frac{1}{T_C}\frac{4\mu K_0}{3K_0+4\mu}\left(\frac{\partial T_C}{\partial p}\right)^2 \Delta C_p > 1 \tag{4.1}$$

where K_0 and μ are the non singular part of the bulk and shear moduli, and ΔC_p is the anomalous part of the heat capacity of unit volume. The left hand side in this expression is quite small and the transition of the first order occurs at temperature $T^{1^{st}}$ close to the critical temperature T_C where fluctuations contributing to the specific heat are large enough. It means that the temperature difference $T^{1^{st}} - T_C$ is smaller than the critical temperature T_C by many orders. Thus, experimentally, the transition is revealed as a second order transition. However, when T_C is reduced by a tuning parameter like pressure p, the term $\frac{1}{T_C}\left(\frac{\partial T_C}{\partial p}\right)^2$ can become very large and the condition 4.1 satisfied in a wider temperature range so that it is experimentally possible to detect a first order transition.

Main results of [Larkin69] with isotropic elastic properties were later confirmed using renormalization group technique [Wegner74, Sak74] and extented to more general elastic properties [Khmelnitskii75, Bergman76, De Moura76, Murata77].

Recently, it has been demonstrated that the relation 4.1 is not fulfilled for UGe_2 at low pressures [Mineev11b], in agreement with the fact that the transition remains of the second order. It points out that the criterium 4.1 can certainly be fulfilled at higher pressure when $T_C \approx 10$ K.

Also, the simple Landau theory, without including fluctuations, predicts that a first-order transition will occur before a quantum critical point that is accessed by the application of pressure [Gehring08].

Influence of Excitations at the Fermi Surface

The basic premise of the Landau theory of phase transition is that the thermodynamic potential F can be expanded (in series) as a function of the order parameter M, i.e. that F is an analytic function at $M = 0$. However and despite the great success of this theory, it is not generally true and non analytic corrections can be added to the series.

For example, spin fluctuations in a Fermi liquid can induce non analytic terms in the Landau free energy. However, these non analytic term can arise from different contributions and cancellations occur [Carneiro77], explaining why their existence remains a subject of controversy [Chitov01]. It appears that non analytic corrections to the Fermi liquid are universal [Misawa71, Belitz97, Chubukov04, Rech06, Maslov09]. This area of research extends well above the simple question of whether a PM-FM transition becomes first order or not. It deals indeed with theories of non Fermi liquid behavior. It also suggests a breakdown of the theory of itinerant quantum criticality [Hertz76, Millis93, Moriya95] and could participate in explaining why unusual behaviors seems to systematically "hide" the quantum critical point (QCP) [Laughlin01].

This theory shows that the effects of gapless particle-hole excitations at the Fermi surface induce a nonanalytic term in the Landau expansion of the free energy F as a function of the magnetic moment M [Belitz99]. It suggests that FM transitions in clean three-dimensional itinerant ferromagnets are always of first order at low enough temperature. The nonanalytic term comes from long-wavelength correlation effects and successfully explains the first order transition at low T while the higher temperature transition is of

second order. If the long range correlation effects are important, i.e., when the transition is first order, one may expect that these effects dominate the critical behavior measured by resistivity. With an itinerant model of the magnetic moment, long-range correlation effects can explain a negative anomaly for $d\rho/dT$ [Su75], which is what has been observed (see section 4.1.4). Then, at higher temperature, long-range effects do not dominate and the transition is of second order as for usual ferromagnets.

This theory has been developed in a way that allows comparison with our results. Equations of the phase diagram whose schematic form is visible on fig. 4.17 are given in ref. [Belitz05].

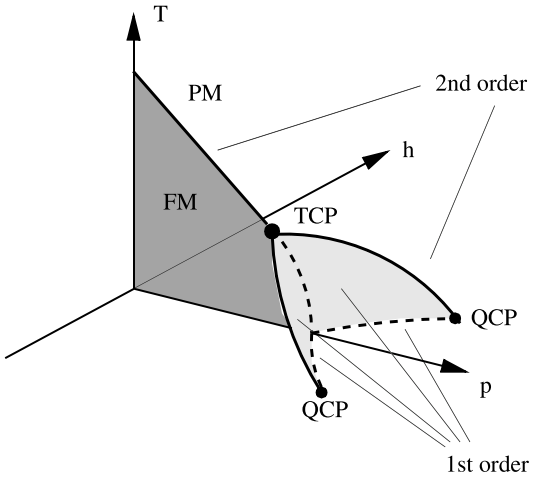

Figure 4.17: Schematic phase diagram in the temperature - pressure - magnetic field (T-p-H) space. Shown are the ferromagnetic (FM, dark shaded) and paramagnetic (PM) phases at $h = 0$, the tricritical point (TCP), and the two quantum critical points (QCP). Also shown are various lines of first-order (dashed lines) and second-order (solid lines) phase transitions, and the "wing" surfaces of first-order transitions (light shaded) [Belitz05]. The QCP are referred to as QCEP in the text. A QCEP differs from a QCP by the absence of spontaneous symmetry breaking [Grigera01].

Influence of Spin Fluctuations

Similarly to the theory of QCP [Hertz76, Millis93, Moriya95], the behavior at a QCEP has been investigated [Yamada93, Yamada99, Meyer01, Satoh01, Millis02]. The magnetoelastic coupling has been included [Yamada07].

The evolution of the critical end point temperature T_{CEP} with the tuning parameter δ (function of the pressure p) is given as $T_{CEP} \propto \delta^{z/(z+d-2)}$ [Millis02] where z is the dynamical exponent and d is the space dimension. As visible in fig. 4.19, for $d = 2$, T_{CEP} is found to decrease linearly with δ in the proximity of the QCEP (corresponding to $\delta = 0$). For $d > 2$, T_{CEP} has a downward curvature. The flattened decreasing in $d = 2$ is closer to our observation, at least up to 3.3 GPa (see fig. 4.20). The difficulty in comparing this prediction to our results is that δ might be a complicated function of the pressure p. The critical behavior at $\delta = 0$, i.e. at the pressure p_{QCEP} has been calculated (see table 4.18). The A coefficient of the T^2 dependence of the resistivity is expected to diverge at H_{QCEP}. This is consistent with our observation that this value increases when approaching the QCEP (see fig. 4.15).

	space dimension	
	d=3	d=2
$\gamma = \frac{C}{T}$	$\ln h^{-1}$	$h^{-\frac{1}{3}}$
A ($\rho = \rho_0 + AT^2$)	$h^{-\frac{1}{3}}$	$h^{-\frac{2}{3}}$

Figure 4.18: Critical behavior at the quantum critical end point predicted from renormalization group treatment [Millis02]. $h = \frac{H - H_{QCEP}}{H_{QCEP}}$ where H_{QCEP} is the critical field.

As visble in fig. 4.20, the Belitz theory for three dimensional systems does not provide a good fit in one curve for the data from the TCP to the proximity of the QCEP. The same observation can be done for Millis theory in space dimension $d = 2$ or $d = 3$. However,

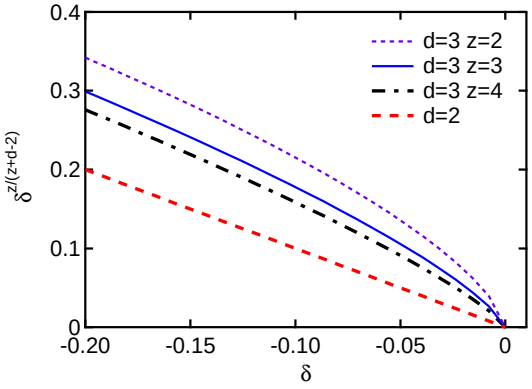

Figure 4.19: Theoretical prediction of the evolution of $T_{CEP} \propto \delta^{z/(z+d-2)}$ where δ is the tuning parameter, z is the dynamical exponent and d is the space dimension [Millis02]. A tentative fit to our data is shown in fig. 4.20(a).

these theories remain valid for data below ~ 10 K. The extension of Belitz calculation to dimension 2 would allow a better comparison.

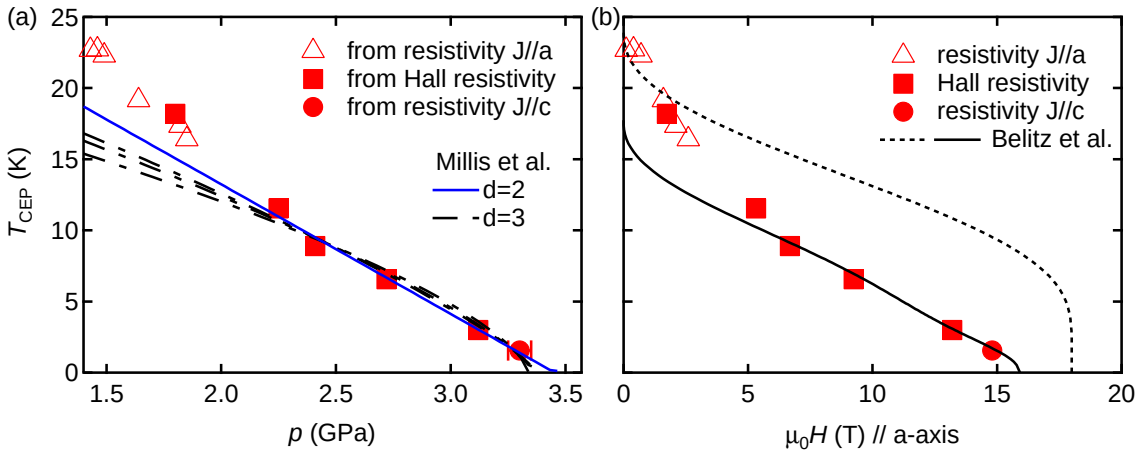

Figure 4.20: Magnetic field (a) and pressure (b) dependence of the critical end point temperature T_{CEP}. The fit with Millis calculations [Millis02] are obtained at different space dimension d. Different values of the dynamical exponent $z = 2 - 3 - 4$ are plotted for $d = 3$, showing that the agreement is more sensitive to the d value. The tuning parameter δ has been taken as $\delta = (p - p_{QCEP})/p_{QCEP}$. Two fits with Belitz calculation [Belitz05] are also presented.

Influence of Singularities of the Fermi Surface

It was pointed out that a first order transition can occur if the Fermi level is between two peaks in the density of states [Shimizu64]. This particular structure of the density of states can also provide an explanation for the FM1-FM2 transition (see section 3.7)[Sandeman03]. The zero temperature phase diagram obtained from this model is in qualitative agreement with the experiment (see fig. 4.21). Calculations at finite temperature will be useful to test this scenario.

More recently, changes in the topology of the Fermi surface from Lifshitz transitions have been considered. Lifshitz transitions correspond to the collapse of a neck of the Fermi surface or the emergence / disappearance of a Fermi pocket. In the absence of the electron interaction, a Lifshitz transition is continuous. However, it has been shown that in the presence of interactions in a preexisting symmetry-broken order, a first order transition may appear [Yamaji06]. Instead of the expected QCEP, a maginal quantum critical point (MQCP) will exist, from which a quantum critical line (QCL) will emerge, replacing the

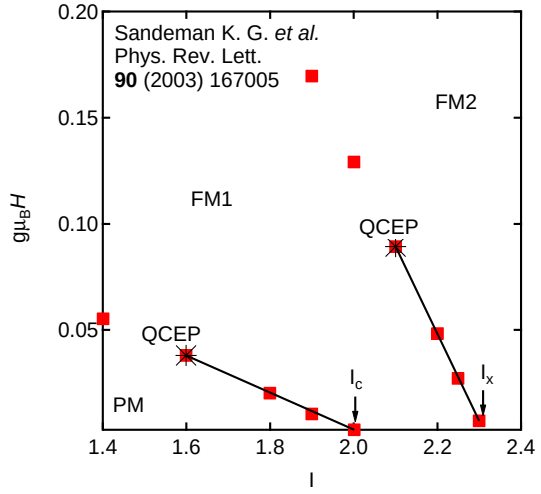

Figure 4.21: Predicted H, I phase diagram where I is the exchange parameter. The tight-binding parameters of the model are the same as in fig. 3.13 page 55 and the total number of spins is $N = 0.8$. It shows the metamagnetic transitions corresponding to the paramagnetic (PM) to low moment ferromagnetic (FM1) phase and then to the higher moment ferromagnetic (FM2) phase. The lines of first order transition are predicted to terminate at a quantum critical end point (QCEP). I_x and I_c correspond to the critical pressures p_x and p_c respectively.

expected crossover above the QCEP (see fig. 4.22) [Yamaji07]. At the crossing of the QCL, a continuous Lifshitz transition occurs. However, the difference compared with a crossover behavior might be small since at low $T \neq 0$, the QCL becomes a crossover.

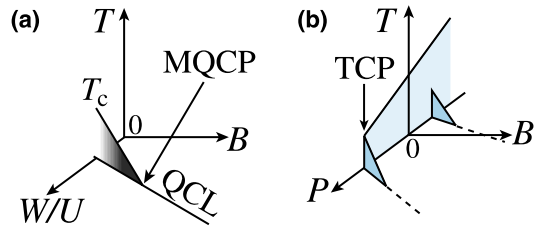

Figure 4.22: (a) Schematic phase diagram around the marginal quantum critical point (MQCP), where a quantum critical line (QCL) and a finite-temperature critical line at T_c meet. Here, B controls quantum fluctuations and corresponds to, for instance, magnetic fields. Experimentally, pressure P may control the ratio of itinerancy (bandwidth) W to the interaction U. (b) Schematic phase diagram proposed for $ZrZn_2$ [Kimura04]. TCP represents the tricritical point, where the critical line at $B = 0$ terminates and the transition becomes of the first order at $B = 0$ below the tricritical temperature. This first-order line below TCP is the edge of the metamagnetic "wing". The dashed lines were regarded as a crossover based on the picture of the QCEP [Yamaji07].

The discontinuous change of the Fermi surface across H_c revealed by quantum oscillatory studies [Terashima01, Settai02] support this idea of a Lifshitz transition. Thermopower measurements could test this theory, since a jump of the thermoelectric power is expected at a Lifshitz transition [Vaks81]. However, such measurements in a diamond anvil cell are very difficult and a new compound with easier measurement conditions would be a breakthrough.

4.1.8 Other Systems and Future Studies

In fig. 4.2, the pressure extension of the PM-FM1 wings is very large by comparison to the zero field parameter : $p_{\mathrm{QCEP}} - p_{\mathrm{TCP}} >> p_c - p_{\mathrm{TCP}}$. This is certainly due to the large values of the magnetization and of the magnetization jump at p_c ($M_0 = 0.9\mu_B$ and $\Delta M_0 = 0.9\mu_B$) associated with large spontaneous magnetostriction ($10^{-4}/\mu_B$ in good agreement with the other heavy fermion compounds [Miyake09]). This large pressure range makes UGe_2 a unique case to observe the FM wings. Such a phenomena is certainly difficult to observe in systems like UCoGe where the M_0 jump will be one order of magnitude smaller [Huy07].

The case of UGe_2 is however complicated experimentally by the high pressure, low temperature and high magnetic field necessary to study the QCEP. A continuation of this study will require measurements in a high field laboratory above 18 T. Another case with lower pressure, and lower magnetic field remains to be found[5]. In this context, the case of UCoAl is interesting. At ambient pressure, this compound is already in the paramagnetic state. Substitution of Y instead of U acts like a negative pressure and restores the ferromagnetic state [Andreev07]. The uniaxial pressure also restore the ferromagnetic state [Ishii03]. As for UGe_2 above p_c, a metamagnetic transition from the PM to the FM state is observed in UCoAl when the field is applied along the c-axis which correspond to the easy magnetization axis in this compound. This first order transition shows hysteresis which decreases progressively with increasing temperature and vanishes at $T_{CEP} \approx 11$ K. With increasing pressure, T_{CEP} is tuned to 0 K at a critical pressure p_{QCEP} around 1.5 GPa and $H_{QCEP} \approx 7$ T. This lower value compared with UGe_2 allows measurements above the critical pressure and critical field. The initial measurements of resistivity performed recently in our laboratory reveal a second anomaly.

Note that a new phase is also found in the proximity of the QCEP in $Sr_3Ru_2O_7$ [Grigera01, Borzi07]. Following our results, a similar study using AC susceptibility have been performed in this material [Wu11]. However the existence of a new phase have not been confirmed. Also it is suggested that the magnetic field should be nonhomogeneous for the specific case of this material [Kirkpatrick11]. This opens a fascinating area of research where new phases exist in the proximity of a QCEP.

4.2 The Critical End Point of the FM1-FM2 Transition

4.2.1 Motivations

It has been shown in section 4.1.1 that the wing structure phase diagram is a direct consequence of the first order nature of the PM-FM transition below the TCP. As described in section 3.6, the FM1-FM2 transition is also first order and a wing structure is expected as well.

The PM-FM transition will now be more precisely labelled the PM-FM1 transition associated to the PM-FM1 wings and to the $QCEP_{PM\text{-}FM1}$. In the following, the FM1-FM2 transition, the FM1-FM2 wings and the $QCEP_{FM1\text{-}FM2}$ are considered.

In the case of the PM-FM1 transition, the first order nature terminates and becomes second order above the TCP. By contrast for the FM1-FM2 transition, the first order nature terminates at the CEP and a crossover regime is observed above the CEP. No second order FM1-FM2 transition exists since the two phases have the same symmetry, so far.

Since it is believed that the PM-FM1 wings will help the understanding on the ferromagnetic quantum criticality, the knowledge of the FM1-FM2 wings might help to understand why this transition is of first order. Interest is increased by the fact that the superconducting transition has its maximum T_{sc} at p_x, i.e. at the FM1-FM2 transition. Moreover, since superconductivity is observed at the quantum phase transition, one may expect fascinating phenomena by driving this transition to a QCEP.

[5] In Ni_3Al, the critical pressure is estimated around 8 GPa [Niklowitz05], in $LaFe_4As_{12}$ around 2 GPa [Tatsuoka10].

4.2.2 Results at $H = 0$: First Order Nature of the FM1-FM2 Transition, CEP and Crossover

Figure 4.23 shows the temperature dependence of the relative elongation $\Delta L_b/L_b$ at different pressures. The expansion coefficient α_b corresponding to the temperature derivative is shown in figure 4.24. A sharp anomaly corresponding to the Curie temperature T_C is observed. Such feature in α_b is observed up to 1.24 GPa, and thus confirms that the PM-FM1 transition is second order at least up to 1.24 GPa. It has been shown in section 4.1.4 that the TCP where it becomes first order is at $p_{TCP} \approx 1.42$ GPa.

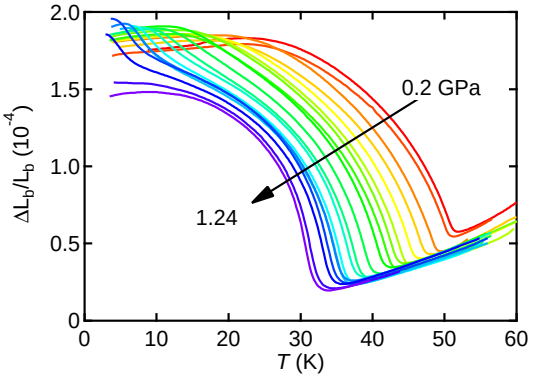

Figure 4.23: Temperature dependence of the relative elongation along the b-axis at all measured pressures. The pressures are 0.2, 0.34, 0.4, 0.56, 0.7, 0.78, 0.86, 0.88, 0.9, 0.98, 1.02, 1.06, 1.12, 1.14, 1.15, 1.17, 1.18, 1.21, 1.24 GPa. The raw data have an offset which has been substracted here. This experimental offset is estimated by fitting the raw data in the paramagnetic regime by a T^2 in addition to the offset [Pfleiderer07]. A selection of these data has been published in the inset of fig.2(a) in ref. [Taufour11].

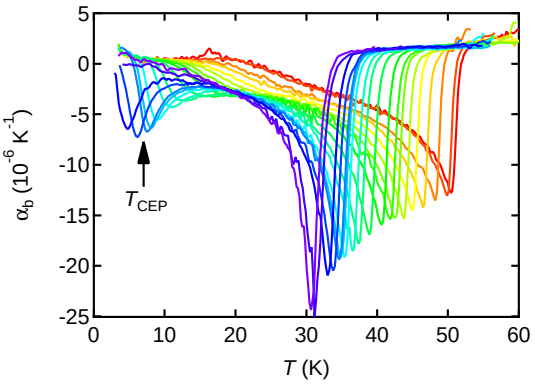

Figure 4.24: Temperature dependence of the thermal expansion coefficient along the b-axis at all measured pressures. The pressures are the same as in fig. 4.23. A zoom at low temperature is presented in fig. 4.25. A selection of these data has been published in the fig.2(a) in ref. [Taufour11].

In addition, below T_C, we observe a clear anomaly at T_x for pressures slightly below 1.19 GPa (see fig. 4.25). It is not visible at 1.21 GPa, above $p_x \approx 1.19$ GPa. At low pressure, only a large hump can be recorded confirming that the switch from FM1 to FM2 corresponds to a broad crossover regime at ambient pressure [Hardy09] and thus the existence of the CEP which terminates the first order line between FM1 and FM2. At low pressure, anomalies can be detected as one inflection point or two (fig. 4.24). Increasing pressure, a minimum is visible in α_b. From fig. 4.25, it is suggested that this minimum is the deepest between 1.15 and 1.17 GPa and between 7.5 and 6.2 K respectively. This suggest that the CEP coordinates are $p_{CEP} \approx 1.16$ GPa, $T_{CEP} \approx 7$ K. Resistivity measurements confirm these values (see section 4.2.4).

In fig. 4.27, the anomalies corresponding to the crossover between FM1 and FM2 are reported. Our resistivity data are in good agreement with previously reported resistivity measurements [Bauer01, Tateiwa01b] but do not perfectly agree with the thermal expansion data. This is not a surprising result, since at ambient pressure the T_x anomaly corresponding to this crossover is given with more than 10 K difference between the different physical quantities (see table 3.1). Above p_{CEP}, at the genuine FM1-FM2 transition, the agreement is very good, as well as for the PM-FM1 transition.

The non magnetic contribution to the relative elongation can be determined by fitting $\Delta L_b/L_b$ (fig. 4.23) in the paramagnetic regime to a T^2 law [Pfleiderer07]. Then, we obtain

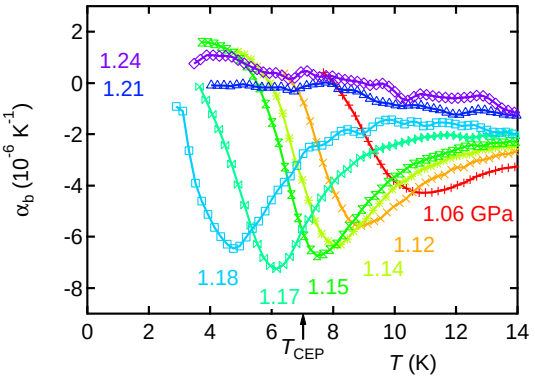

Figure 4.25: Temperature dependence of the thermal expansion coefficient along the b-axis at different pressures. A selection of these data has been published in the fig.2(a) in ref. [Taufour11].

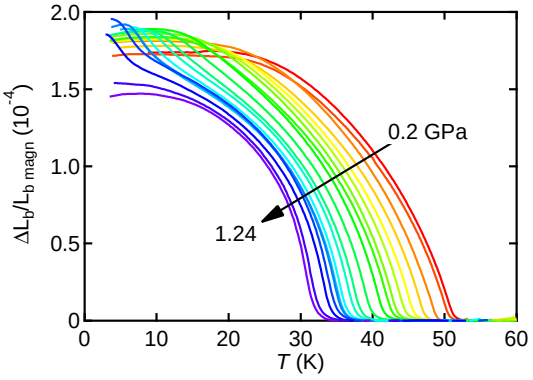

Figure 4.26: Temperature dependence of the magnetic contribution to the relative elongation along the b-axis at all measured pressures. The pressures are the same as in fig. 4.23.

the spontaneous magnetostriction $\Delta L_b/L_{b_{\rm magn}}$ by substracting the non magnetic part to $\Delta L_b/L_b$ (see fig. 4.26). Fine tuning of the pressure allows us to draw $\Delta L_b/L_{b_{\rm magn}}$ as a function of pressure in fig. 4.28. The anomaly at 45 K and 35 K is associated to the PM-FM1 transition. By comparison to the continuity of the spontaneous magnetostriction at that second order transition, we observe a discontinuity at low temperature at the FM2-FM1 transition. This discontinuity changes to a continuity above 7 K (curve at 15 K for fig. 4.28). Thus, the FM1-FM2 transition is first order below 7 K, and the transition line ends up at a CEP.

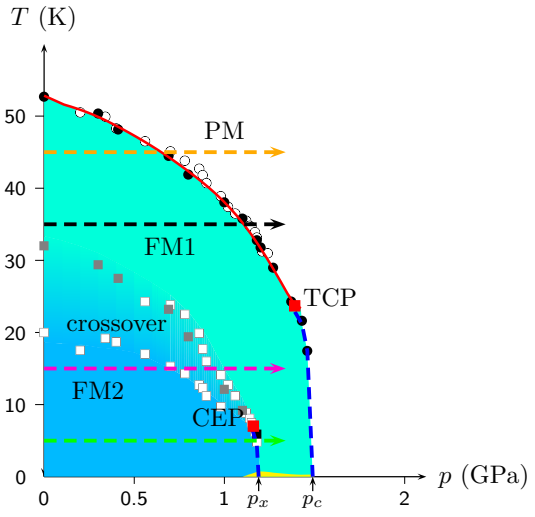

Figure 4.27: Phase diagram of UGe_2 determined by resistivity (full symbol) and thermal expansion (open symbol). Horizontal dashed arrows show the pressure scan of fig. 4.28. The superconducting phase is shown in a light yellow color.

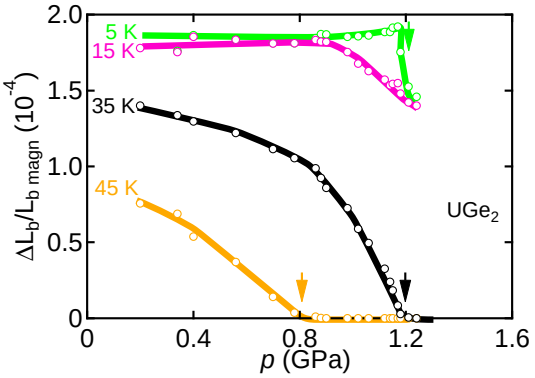

Figure 4.28: Pressure dependence of the isothermal spontaneous magnetostriction along the b-axis [Taufour11].

4.2.3 Comparison with the Results at Ambient Pressure

The measurements of the thermal expansion under pressure come as a confirmation of a complete analysis at ambient pressure of the magnetization, the specific heat and the thermal expansion [Hardy09].

Using magnetization measurements in the framework of the molecular field approximation (MFA), the magnetic heat capacity C_{MFA} can be obtained at several magnetic fields. The lattice contribution to the heat capacity is obtained by subtraction : $C_{\mathrm{lat}} = C - C_{\mathrm{MFA}}$. The fact that the lattice contribution is independent of the magnetic field confirms the validity of the MFA. This simple model neglects the spin-wave excitations, which are indeed negligible in UGe_2 due to the large uniaxial magnetic anisotropy. The lattice contribution can be decomposed into a single Debye function and two Einstein terms, from which a lattice contribution to the volumic thermal expansion can be obtained α_v^{lat}. The magnetic contribution to the volumic thermal expansion is obtained : $\alpha_v^{\mathrm{mag}} = \alpha_v - \alpha_v^{\mathrm{lat}}$. In the case of a system governed by only one energy scale, the thermal expansion is directly proportional to the specific heat and the proportionality constant is the Grüneisen parameter Γ. Therefore one should expect $\alpha_v^{\mathrm{mag}} = \Gamma \cdot C_{\mathrm{MFA}}$. However, this is not the case and it is necessary to consider two energy scale associated to the two states FM1 and FM2. Thus $\alpha_v^{\mathrm{mag}} = \Gamma_{\mathrm{FM1}} \cdot C_{\mathrm{FM1}} + \Gamma_{\mathrm{FM2}} \cdot C_{\mathrm{FM2}}$. The results of this decomposition are given in fig. 4.29.

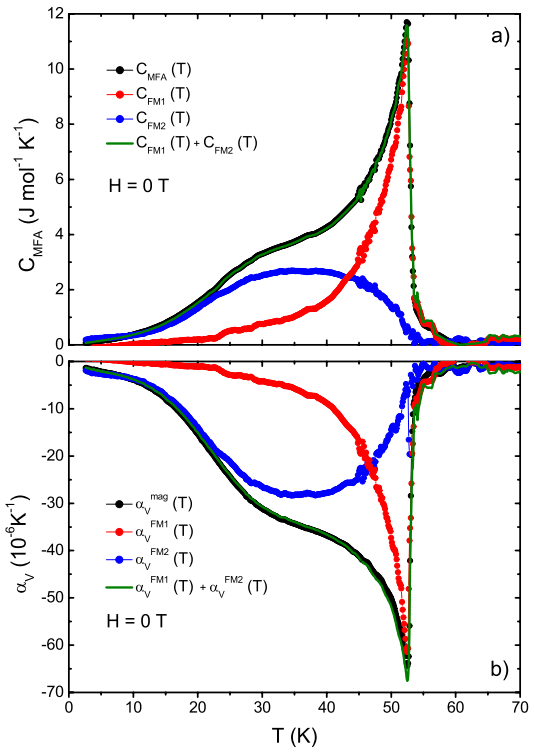

Figure 4.29: Temperature dependence of the magnetic heat capacity (a) and magnetic thermal expansion (b) in zero field. These two quantities are decomposed into two contributions related to FM1 (red) and FM2 (blue) [Hardy09].

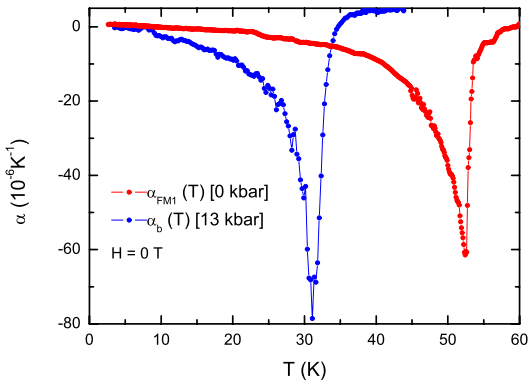

Figure 4.30: Temperature dependence of the ambient pressure FM1 magnetic thermal expansion. It is compared to the thermal expansion measured along the b axis at 13 kbar (this study). Because of its small lattice contribution, $\alpha_b(T)$ is almost entirely of magnetic origin [Hardy09].

Although this analysis is performed from measurements at ambient pressure where both the FM1 and the FM2 phases exist, it is remarkable that the extracted contribution of the FM1 phase (red curves in fig. 4.29) is closely similar to the present results above p_x where only the FM1 phase exists (see fig. 4.30). Especially as there is no hump related to the FM2 contribution. This confirm the validity of the analysis.

4.2.4 Evolution of T_{CEP} in Magnetic Field : the FM1-FM2 Wings

To determine the field evolution of the FM1-FM2 boundary and CEP, the same resistivity measurement used for the field evolution of the PM-FM1 boundary and TCP have been performed. Figure 4.31 shows the temperature variation of $d\rho/dT$ (temperature derivative of the resistivity ρ) at different magnetic fields for three pressures : at 1.1 GPa just below $p_{CEP} \approx 1.16$ GPa, at 1.2 GPa just above $p_x = 1.19$ GPa and at 1.27 GPa between p_x and $p_c = 1.49$ GPa. Two different behaviors are observed : the peak of $d\rho/dT$, characteristic of the FM1-FM2 transition, is either sharpened with magnetic field or broadened. The first case is interpreted as the first order FM1-FM2 transition and the second as the crossover regime. The magnetic field value between these two behaviors is thus defined as H_{CEP}. The corresponding $T_{CEP}(H)$ is obtained as explained in fig. 4.32. Clearly, the field dependence of T_{CEP} must be very small up to 8 T : within the resolution of the field steps of the experiment, the CEP seems to remain at roughly the same temperature.

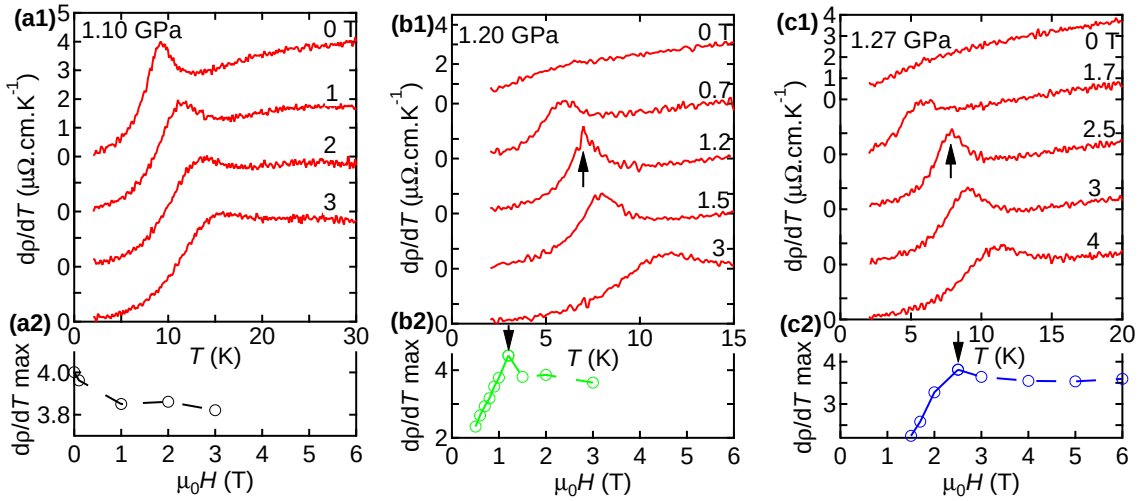

Figure 4.31: Temperature derivative of resistivity $d\rho/dT$ for three typical pressures : (a) below p_{CEP} ; (b) near p_x ; (c) above p_x. (a1) The anomaly smears out with magnetic field. (a2) The value at the maximum (i.e. at T_x) decreases. (b1) Up to 1.2 Tesla, the FM1-FM2 transition is sharper. At higher field, the anomaly is broadened and disappears. (b2) Below 1.2 T, $d\rho/dT_{max}$ increases with field (full line) which is interpreted here as the first order FM1-FM2 transition and then decreases (dashed line) as in a crossover regime. (c1) Below 1.5 Tesla, there is no anomaly (FM1 state). From 1.5 to 2.5 Tesla, anomalies are detected. Above 2.5 Tesla, the anomaly is broadened. (c2) The feature is the same as for 1.2 GPa but shifted to higher fields.

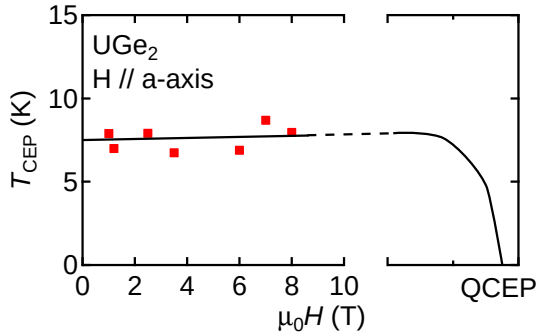

Figure 4.32: Magnetic field dependence of T_{CEP}. Each point is determined as follows (see arrows in fig.3(b) and (c)) : first H_{CEP} is determined by taking the maximum position of $d\rho/dT_{max}$ (for example 1.2 T from the data in fig. 4.31(b2) at 1.2 GPa), and then T_{CEP} is obtained as the position of the peak on the $d\rho/dT$ curve at H_{CEP} (7 K in the data of fig. 4.31(b1) at 1.2 GPa and 1.2 T).

4.2.5 Comparison with the PM-FM1 Wings

The fact that T_{CEP} of the FM1-FM2 transition does not decrease significantly up to 8 T is in contrast with the reduction of the critical point of the PM-FM1 transition (see fig. 4.2). These results agree with the theoretical prediction that H_{QCEP} varies as m_0^3 where m_0 is a microscopic magnetization parameter [Belitz05]. The spontaneous magnetization is indeed $M_0 \approx 0.9\mu_B$ in FM1 and $M_0 \approx 1.4\mu_B$ in FM2 (see section 3.5), so that $H_{\mathrm{QCEP}_{\mathrm{FM1\text{-}FM2}}}$ can be much higher than $H_{\mathrm{QCEP}_{\mathrm{PM\text{-}FM1}}}$. Assuming $H_{\mathrm{QCEP}} \propto M_0^3$, $H_{\mathrm{QCEP}_{\mathrm{FM1\text{-}FM2}}}$ is more than 40 T.

Chapter 5

Results on the Superconducting Phase of UGe_2

5.1 Motivation

The current status of research on the superconducting phase of UGe_2 has been presented in section 3.11. It has been studied by means of resistivity, AC susceptibility, specific heat and NQR experiments. These measurements indicate that the transition temperature T_{sc} is maximum at the pressure p_x where the ground state changes from FM2 to FM1. The superconductivity is observed in a pressure range which is much smaller on the FM2 side than on the FM1 side.

In section 3.11.1, it has been presented that the bulk nature of the superconductivity has been reported by two specific heat measurements [Tateiwa04, Vollmer02]. The first aim of new measurements of the specific heat anomaly on the FM2 side will be to confirm the bulk nature of the superconductivity in the FM2 phase. Unfortunately, the measurements of AC calorimetry presented in this study have not been correctly performed in the FM2 phase :

- The pressure was increased progressively until a superconducting transition was obtained by resistivity measurement.
- As will be described in section 5.3 the superconducting transition is broad in FM2.
- Therefore it was not surprising that nothing was detected in AC calorimetry.
- Thus, not much characterization of the measurement technique such as different frequencies or higher excitation have been tried.
- These characterizations have been done at the first pressure where the superconducting transition by resistivity was sharp, i.e. at 1.20 GPa above p_x in the FM1 state.
- Once the AC calorimetry technique had been shown to be able to detect the superconducting transition, the pressure was not decreased to perform measurements in the FM2 state, because more interesting phenomena have been observed at higher pressure : the wing structure phase diagram presented in chapter 4.

New measurements of AC calorimetry to confirm the bulk nature of the superconductivity in the FM2 phase remain necessary. However, resistivity measurements in the FM2 phase will be presented. It indicates a broad transition to the superconducting state in FM2. Such a broad transition will be very difficult to detect in specific heat measurements. Moreover, new measurements of AC susceptibility have been reported during this study [Kabeya09] and presented in section 3.11.4. The authors conclude that the superconductivity observed in the FM2 phase arise from the FM1 phase introduced

by the pressure inhomogeneity (they estimate a Gaussian pressure distribution of width 0.02 GPa in daphne 7474, which can be compared to our upper value of 0.04 GPa in the same pressure medium).

Also in section 3.11.1, it has been shown by resistivity that the superconductivity is found in a larger pressure range from p_x to p_c, in the FM1 phase. However, the specific heat measurements by Tateiwa *et al.* reveal a jump at the transition which is more rapidly reduced when increasing pressure away from p_x. The phase diagram seems different from resistivity measurement than from specific heat measurements.

The second aim of new specific heat measurements will be to investigate this discrepancy. Our experiment allows one to measure both the resistivity and the AC calorimetry of a UGe_2 single crystal in a piston cylinder cell.

Finally, it has been presented in section 3.11.4 that resistivity measurements in the FM1 phase with magnetic field applied along the a axis reveal a re-entrance of the superconductivity[Sheikin01, Huxley01]. This behavior is associated with the magnetic field re-entrance of the FM2 phase. It has been proposed that the fluctuations associated to the FM1-FM2 transition can enhance the superconductivity[Watanabe02, Sandeman03]. It has also been explained considering a higher T_{sc} in the FM2 than in the FM1 phase[Huxley03b]. This contradicts the idea of non bulk superconductivity in the FM2 phase. However, the re-entrant behavior of the superconductivity has been observed only in resistivity measurements and it has never been confirmed in a bulk measurement.

5.2 Determination of T_{sc} and of the Transition Width in the Specific Heat Measurement

To illustrate the influence of nodes in the gap on the temperature dependent specific heat, I calculated the gap and the specific heat in the framework of BCS theory (weak coupling) and also with a line node such as $\Delta = \Delta_0 \cos\theta$. Such a line node gap is proposed for the specific heat of URhGe [Huxley04], nuclear spin lattice relaxation rate in UGe_2 [Kotegawa04, Harada07] and UCoGe [Ohta10]. The temperature dependence of the gap is shown in fig. 5.1. The low temperature behavior of the specific heat shows a larger specific heat in the case of a line of nodes because low energy excitations exist at the nodes (see fig. 5.2). Consequently, the conservation of entropy implies a smaller jump at the superconducting transition, compared to the s-wave case.

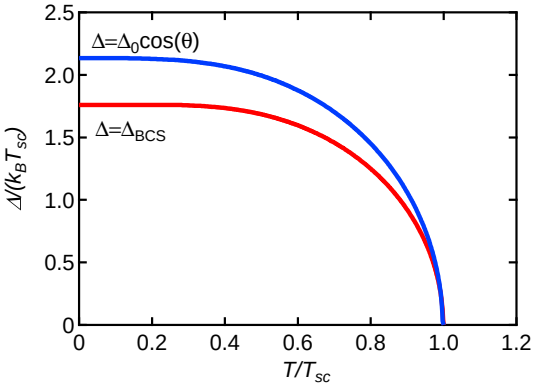

Figure 5.1: Temperature dependence of the gap in the weak coupling BCS theory in the isotropic case and in a line of nodes.

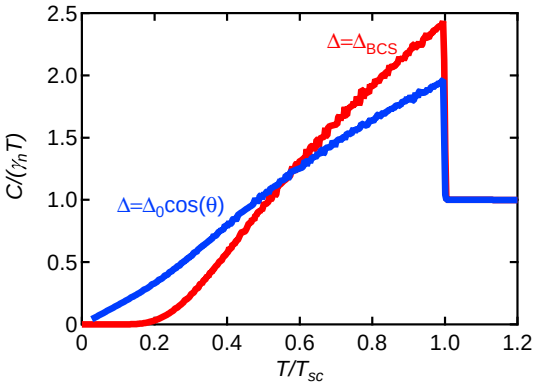

Figure 5.2: Temperature dependence of $C/\gamma_n T$ in the case of s-wave and in the case with a line of nodes.

However, it is not possible in this study to use specific heat measurements in order

to deduce information about the symmetry of the order parameter. Indeed, in the case of ferromagnetic superconductors, a rather large residual specific heat is observed. This residual specific heat can arise from the presence of vortices due to the magnetization, the presence of ungapped band or impurities.... This additional parameter allows one to fit the data within many different order parameters. This is illustrated in fig. 5.3, where it can be seen that both order parameters can reproduce the data. Note that this is true for heat capacity measurements with adiabatic technique. It is even more difficult with AC calorimetry technique, since these measurements cannot be performed in a large temperature range.

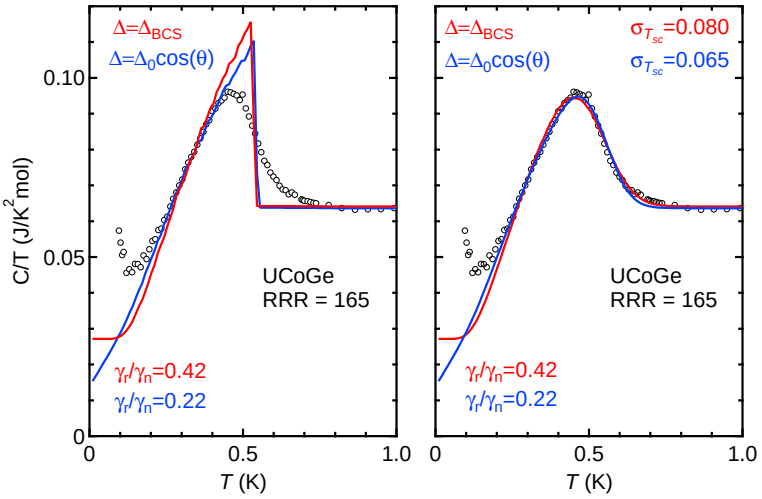

Figure 5.3: Temperature dependence of C/T of UCoGe with fits in the case of a s-wave order parameter and in the case of a line node. In both case, a residual term γ_r have to be considered, so that both theory can reproduce the experiments. On the left panel, a gaussian distribution of T_{sc} with a caracteristic width $\sigma_{T_{sc}}$ have been included. The increase of C/T at the lowest temperature is the nuclear contribution.

Even if in fig. 5.3, the case of a line of node seems a better fit, measurements at lower temperature are necessary. However, these measurements will be complicated by the large nuclear contribution in the specific heat.

Finally, it must be noted that such a weak coupling theory is not expected to be valid in these materials. Calculations of the specific heat in the strong coupling case are more difficult. However, it is possible to have an idea of the influence of the strong coupling using a so-called α-model [Padamsee73], where the gap Δ is simply replaced by $\alpha \cdot \Delta$ (see for example [Bouquet01, Taylor07]). An illustration on the specific heat with $\alpha = 1.5$ is represented fig. 5.4. It can be seen that the downward curvature in the weak coupling case evolves to an upward curvature. In counterpart, the jump at T_{sc} is larger. The addition of this α parameter together with the residual term γ_r (or with a double band : $\gamma_{\uparrow\uparrow}$, $\Delta_{\uparrow\uparrow}$ and $\gamma_{\downarrow\downarrow}$, $\Delta_{\downarrow\downarrow}$) makes it difficult to deduce information on the gap symmetry from the specific heat in these materials.

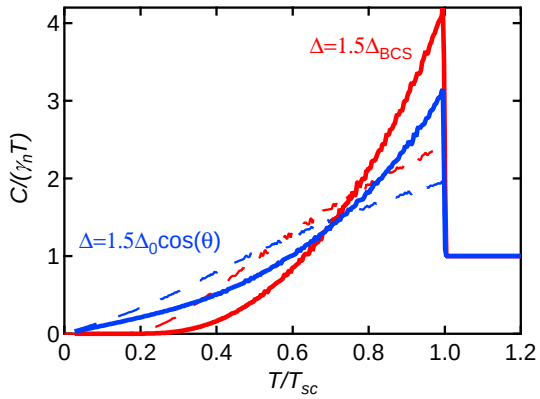

Figure 5.4: Temperature dependence of $C/\gamma_n T$ in the case of s-wave and in the case with a line of nodes using the α model [Padamsee73] to account for the strong coupling. The dotted lines are the results in the weak coupling case ($\alpha = 1$) also plotted in fig. 5.2.

However, it can be used to determine T_{sc} so that the entropy is conserved. Additionaly, it allows a determination of the T_{sc} distribution. In fig. 5.3, a gaussian distribution of T_{sc} with a caracteristic width $\sigma_{T_{sc}}$ have been considered in UCoGe. In what follows, the same procedure will be used on UGe_2 to derive T_{sc} and its caracteristic distribution $\sigma_{T_{sc}}$. No other quantity will be derived from the fits.

5.3 Broad Resistive Transition in the FM2 Phase

5.3.1 From Resistivity Measurements

At 0 Tesla below p_x

The experimental setup has been presented in fig. 2.19 page 34. The resistivity and the AC calorimetry measurements have been done on the same sample at the same time. The pressure was increased at high temperature and low temperature measurements were then performed. The zero resistivity was obtained successively at 1.10 and 1.18 GPa in the FM2 phase and 1.20, 1.24, 1.27, 1.37 and 1.5 GPa in the FM1 phase.

At the two pressures corresponding to the FM2 phase (1.10 and 1.18 GPa), the transition is broad and the zero resistivity is obtained only after a long tail. This can be seen in fig. 5.5. At 1.10 GPa, the difference between the onset temperature T_{onset} and the temperature at which zero resistivity is observed $T_{\rho=0}$ is larger than 500 mK. It remains larger than 150 mK at 1.18 GPa. Such broad superconducting transitions cannot arise from a poor sample quality since a sharp transition is observed on the same sample at 1.20 GPa : $T_{\text{onset}} - T_{\rho=0} < 50$ mK (see later in fig. 5.7).

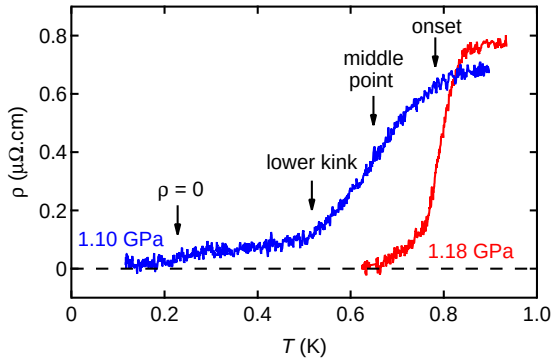

Figure 5.5: Superconducting transition of resistivity in the FM2 phase.

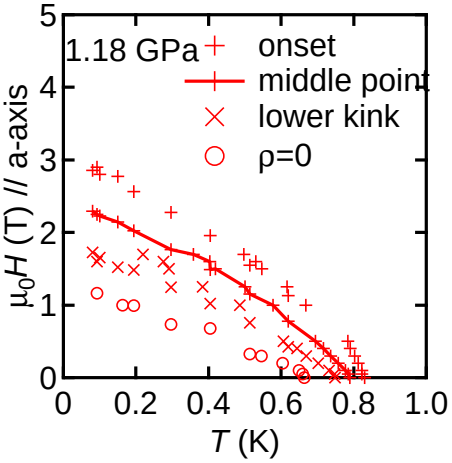

Figure 5.6: Critical field versus temperature phase diagram at 1.18 GPa determined by resistivity measurements.

Above p_x for Magnetic Field $H > H_x$

Above $p_x = 1.19$ GPa in the FM1 phase, the superconducting transition is sharper. Applying magnetic field along the magnetization axis a-axis restores the FM2 state. It affects the superconducting transition by increasing the resistivity transition width (see fig. 5.7).

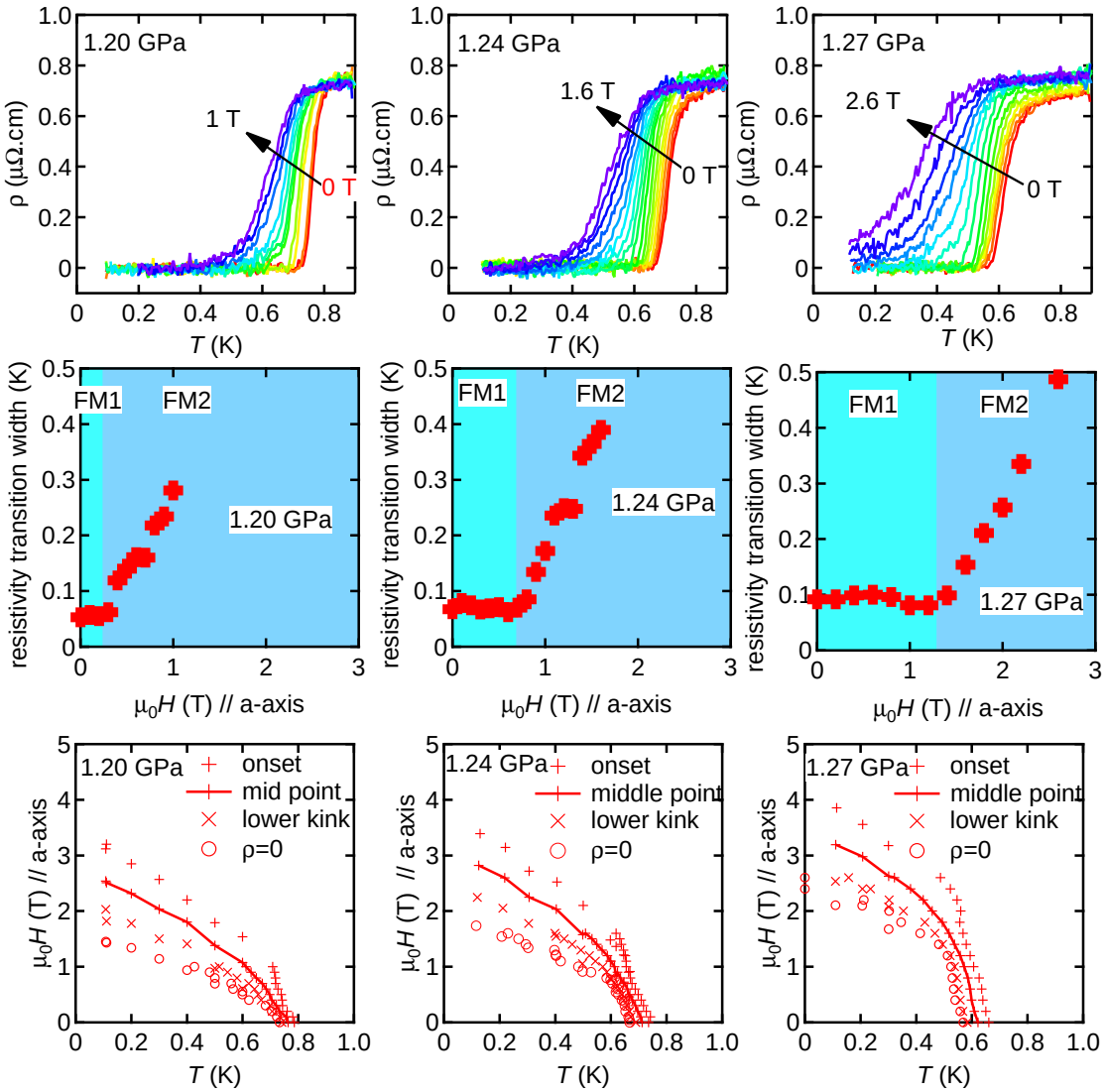

Figure 5.7: a)Temperature dependence of resistivity at different magnetic field. b)Magnetic field dependence of the resistivity transition width. c)Critical field versus temperature phase diagram determined by resistivity measurements.

Two obvious observations can be drawn from these measurements. First, as can be seen on fig. 5.8 the pressure range where the superconductivity is observed is much narrower in FM2 than in FM1. Second, the resistive transition width is increased in the FM2 phase in comparison to the FM1 phase. This change in width is clear at 0 T by changing pressure (fig. 5.9), but also at constant pressure by changing the magnetic field (fig. 5.7).

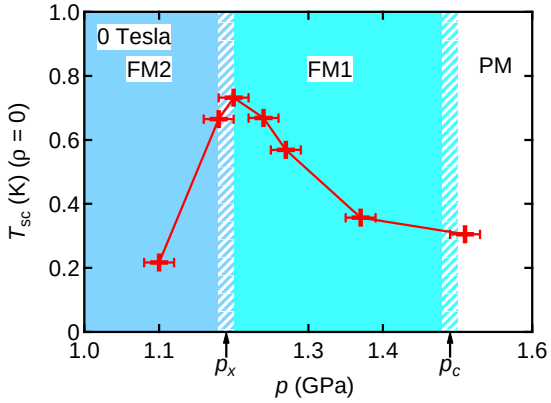

Figure 5.8: Temperature versus pressure phase diagram of the superconducting state determined by resistivity measurements.

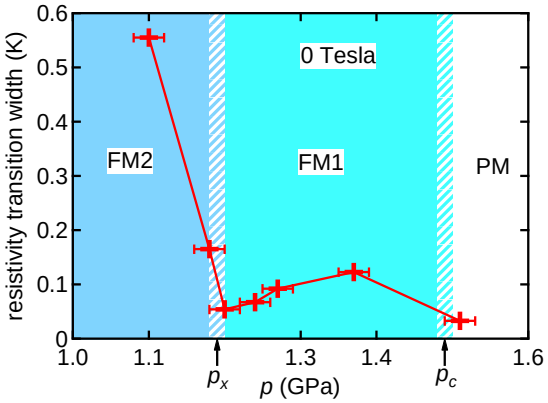

Figure 5.9: Transition width of resistivity versus pressure.

5.3.2 From AC Calorimetry Measurements

The anomaly of the superconducting transition at 1.20 GPa can be seen in fig. 5.10(a). It is obtained from AC calorimetry measurements using two frequencies at which a simple model of AC calorimetry seems valid [Sullivan68] (see section 2.4). In fig. 2.28 page 36, our result have been compared to the only previous report of specific heat on a single crystal of UGe_2 performed by Tateiwa *et al.*. In Tateiwa's report, the specific heat of all the pressure cell is measured by adiabatic technique. Since both curves are qualitatively the same, it shows that the small value of the specific heat jump does not arise from the AC calorimetry technique.

As is visible on fig. 5.10(a), the superconducting anomaly in the specific heat is rapidly suppressed under magnetic field at 1.20 GPa. It is not possible to see the superconducting anomaly above 0.5 Tesla. Following the description made in section 5.2, the determination of T_{sc} and its caracteristic distribution $\sigma_{T_{sc}}$ are illustrated on fig. 5.10(a) by full black lines. The results are in agreement with resistivity measurements : T_{sc} decreases with applied magnetic field and the transition is broadened as soon as the FM2 phase is induced. The evolution of the T_{sc} distribution in figure 5.10(b) is very similar to the one of the resistivity transition width (also displayed on fig. 5.7 page 95).

We note that the superconducting transition cannot be detected in our AC calorimetry measurement as soon as the distribution of T_{sc} is larger than 150 mK. As concluded from the resistivity measurements, the distribution of T_{sc} increase when entering the FM2 phase.

5.3.3 Discussion

It has been shown from AC calorimetry measurements and resistivity measurements that the transition width is increased in the FM2 phase by comparison with the FM1 phase.

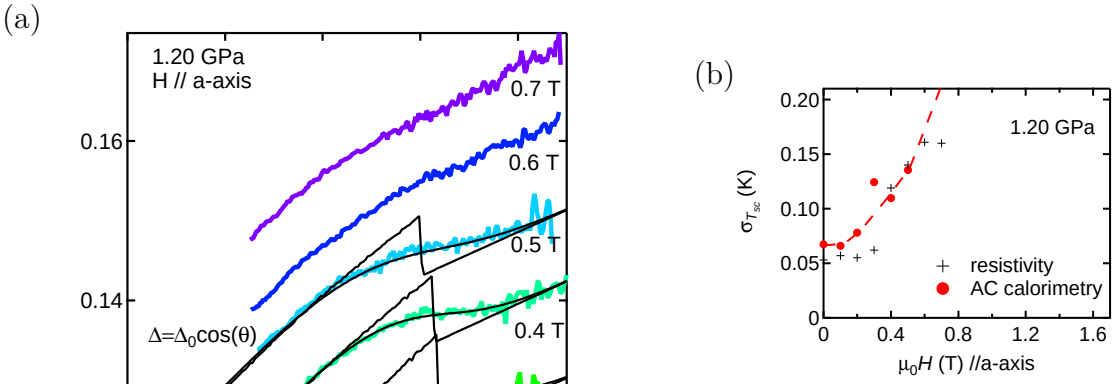

Figure 5.10: (a) Temperature dependence of C/T at 1.20 GPa at different magnetic field applied along the a-axis. The data are offset for clarity. The superconducting transition temperature T_{sc} is determined by the conservation of entropy as indicated by the black curves. These curves have been inferred using the calculations of $\frac{C}{\gamma T}\Big|_{theo}$ for a line node illustrated in fig. 5.2 and assuming a residual term γ_r. A background signal have also been added and assumed to be proportional to the temperature. Such background signal depends on the choice of frequencies used in the AC calorimetry measurement (see fig. 2.27 page 36).
$\frac{C}{T} = \frac{C}{\gamma T}\Big|_{theo} \cdot \gamma_n \left(1 - \frac{\gamma_r}{\gamma_n}\right) + \gamma_n \frac{\gamma_r}{\gamma_n} + B \cdot T$
The broadening of the curves due to a gaussian distribution of T_{sc} is also shown. (b) Caracteristic width of the distribution of T_{sc} as a function of magnetic field. The line is guide to the eye. The resistivity transition width determined as $T_{onset} - T_{\rho=0}$ is also displayed. T_{onset} and $T_{\rho=0}$ are defined on fig. 5.5 page 94.

One may conclude that the superconducting transition observed in the FM2 phase is due to impurity phases of FM1. Because the FM1-FM2 transition is of first order, and because of the pressure inhomogeneity, parts of the sample are in the FM1 state even below p_x. As presented in section 3.11.4 page 61, in ref. [Kabeya09], the superconductivity observed by AC susceptibility in the FM2 phase is attributed to the pressure gradient (Gaussian pressure distribution of width 0.02 GPa in daphne 7474). Our results are compatible with this conclusion.

Another explanation is also available : the increase of the transition width in FM2 phase can be explained by the fact that the pressure range is smaller. The pressure inhomogeneity could indeed create a larger T_{sc}-distribution in the FM2 state than in the FM1 state, and thus a larger transition.

To distinguish between the two interpretations, a significant improvement of the pressure inhomogeneity will be necessary. In the first case, the transition will remain broad but will be observed in a smaller pressure range in the FM2 phase. In the second case, the transition will be less broad and will still be observable in the same pressure range. However, the pressure inhomogeneity corresponds to a Gaussian distribution of width ~ 0.02 GPa in daphne 7474 (estimated in ref. [Kabeya09]), and significant improvement seems unlikely.

Thus, it is clear that the transition is broadened in the FM2 phase. It can arise from non bulk superconductivity or because of the fact that T_{sc} is strongly pressure dependent in the FM2 phase. Unfortunately, if the superconductivity is bulk in FM2 and shows a broad transition due to the pressure dependence of T_{sc}, it will be difficult to detect in specific heat measurements.

If such experiment is attempted again, the use of helium as a pressure transmitting medium might be necessary even though other improvements will certainly be required.

5.4 Bulk Evidence for a Field Enhanced Superconductivity

5.4.1 Magnetic Field Dependence

Three characteristic C/T curves at different magnetic field are displayed in fig. 5.11. The full set of curves will be showed later. The most interesting result is observed at 1.24 GPa. Contrary to the results at 1.20 GPa at which the anomaly cannot be observed at 0.6 T, the anomaly remains clearly observable at 0.6 T at 1.24 GPa. More suprisingly, the superconducting transition temperature T_{sc} seems higher, or at least sharper, at 0.6 T than at 0 T. These conclusions which are drawn by looking at the curves without any analysis are confirmed when T_{sc} is determined by the conservation of entropy as showed on fig. 5.12 where the full set of curves at 1.24 GPa is displayed.

The maximum of T_{sc} is obtained at 0.6 T which correspond to the phase transition at H_x from FM1 to FM2 (fig. 5.12(c)). Entering the FM2 phase above H_x, the transition width is increased and the AC calorimetry anomaly is rapidly suppressed.

One advantage of the experimental setup is that we can follow the FM1-FM2 transition by AC calorimetry, especially inside the superconducting phase where the resistivity is zero (figs. 5.13 and 5.14). This evolution is reported in the phase diagram of fig. 5.12(c).

At 1.27 GPa, the phenomena are similar (see fig. 5.11 and 5.15) : the superconducting transition temperature T_{sc} seems higher, or at least sharper, with applyied magnetic field

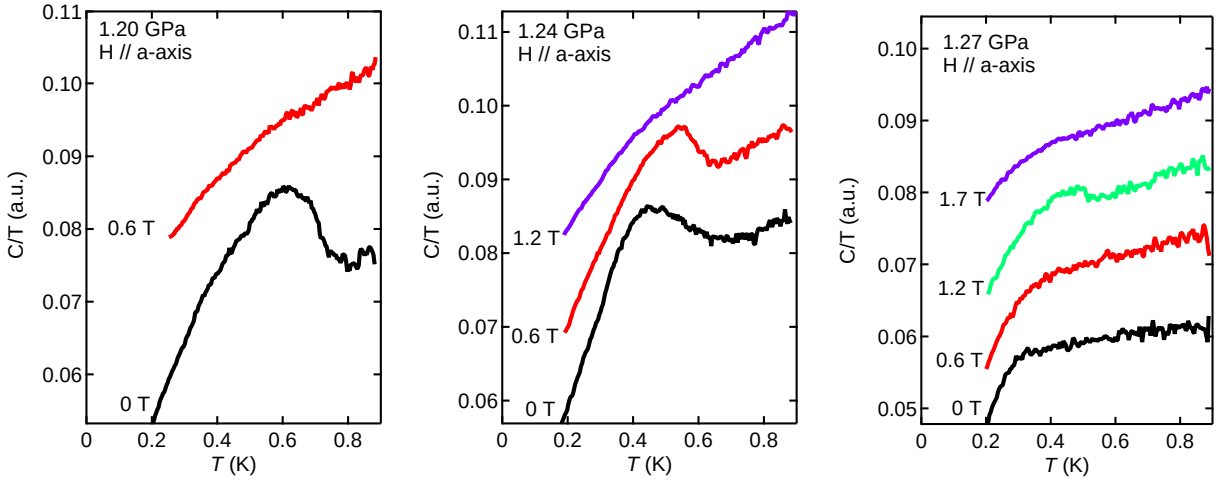

Figure 5.11: Temperature dependence of C/T at different magnetic field at 1.20, 1.24 and 1.27 GPa. The data are shifted for clarity.

close to H_x. No jump can be measured below 0.8 T where a small jump appears and is maximum at $H_x = 1.2$ T (fig. 5.15(c)). Above H_x, the anomaly disappears. However, even at 1.2 T, the transition is broad and the distribution of T_{sc} is $\sigma_{T_{sc}} \approx 120$ mK.

Although AC calorimetry reveals a slight field enhancement of the superconducting transition temperature T_{sc}, or at least sharper anomalies, we remark that there is no enhancement of T_{sc} determined by resistivity at 1.24 and 1.27 GPa. This is certainly due to the fact that at low magnetic field, the superconductivity is sensitive to filamentary superconductivity. Note also that the pressure dependence of T_{sc} is large at these pressures (see fig. 5.8 page 96). At higher pressure, the critical field H_x is higher and the pressure dependence of T_{sc} is smaller. Thus, the enhancement of T_{sc} is visible by resistivity (see fig. 5.17 at 1.37 GPa, which is similar to the previous report at 1.35 GPa [Sheikin01, Huxley01]). Unfortunately, one of the thermocouple wire broke and AC calorimetry could not be measured. After remaking the set up, this pressure could not be reached again. However, the AC calorimetry signal is already very small at 1.27 GPa and it seems unlikely that it can be measured at 1.37 GPa.

5.4.2 Discussion

In addition to UGe_2, such field enhanced superconductivity have also been observed by resistivity in URhGe (fig. 5.18) and UCoGe (fig. 5.19). In all of these compounds, it is associated to a metamagnetic transition, but of different nature. In URhGe, the re-entrant superconductivity is associated to a reorientation of the magnetization axis (see fig. 5.20[Lévy05, Hardy11]) : the re-entrant superconductivity is observed for a magnetic field $H \parallel b$ perpendicular the the magnetization $M \parallel c$. The case of UCoGe remains unclear but might be similar to URhGe. Indeed, as shown in fig. 5.19, the enhancement of T_{sc} is linked to the ferromagnetic instability. In UGe_2, the re-entrant superconductivity is observed for a magnetic field $H \parallel a$ parallel to the magnetization axis $M \parallel a$. It is associated to a metamagnetic transition which is the transition from FM1 to FM2. In the case of UGe_2, it is an increase of the magnetic moment without any reorientation.

Despite the fact that no pressure is required to observe superconductivity in URhGe and UCoGe, the field enhanced superconductivity has not been observed by a bulk probe.

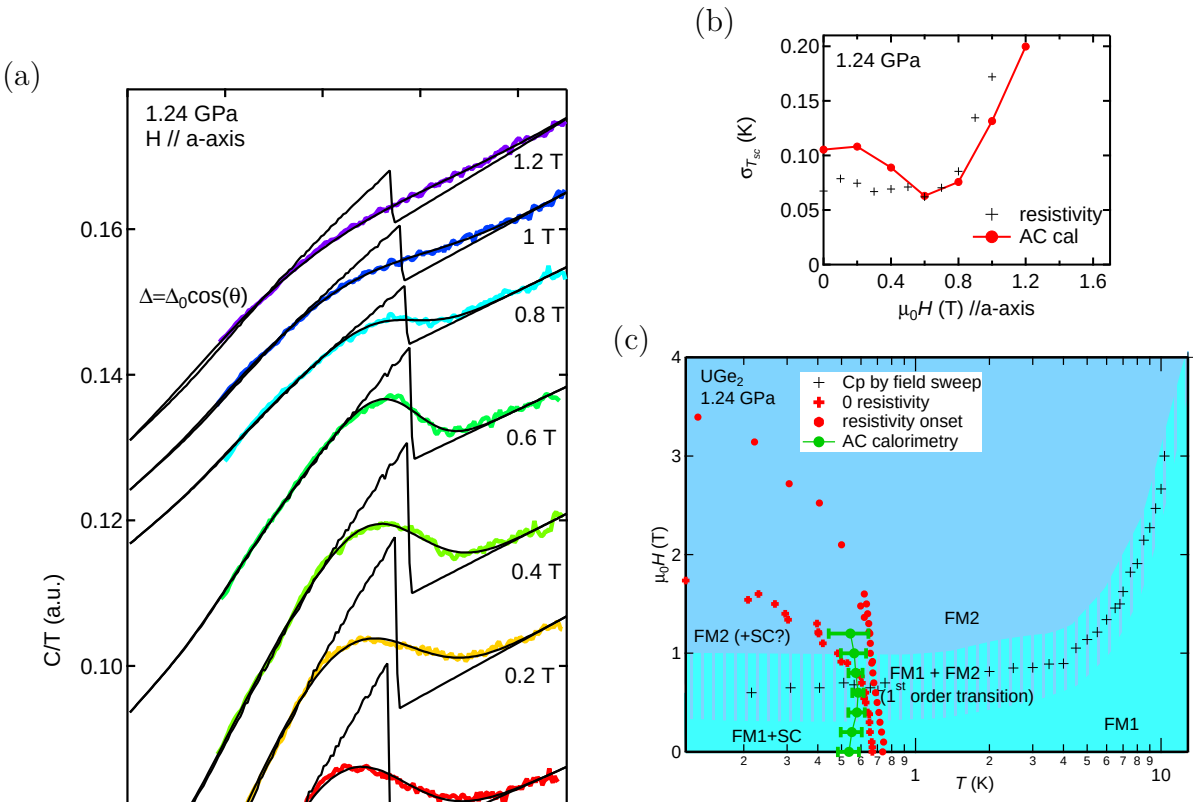

Figure 5.12: (a) Temperature dependence of C/T at 1.24 GPa at different magnetic field applied along the a-axis. The data are offset for clarity. The superconducting transition temperature T_{sc} is determined by the conservation of entropy as indicated by the black curves. The broadening of the curves due to a gaussian distribution of T_{sc} is also shown. (b) Caracteristic width of the distribution of T_{sc} as a function of magnetic field. The line is guide to the eye. The resistivity transition width determined as $T_{onset} - T_{\rho=0}$ is also displayed (see also fig. 5.7) (c) Critical field versus temperature phase diagram determined by resistivity measurements and AC calorimetry.

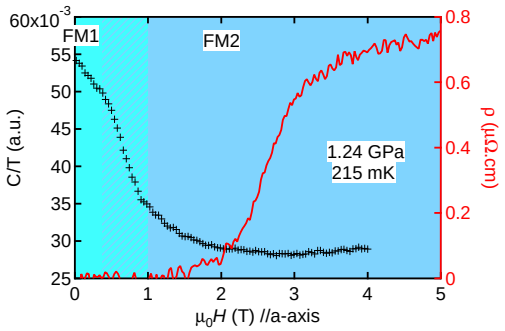

Figure 5.13: Magnetic field dependence of C/T and of the resistivity 215 mK at 1.24 GPa.

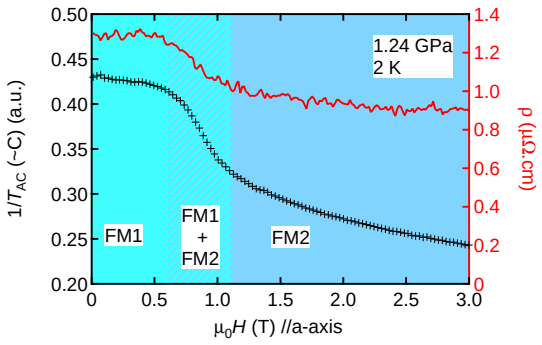

Figure 5.14: Magnetic field dependence of AC calorimetry signal and of the resistivity 2 K at 1.24 GPa.

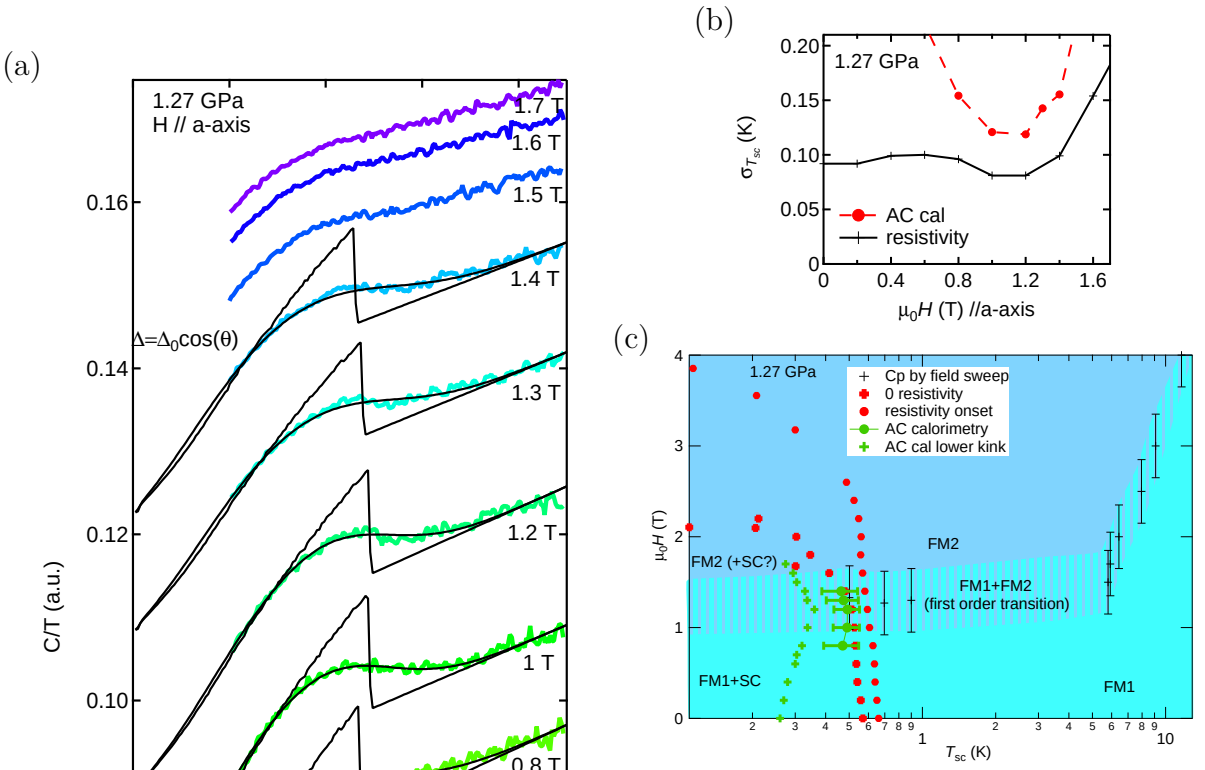

Figure 5.15: (a) Temperature dependence of C/T at 1.27 GPa at different magnetic field applied along the a-axis. The data are offset for clarity. The superconducting transition temperature T_{sc} is determined by the conservation of entropy as indicated by the black curves. The broadening of the curves due to a gaussian distribution of T_{sc} is also shown. (b) Caracteristic width of the distribution of T_{sc} as a function of magnetic field. The line is guide to the eye. The resistivity transition width determined as $T_{onset} - T_{\rho=0}$ is also displayed (see also fig. 5.7) (c) Critical field versus temperature phase diagram determined by resistivity measurements and AC calorimetry.

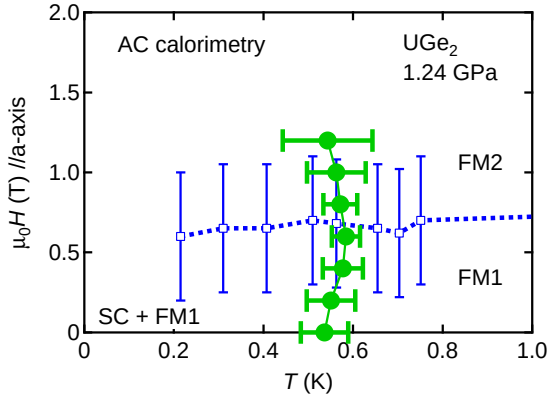

Figure 5.16: Critical field versus temperature phase diagram at 1.24 GPa determined by AC calorimetry. Error bars of the superconducting transition (green circles) represent the distribution of T_{sc}. Error bars of the FM1-FM2 transition (blue squares) represent the width of the transition as shown in figs. 5.13 and 5.14.

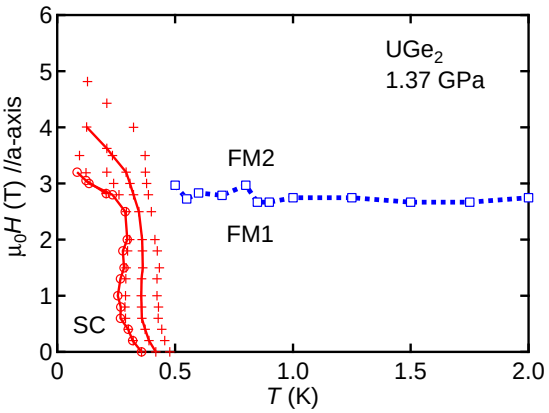

Figure 5.17: Critical field versus temperature phase diagram at 1.37 GPa determined by resistivity measurements.

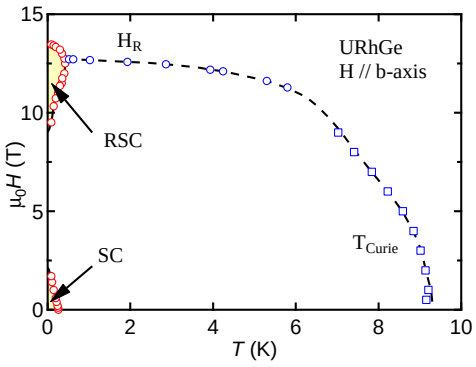

Figure 5.18: Critical field versus temperature phase diagram of URhGe determined by resistivity measurements.

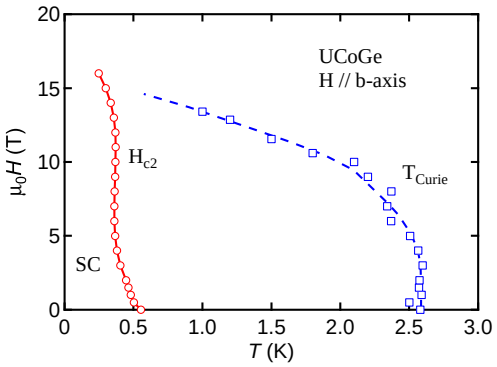

Figure 5.19: Critical field versus temperature phase diagram of UCoGe determined by resistivity measurements.

This can be explained by several reasons. First, good single crystals of URhGe and UCoGe are difficult to obtain. Second, the metamagnetic transition that create the enhancement is strongly angular dependent. Third, high magnetic fields are necessary. Recently, the upward curvature of the critical field up to 8.5 T has been confirmed in UCoGe from thermal conductivity measurements [Howald11]. Measurements above 12 T at which the enhanced superconductivity is observed are scheduled. The case of UGe_2 seems more simple experimentally despite the necessity of applying pressure : the crystals are much better (RRR> 300 in UGe_2 which is ten times larger than usual samples of UCoGe and all samples of UGe_2 show superconductivity which is not the case for URhGe), the angular dependence seems weak, and the magnetic fields are smaller.

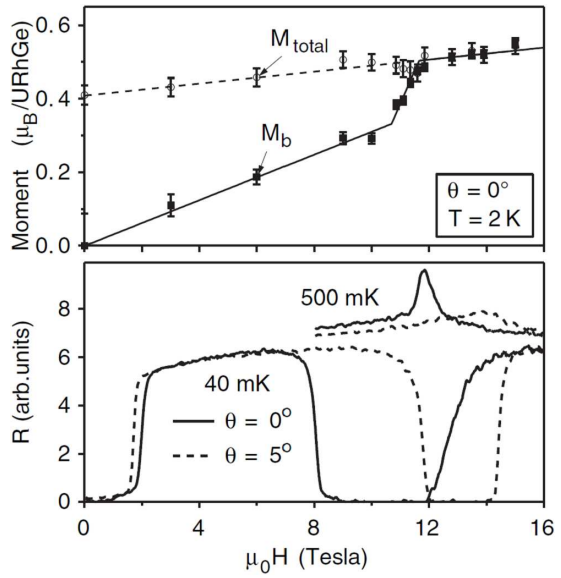

Figure 5.20: The upper panel shows the total magnetic moment and the component of the moment parallel to the b axis (in units of Bohr magnetons per URhGe) for magnetic field applied along the b axis ($\theta = 0$), measured by neutron scattering at 2 K (the lines are to guide the eye). The moment parallel to b increases rapidly at H_R. Error bars show the estimated standard deviation of each measurement. The lower panel shows the electrical resistance of the sample over the same field range at temperatures of 40 mK and 500 mK. At 500 mK the sample is in the normal state and a clear peak in the resistance is seen at H_R. At 40 mK the resistance is zero for a range of fields about H_R. This pocket of field induced superconductivity occurs in addition to that observed below 2 T[Lévy05].

Magnetic field re-entrant superconductivity has also been observed in Chevrel phase compounds [Fischer75, Meul84] and in organic superconductors [Konoike04, Uji01, Uji05]. It can be understood as the Jaccarino-Peter effect [Jaccarino62] where the applied magnetic field is compensated by an opposite exchange field. The re-entrant superconductivity in these materials is observed when the applied magnetic field is parallel to the exchange field. A completely different situation is observed in URhGe and UCoGe in which the re-entrant superconductivity is observed only for magnetic field perpendicular to the magnetization axis. Moreover, the Jaccarino-Peter effect is distinct from other phase transitions seen at different fields, whereas in URhGe, UCoGe and UGe_2, the re-entrant superconductivity is associated to a metamagnetic transition.

Several explanations have been given to explain these field enhanced superconductivity.

Influence of the Effective Mass

The critical field given by the orbital limit is :

$$\mu_0 H_{c_2}^{\mathrm{orb}}(T) = \frac{\mu_0 \phi_0}{2\pi\xi(T)}$$

where ϕ_0 is the quantum flux $\phi_0 = \frac{h}{2e}$ with e the electron charge and h the Planck constant. The coherence length $\xi(T)$ is defined in the BCS theory by :

$$\xi(T) = \frac{\hbar v_F}{\pi\Delta(T)}$$

where $\Delta(T)$ is the superconducting gap and v_F is the quasiparticule velocity at the Fermi energy. Assuming $\Delta(0) \propto k_B T_{sc}$, we have :

$$\mu_0 H_{c_2}^{\text{orb}}(0) \propto \frac{T_{sc}^2}{v_F^2} \propto \frac{m^{*2} T_{sc}^2}{k_F^2} \tag{5.1}$$

Using a McMillan type formula [McMillan68] simplified to :

$$T_{sc} = T_0 e^{-\frac{1+\lambda}{\lambda}}$$

where λ is the mass renormalization factor ($m^* = m_B + m^{**} = m_B(1+\lambda)$ with the band mass m_B and the extra mass m^{**} directly related to the superconducting pairing), we can obtain :

$$T_{sc} = T_0 e^{-\left(\frac{m_B}{m^{**}}+1\right)} \tag{5.2}$$

Thus, if m^{**} is increased under magnetic field, T_{sc} is increased and so is H_{c_2}. The effective mass m^* can be deduced from the A coefficient of the T^2 term of the resistivity assuming $m^* \propto \sqrt{A}$, by the γ term of the specific heat with $m^* \propto \gamma$, or from magnetization measurements through the Maxwell relation : $\frac{\partial C}{\partial H}\Big|_{T,p} = T \frac{\partial^2 M}{\partial T^2}\Big|_{H,p}$. In the three cases, an enhancement of the effective mass at the reorientation field H_R is observed (see fig. 5.21 [Hardy11]).

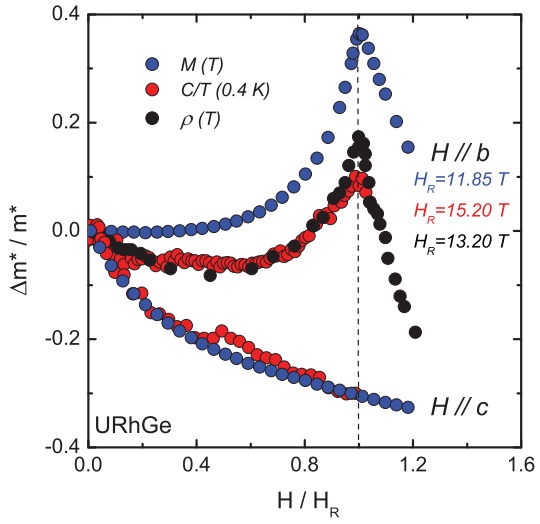

Figure 5.21: Comparison of the field dependence of the effective mass m^* for $H \parallel b$ and $H \parallel c$ obtained from magnetization, specific-heat, and transport measurements [Hardy11].

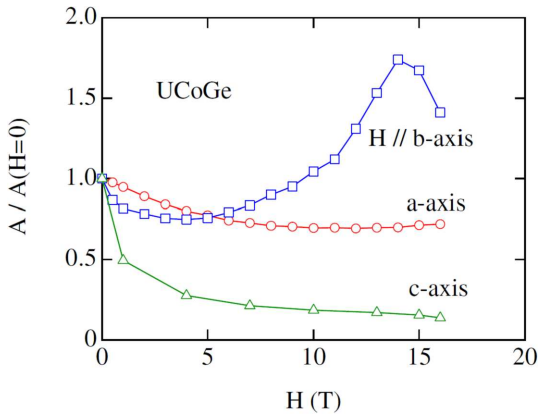

Figure 5.22: Field dependence of the normalized A coefficient of resistivity for $H \parallel a$, b, and c-axis [Aoki09b].

Assuming that k_F and m_B are not modified under magnetic field, the observed increase of the effective mass in URhGe for field parallel to the b axis can explain the re-entrant superconductivity [Miyake08].

In fig. 5.22, a similar enhancement of the effective mass is observed in UCoGe for the field applied along the b-axis at which the re-entrant curvature of H_{c_2} have been observed.

Up to know, a change of the Fermi surface at H_R has not been reported in URhGe and UCoGe (no measurements have been reported). This is not the case in UGe_2 where a change is observed at H_x (see section 3.10 page 56). Therefore, the above simple model [Miyake08] is no longer valid. However, the field dependence of the effective mass will have a qualitatively similar influence.

Influence on the Pairing Interaction

After the experimental results on UCoGe (see section 2.6.2), the influence of the magnetic field on the pairing interaction has been considered [Mineev11a]. Starting from a Landau development of the free energy, it has been shown that for a magnetic field applied perpendicular to the magnetization axis, the Curie temperature will decrease, as well as the magnetization along the easy axis. This leads to an increased strength of the pairing interaction.

However, it cannot be applied to UGe_2, since an increase of the magnetization along the easy axis is observed at H_x.

In [Sandeman03], another calculation has been done in the case where the superconducting pairing is mediated by the spin fluctuation with an interaction potential derived by Fay and Appel [Fay80] :

$$V_{\sigma\sigma}(\mathbf{q}) = \frac{I^2\chi^{(0)}_{-\sigma-\sigma}(\mathbf{q})}{1 - I^2\chi^{(0)}_{\sigma\sigma}(\mathbf{q})\chi^{(0)}_{-\sigma-\sigma}(\mathbf{q})}$$

where I is the repulsive Hubbard-type contact interaction acting between opposite spins and $\chi^{(0)}_{\sigma\sigma}(\mathbf{q})$ is the Lindhard response. The large density of states giving rise to the magnetization step (see section 3.7) is also able to enhance the superconductivity in the ferromagnetic state. However, ref. [Monthoux01] shows that a McMillan type formula does not seem to exist so that comparison with experiments is difficult.

Clearly, it is shown here that the field enhanced superconductivity previously observed by resistivity measurements is a bulk phenomenon from AC calorimetry measurements, but a theoretical investigation remains to be done in order to make a quantitative confrontation with the observations. On the experimental side, careful measurements of the anisotropy of the critical field H_{c_2} must be performed.

5.5 The Specific Heat Jump

The anomaly at the superconducting transition in the specific heat measurements can be compared to the other ferromagnetic superconductor URhGe and UCoGe (fig. 5.23). Note that our AC calorimetry signal has a shape which is closely similar to the results of these adiabatic techniques. This indicates that the AC calorimetry signal is very close to detect correctly the heat capacity anomaly.

The specific heat jump at the superconducting transition is smaller in UGe_2 than in URhGe and UCoGe. Before this study, one might think that it arises from experimental precision since in UGe_2, the specific heat has been measured by subtracting the signal of a pressure cell to a (sample + pressure cell) system. Our study by AC calorimetry confirms this small jump value for UGe_2. Moreover, the pressure inhomogeneity or the pressure dependence of T_{sc} cannot be taken as an explanation of this smaller anomaly. Indeed, the biggest jump is observed in UCoGe, where the distribution of T_{sc} is found to be around 65 mK (see fig. 5.3 page 93). In UGe_2, at 1.20 GPa, the same T_{sc} distribution is observed (see fig. 5.10(b) page 97), although the specific heat jump at the superconducting transition is more than 2 times smaller.

It is interesting to remark on fig. 5.23 that the relative jump of specific heat at the superconducting transition depends on the magnetic moment. As it has already been mentioned in section 3.11.3 page 60, a reduced jump can occur for several reasons [Huxley04]. The presence of a finite field due to ferromagnetism can explain a smaller

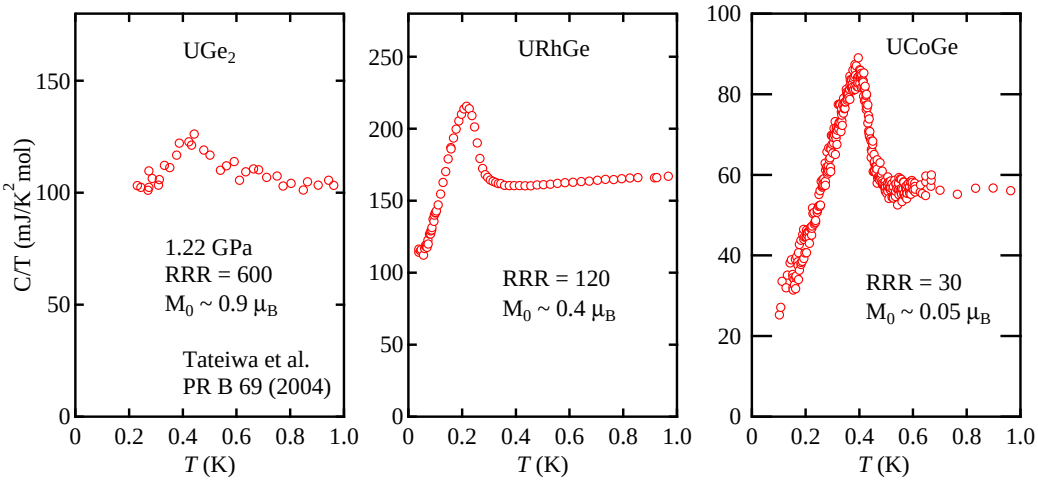

Figure 5.23: Temperature dependence of the specific heat at low temperatures in UGe_2, URhGe and UCoGe. The data of UGe_2 were cited from ref.[Tateiwa04]

jump in UGe_2 compared to URhGe and UCoGe. As given in table 5.1, the internal field due to the magnetization and neglecting the demagnetization effect is 0.17 T in the FM1 phase of UGe_2 and more than 10 times smaller in UCoGe. It is difficult to estimate the residual contribution due to the self induced vortex without knowing H_{c_1}, the coherence length and the demagnetization effect. However it can be estimated roughly from the ratio of the internal field H_{int} over the critical field H_{c_2}. This ratio gives around 10 % for the residual term in UGe_2 and 2 % in UCoGe. It is around 65 % from our specific heat measurement in UGe_2 and 20 % in UCoGe (see fig. 5.3 page 93).

Another possibility is that since the energy splitting between the majority and the minority spin band is stronger in UGe_2, it can result in an almost ungapped band [Huxley04, Harada07]. Note that in the NQR experiments, the residual state is around 20 % of the normal state [Harada07] or 30 % in ref. [Kotegawa05]. In our AC calorimetry experiments (and also in Tateiwa's results), the residual state is more than 60 %. Let us suppose that the density of state in the majority band is larger than the density of states in the minority band (In the double peak density of states scenario, the majority Fermi level sits between the two peaks in the FM1 state [Sandeman03]). Then, the fact that the residual state is larger than the superconducting state in our specific heat measurements would imply that the residual part arises from an ungapped band which would be the majority one. This is in agreement with the fact that in the Fay and Appel theory [Fay80], the superconducting transition temperature is higher for the minority band than for the majority one (see fig. 5.24 and note that the minority band is represented by up spin in ref. [Fay80]). However, the opposite conclusion is given in the NQR experiments : the minority band is supposed ungapped [Kotegawa05, Harada07]. Measurements at lower temperatures are necessary for a better estimation of the residual part.

Since before our measurements, the specific heat anomaly was reported only at 0 T, it has been proposed that the small value of the specific heat jump could be due to spatial inhomogeneity of the superconductivity due to the suppression of superconductivity at magnetic domain boundaries [Huxley04]. It could be stronger in UGe_2 than in URhGe and UCoGe. In ref. [Sakarya05], the domain-wall thickness is estimated as 0.22 μm which represent less than 10% of the volume. Similar studies in URhGe and UCoGe would be

interesting for comparison. However, we detect the specific heat anomaly at magnetic field far above 0.02 T at which the sample can be considered monodomain [Pfleiderer02].

Other reasons can reduce the specific heat jump more equivalently in the 3 compounds with respect to the BCS case [Huxley04], such as the presence of nodes in the order parameter, the pair breaking due to non-magnetic impurities and defects.

	UGe_2		URhGe	UCoGe	references
	FM2	FM1			
Structure Space group	Ortho. *Cmmm*		Ortho. *Pnma*	Ortho. *Pnma*	
T_C (K)	52	~ 30	9.5	~ 3	
M_0 (μ_B)	1.5	0.9	0.4	~ 0.05	[Pfleiderer02, Tran98, Huy08]
$\mu_0 H_{\rm int}$ (T)	0.28	0.17	0.08	~ 0.01	
domain size (μm)	$4-5$		~ 20	~ 10	[Sakarya05, Dolocan05, Hykel11]
domain-wall thickness (μm)	< 0.22				[Sakarya05]
$H_{\rm monodom}$ (T)	< 0.02			< 0.02	[Pfleiderer02, Hykel11]
γ (mJ.K^{-2}.mol^{-1})	34	100	160	55	[Tateiwa01b, Aoki01, Huy07]
$T_{sc_{max}}$ (K)	0.7		0.26	0.7	[Saxena00, Aoki01, Huy07]
$\Delta C/(\gamma_n T_{sc})$	~ 0.3		0.6	0.7	[Tateiwa04, Aoki01, Huy07]
$H^a_{c_2}$ T	1.5†		2.5	> 30	[Kobayashi02, Aoki09b]
$H^b_{c_2}$ T	2.4‡		2	18	
$H^c_{c_2}$ T	5‡		0.7	0.6	
re-entrant superconductivity (RSC)	none	$H \parallel a \parallel M_0$ increase of M_0 FM1-FM2	$H \parallel b \perp M_0$ reorientation FM instability	$H \parallel b \perp M_0$? FM instability	[Sheikin01, Lévy05, Aoki09b] [Lévy05] [Miyake08, Aoki09b]

Table 5.1: Characteristic properties of UGe_2, URhGe and UCoGe. M_0 is the ordered moment. $H_{\rm int}$ is the internal field associated with M_0. † value from this study at 1.20 GPa. ‡ value from [Kobayashi02] at 1.22 GPa. See also [Aoki11a]

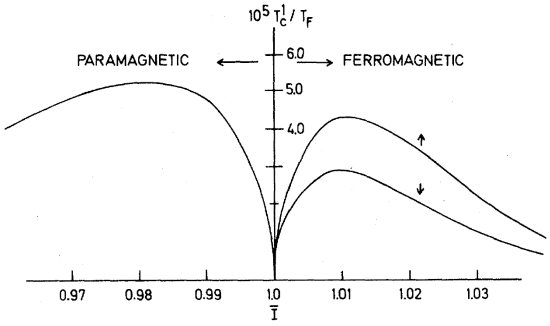

Figure 5.24: The p state superconducting transition temperature as a function of the exchange interaction parameter $\bar{I}$ [Fay80]. The minority band ($\sigma = \uparrow$) has a higher superconducting transition temperature than the majority band ($\sigma = \downarrow$).

5.6 Conclusion and Future Experiments

By performing resistivity measurements and AC calorimetry measurements on the same sample in a piston cylinder cell, we have shown :

- In the FM2 phase, the superconducting transition is broadened in both the resistivity measurements where the zero resistivity is obtained only after a long tail, and in the AC calorimetry measurement where the distribution can be estimated. When this distribution is larger than ~ 150 mK, the superconducting transition cannot be determined in the bulk measurement.

- The enhancement of T_{sc} with magnetic field associated to the FM1-FM2 transition is confirmed for the first time with a bulk probe.

- The small specific heat jump observed at the superconducting transition of UGe_2 by comparison to UCoGe cannot be explained by the distribution of T_{sc} due to pressure inhomogeneity. It seems more related to the large residual term.
- The attribution of the large residual term to the minority band is not obvious and our results suggests that it could be the majority band.

It is difficult to have a finite conclusion concerning the field enhanced superconductivity. Our measurements clearly associate this phenomenon to the FM1-FM2 transition, but efforts are required in order to compare theories with experiments. It will certainly be necessary to confront the models with the critical field measured along the 3 crystallographic axis. In the case of UGe_2, this means it requires to measure 3 samples in a piston cylinder cell, or one sample in a small cell that could be rotated inside a superconducting magnet. In both case, this represents an experimental challenge.

To more precisely investigate the residual contribution below the superconducting temperature, thermal conductivity measurements would be interesting as it is not affected by the nuclear contribution. However, such measurements under pressure remains difficult.

Chapter 6

Conclusion

In this thesis, I have presented a project which started in October 2008 with crystal growth of uranium compounds in a new tetra-arc furnace. New high quality single crystals were obtained, leading to new experimental results on the compounds URu_2Si_2, UCoGe and UGe_2.

With the obtained high quality single crystals of UGe_2, we have reinvestigated the pressure p temperature T phase diagram of this ferromagnetic compound. By applying pressure, the second order transition to the ferromagnetic ordering at low temperature is changes to a first order transition. By performing resistivity measurements on UGe_2 under pressure, we have been able to detect the coordinates of the tricritical point TCP where this change from second order to first order occurs. Moreover, we have been able to follow the evolution of the TCP under an applied magnetic field H parallel to the magnetization axis. When the critical point occurs at 0 K, it is called at a quantum critical end point QCEP. The results presented in this work constitute the first experimental determination of the p-T-H phase diagram with the critical line from the TCP to the proximity of the QCEP of a ferromagnet.

The importance of this work is reinforced by the fact that this phase diagram is general for ferromagnetic compounds. The general character of the theories does not facilitate the comparison with our results, although it opens the field for new theoretical investigations taking into account the specific properties of UGe_2 such as the strong anisotropy and large effective mass....

On the experimental side, this work is a step in studiing a new kind of quantum criticality : the quantum critical end point. Following these results, new similar studies will be performed on other compounds, as it has already started. The extreme measurement conditions to reach the QCEP in UGe_2 remain to be achieved (around 3.5(1) GPa and $17 - 19$ T). In addition, our resistivity measurements are preliminary to new measurements, especially thermodynamic measurements, in order to better ellucidate the physics of this compound. Also, the search for new compounds with easier measurement conditions is hopeful.

Another part of this work focused on the superconducting phase observed under pressure inside the ferromagnetic phase of UGe_2. By AC calorimetry measurements under pressure, we confirmed the rather small amplitude of the heat capacity anomaly in this compound with respect to the other superconducting ferromagnets URhGe and UCoGe. This result cannot arise from poor sample quality or pressure conditions, and we suggest the importance of a residual contribution. Still open questions are whether this residual term arise from the majority or the minority spin band or has another origin, what is the symmetry of the order parameter, is the superconductivity bulk in the large moment phase FM2.... Our results suggest that the majority band has the smallest gap or is ungapped, but other measurements are clearly required to answer this question.

In addition, the enhanced superconductivity which was previously observed from resistivity measurements with a magnetic field applied parallel to the magnetization axis, has been confirmed to be a bulk transition by our AC calorimetry measurements. It has

been compared to the observations in URhGe and UCoGe. In UGe_2, this phenomenon is associated to a field induced first order transition between two ferromagnetic phases FM1 and FM2 which differ by the size of the ordered moment : $M_0 \approx 0.9\ \mu_B$/U in FM1 and $M_0 \approx 1.4\ \mu_B$/U in FM2. It appears that a better understanding of the superconductivity in this compound will require a more precise consideration of the anisotropy of the magnetism, the interactions and the Fermi surface.... The discovery of another superconducting ferromagnet at ambient pressure with good sample quality would be a breakthrough.

Bibliography

[Abrikosov61] A. A. Abrikosov and L. P. Gorkov. *Sov. Phys.-JETP* **12**, 1243–1253, 1961.

[Amitsuka08] H. Amitsuka, K. Matsuda, M. Yokoyama, I. Kawasaki, S. Takayama, Y. Ishihara, K. Tenya, N. Tatelwa, T. C. Kobayashi, and H. Yoshizawa. *Physica B* **403**, 925–927, 2008.

[Andreev07] A. V. Andreev, K. Koyama, N. V. Mushnikov, V. Sechovsky, Y. Shiokawa, I. Satoh, and K. Watanabe. *J. Alloy. Compd.* **441**, 33–38, 2007.

[Aoki00] Dai Aoki. *Fermi Surface Properties of Rare Earth and Uranium Compounds grown by the self-flux and chemical transport methods*. PhD thesis, Department of Physics Graduate school of Science Osaka University, 2000.

[Aoki01] Dai Aoki, Andrew D. Huxley, Eric Ressouche, Daniel Braithwaite, Jacques Flouquet, JP Brison, E Lhotel, and C Paulsen. *Nature* **413**, 613–616, 2001.

[Aoki09a] Dai Aoki, Frederic Bourdarot, Elena Hassinger, Georg Knebel, Atsushi Miyake, Stephane Raymond, Valentin Taufour, and Jacques Flouquet. *J. Phys. Soc. Jpn.* **78**, 053701, 2009.

[Aoki09b] Dai Aoki, Tatsuma D. Matsuda, Valentin Taufour, Elena Hassinger, Georg Knebel, and Jacques Flouquet. *J. Phys. Soc. Jpn.* **78**, 113709, 2009.

[Aoki10] Dai Aoki, F. Bourdarot, E. Hassinger, G. Knebel, A. Miyake, S. Raymond, V. Taufour, and Jacques Flouquet. *J. Phys.-Condes. Matter* **22**, 164205, 2010.

[Aoki11a] Dai Aoki and Jacques Flouquet. *J. Phys. Soc. Jpn.* , submitted as a review, 2011.

[Aoki11b] Dai Aoki, Ilya Sheikin, Tatsuma D. Matsuda, Valentin Taufour, Georg Knebel, and Jacques Flouquet. *J. Phys. Soc. Jpn.* **80**, 013705, 2011.

[Aso05] N Aso, H Nakane, G Motoyama, NK Sato, Y Uwatoko, T Takeuchi, Y Homma, Y Shlokawa, and K Hirota. *Physica B* **359**, 1051–1053, 2005.

[Aso06a] N Aso, G Motoyama, Y Uwatoko, S Ban, S Nakamura, T Nishioka, Y Homma, Y Shiokawa, K Hirota, and N. K. Sato. *Phys. Rev. B* **73**, 054512, 2006.

[Aso06b] Naofumi Aso, Kenji Ohwada, Tetsu Watanuki, Akihiko Machida, Ayako Ohmura, Toshiya Inami, Yoshiya Homma, Yoshinobu Shiokawa, Kazuma Hirota, and Noriaki K. Sato. *J. Phys. Soc. Jpn.* **75S**, 88–90, 2006.

[Ban07] S. Ban, K. Deguchi, N. Aso, Y. Homma, Y. Shiokawa, and N. K. Sato. *J. Magn. Magn. Mater.* **310**, E120–E122, 2007.

[Barnett73] J. D. Barnett, S. Block, and G. J. Piermarini. *Rev. Sci. Instrum.* **44**, 1–9, 1973.

[Bauer01] E. D. Bauer, R. P. Dickey, V .S. Zapf, and M. B. Maple. *J. Phys.-Condes. Matter* **13**, L759–L770, 2001.

[Bean62] C. P. Bean and D. S. Rodbell. *Phys. Rev.* **126**, 104–&, 1962.

[Belitz97] Dietrich Belitz, T. R. Kirkpatrick, and T. Vojta. *Phys. Rev. B* **55**, 9452–9462, 1997.

[Belitz99] Dietrich Belitz, T. R. Kirkpatrick, and T Vojta. *Phys. Rev. Lett.* **82**, 4707–4710, 1999.

[Belitz05] Dietrich Belitz, T. R. Kirkpatrick, and J Rollbuhler. *Phys. Rev. Lett.* **94**, 247205, 2005.

[Belitz07] Dietrich Belitz and Theodore R. Kirkpatrick. *Nature Physics* **3**, 15–16, 2007.

[Bergman76] D. J. Bergman and B. I. Halperin. *Phys. Rev. B* **13**, 2145–2175, 1976.

[Biasini03] M Biasini and R Troc. *Phys. Rev. B* **68**, 245118, 2003.

[Bireckoven88] B. Bireckoven and J Wittig. *J. Phys. E: Sci. Instrum.* **21**, 841–848, 1988.

[Borzi07] R. A. Borzi, S. A. Grigera, J. Farrell, R. S. Perry, S. J. S. Lister, S. L. Lee, D. A. Tennant, Y. Maeno, and A. P. Mackenzie. *Science* **315**, 214–217, 2007.

[Boulet97] P Boulet, A Daoudi, M Potel, H Noel, G. M. Gross, G Andre, and F Bouree. *J. Alloy. Compd.* **247**, 104–108, 1997.

[Bouquet01] F. Bouquet, Y. Wang, R. A. Fisher, D. G. Hinks, J. D. Jorgensen, A. Junod, and N. E. Phillips. *Europhys. Lett.* **56**, 856–862, 2001.

[Bourdarot10a] Frederic Bourdarot, Elena Hassinger, Stephane Raymond, Dai Aoki, Valentin Taufour, and Jacques Flouquet. *J. Phys. Soc. Jpn.* **79**, 094706, 2010.

[Bourdarot10b] Frederic Bourdarot, Elena Hassinger, Stephane Raymond, Dai Aoki, Valentin Taufour, Louis-Pierre Regnault, and Jacques Flouquet. *J. Phys. Soc. Jpn.* **79**, 064719, 2010.

[Bud'ko06] Sergey L. Bud'ko and Paul C. Canfield. *Comptes Rendus Physique* **7**, 56–67, 2006.

[Bulaevskii88] L. N. Bulaevskii, O. V. Dolgov, and M. O. Ptitsyn. *Phys. Rev. B* **38**, 11290–11295, 1988.

[Butch10] Nicholas P. Butch, Jason R. Jeffries, Songxue Chi, Juscelino Batista Leao, Jeffrey W. Lynn, and M. Brian Maple. *Phys. Rev. B* **82**, 060408, 2010.

[Canepa96] F Canepa, P Manfrinetti, M Pani, and A Palenzona. *J. Alloy. Compd.* **234**, 225–230, 1996.

[Canfield96] Paul C. Canfield, Sergey L. Budko, and B. K. Cho. *Physica C* **262**, 249–254, 1996.

[Carneiro77] G. M. Carneiro and C. J. Pethick. *Phys. Rev. B* **16**, 1933–1943, 1977.

[Chandrasekhar62] B. S. Chandrasekhar. *Appl. Phys. Lett.* **1**, 7–8, 1962.

[Chiang74] C. K. Chiang. *Rev. Sci. Instrum.* **45**, 985–989, 1974.

[Chitov01] G. Y. Chitov and A. J. Millis. *Phys. Rev. Lett.* **86**, 5337–5340, 2001.

[Chubukov04] A. V. Chubukov and D. L. Maslov. *Phys. Rev. B* **69**, 121102, 2004.

[Clogston62] A. M. Clogston. *Phys. Rev. Lett.* **9**, 266–&, 1962.

[Coleman05] P. Coleman and A. J. Schofield. *Nature* **433**, 226–229, 2005.

[Czochralski16] J. Czochralski. *Int. Z. Metallogr.* **8**, 1, 1916.

[Czochralski18] J. Czochralski. *Zeitschrift für Physikalische Chemie* **82**, 219–221, 1918.

[Czochralski25] J. Czochralski. *Zeitschrift für Metallkunde* **17**, 1, 1925.

[De Moura76] M. A. De Moura, T. C. Lubensky, Y. Imry, and A. Aharony. *Phys. Rev. B* **13**, 2176–2185, 1976.

[de Visser09] Anne de Visser, N. T. Huy, A. Gasparini, D. E. de Nijs, D. Andreica, C. Baines, and A. Amato. *Phys. Rev. Lett.* **102**, 167003, 2009.

[Dhar92] S. K. Dhar, R. J. Begum, P. Raj, P. Suryanarayana, L. C. Gupta, and R. Vijayaraghavan. *Solid State Commun.* **83**, 965–967, 1992.

[Dolocan05] Voicu Octavian Dolocan. *Imagerie magnétique des supraconducteurs non conventionnels*. PhD thesis, Joseph Fourier University, 2005.

[Domb56] C. Domb. *J. Chem. Phys.* **25**, 783, 1956.

[Fay80] D. Fay and J. Appel. *Phys. Rev. B* **22**, 3173–3182, 1980.

[Fischer75] O. Fischer, M. Decroux, S. Roth, R. Chevrel, and M. Sergent. *J. Phys. C: Solid State Phys.* **8**, L474–L477, 1975.

[Fischer90] O. Fischer. *North-Holland* **5**, 466, 1990.

[Fisher61] E. S. Fisher and H. J. McSkimin. *Phys. Rev.* **124**, 67–&, 1961.

[Fisher68a] M. E. Fisher. *Phys. Rev.* **176**, 257, 1968.

[Fisher68b] ME Fisher and JS Langer. *Phys. Rev. Lett.* **20**, 665–&, 1968.

[Flouquet02] Jacques Flouquet and Alexandre Buzdin. *Physics World*, 41, 2002.

[Galatanu05] A Galatanu, Y Haga, TD Matsuda, S Ikeda, E Yamamoto, Dai Aoki, T Takeuchi, and Y Onuki. *J. Phys. Soc. Jpn.* **74**, 1582–1597, 2005.

[Garland66] C. W. Garland and R. Renard. *J. Chem. Phys.* **44**, 1120, 1966.

[Gehring08] G. A. Gehring. *Europhys. Lett.* **82**, 60004, 2008.

[Goto97] T Goto, Y Shindo, H Takahashi, and S Ogawa. *Phys. Rev. B* **56**, 14019–14028, 1997.

[Griffiths73] R. B. Griffiths. *Phys. Rev. B* **7**, 545–551, 1973.

[Grigera01] S. A. Grigera et al. *Science* **294**, 329–332, 2001.

[Guritanu08] V. Guritanu, N. P. Armitage, R. Tediosi, S. S. Saxena, Andrew D. Huxley, and D. van der Marel. *Phys. Rev. B* **78**, 172406, 2008.

[Haga02] Y Haga, M Nakashima, R Settai, S Ikeda, T Okubo, S Araki, T. C. Kobayashi, N Tateiwa, and Y Onuki. *J. Phys.: Condes. Matter* **14**, L125–L135, 2002.

[Harada05] A Harada, S Kawasaki, H Kotegawa, Y Kitaoka, Y Haga, E Yamamoto, Y Onuki, K. M. Itoh, E. E. Haller, and H Harima. *J. Phys. Soc. Jpn.* **74**, 2675–2678, 2005.

[Harada07] A. Harada, S. Kawasaki, H. Mukuda, Y. Kitaoka, Y. Haga, E. Yamamoto, Y. Onuki, K. M. Itoh, E. E. Haller, and H. Harima. *Phys. Rev. B* **75**, 140502, 2007.

[Hardy04] Frederic Hardy. *Etude du compose ferromagnetique supraconducteur URhGe.* PhD thesis, Universite Joseph Fourier Grenoble 1, 2004.

[Hardy09] F. Hardy, C. Meingast, V. Taufour, Jacques Flouquet, H. v. Loehneysen, R. A. Fisher, N. E. Phillips, Andrew D. Huxley, and J. C. Lashley. *Phys. Rev. B* **80**, 174521, 2009.

[Hardy11] F. Hardy, Dai Aoki, C. Meingast, P. Schweiss, P. Burger, H. v. Loehneysen, and Jacques Flouquet. *Phys. Rev. B* **83**, 195107, 2011.

[Harrison03] N. Harrison, M. Jaime, and J. A. Mydosh. *Phys. Rev. Lett.* **90**, 096402, 2003.

[Hassinger08] E. Hassinger, G. Knebel, K. Izawa, P. Lejay, B. Salce, and Jacques Flouquet. *Phys. Rev. B* **77**, 115117, 2008.

[Hassinger10] E. Hassinger, G. Knebel, T. D. Matsuda, Dai Aoki, V. Taufour, and Jacques Flouquet. *Phys. Rev. Lett.* **105**, 216409, 2010.

[Hertz76] J. A. Hertz. *Phys. Rev. B* **14**, 1165–1184, 1976.

[Hill70] H. H. Hill. *Nuclear Metallurgy* **17**, , 1970.

[Howald11] Ludovic Howald. *Interactions entre la supraconductivité et la criticité quantique dans les composés CeCoIn5, URhGe et UCoGe.* PhD thesis, University Joseph Fourier, 2011.

[Hu72] C. R. Hu and R. S. Thompson. *Phys. Rev. B* **6**, 110–&, 1972.

[Huxley00] Andrew D. Huxley, I. Sheikin, and Daniel Braithwaite. *Physica B* **284**, 1277–1278, 2000.

[Huxley01] Andrew D. Huxley, I. Sheikin, Eric Ressouche, N. Kernavanois, Daniel Braithwaite, R. Calemczuk, and Jacques Flouquet. *Phys. Rev. B* **63**, 144519, 2001.

[Huxley03a] Andrew D. Huxley, S Raymond, and Eric Ressouche. *Phys. Rev. Lett.* **91**, 207201, 2003.

[Huxley03b] Andrew D. Huxley, Eric Ressouche, B Grenier, Dai Aoki, Jacques Flouquet, and C Pfleiderer. *J. Phys.-Condes. Matter* **15**, S1945–S1955, 2003.

[Huxley04] Andrew D. Huxley, V. Mineev, B. Grenier, Eric Ressouche, Dai Aoki, J. P. Brison, and Jacques Flouquet. *Physica C* **403**, 9–14, 2004.

[Huy07] N. T. Huy, A. Gasparini, D. E. de Nijs, Y. Huang, J. C. P. Klaasse, T. Gortenmulder, Anne de Visser, A. Hamann, T. Gorlach, and H. v. Lohneysen. *Phys. Rev. Lett.* **99**, 067006, 2007.

[Huy08] N. T. Huy, D. E. de Nijs, Y. K. Huang, and Anne de Visser. *Phys. Rev. Lett.* **100**, 077002, 2008.

[Hykel11] Danny Hykel. *Microscopie à micro-SQUID : étude de la coexistence de la supraconductivité et du ferromagnetisme dans le composé UCoGe*. PhD thesis, Université Joseph Fourier, 2011.

[Ishii93] T Ishii. *Physica B* **188**, 21–25, 1993.

[Ishii03] Y. Ishii, M. Kosaka, Y. Uwatoko, A. V. Andreev, and V. Sechovsky. *Physica B* **334**, 160–166, 2003.

[Ito02] Takahiro Ito, Hiroshi Kumigashira, Seigo Souma, Takashi Takahashi, Yoshinori Haga, and Yoshichika Ōnuki. *J. Phys. Soc. Jpn.* **71S**, 261–263, 2002.

[Jaccarino62] V. Jaccarino and M. Peter. *Phys. Rev. Lett.* **9**, 290–&, 1962.

[Kabeya09] N. Kabeya, R. Iijima, E. Osaki, S. Ban, K. Imura, K. Deguchi, N. Aso, Y. Homma, Y. Shiokawa, and N. K. Sato. *Physica B* **404**, 3238–3241, 2009.

[Kambe99] S Kambe, Andrew D. Huxley, P Rodiere, C Paulsen, and Jacques Flouquet. *Physica B* **259–61**, 670–671, 1999.

[Kernavanois01] N Kernavanois, B Grenier, Andrew D. Huxley, Eric Ressouche, J. P. Sanchez, and Jacques Flouquet. *Phys. Rev. B* **64**, 174509, 2001.

[Khalifah04] P. Khalifah, I. Ohkubo, H. M. Christen, and D. G. Mandrus. *Phys. Rev. B* **70**, 134426, 2004.

[Khmelnitskii75] D. E. Khmelnitskii and V. L. Shneerson. *Sov. Phys.-JETP* **42**, 560, 1975.

[Kim03] K. H. Kim, N. Harrison, M. Jaime, G. S. Boebinger, and J. A. Mydosh. *Phys. Rev. Lett.* **91**, 256401, 2003.

[Kim04] K. H. Kim, N. Harrison, M. Jaime, G. S. Boebinger, and J. A. Mydosh. *J. Magn. Magn. Mater.* **272**, 50–51, 2004.

[Kimura04] N Kimura, M Endo, T Isshiki, S Minagawa, A Ochiai, H Aoki, T Terashima, S Uji, T Matsumoto, and G. G. Lonzarich. *Phys. Rev. Lett.* **92**, 197002, 2004.

[Kirkpatrick01] T. R. Kirkpatrick, Dietrich Belitz, T. Vojta, and R. Narayanan. *Phys. Rev. Lett.* **87**, 127003, 2001.

[Kirkpatrick11] T. R. Kirkpatrick and Dietrich Belitz. *Phys. Rev. Lett.* **106**, 105701, 2011.

[Kitaoka05] Y Kitaoka, H Kotegawa, A Harada, S Kawasaki, Y Kawasaki, Y Haga, E Yamamoto, Y Onuki, KM Itoh, EE Haller, and H Harima. *J. Phys.-Condes. Matter* **17**, S975–S986, 2005.

[Knebel06] G. Knebel, Dai Aoki, Daniel Braithwaite, B. Salce, and Jacques Flouquet. *Phys. Rev. B* **74**, 020501, 2006.

[Kobayashi02] T. C. Kobayashi, K Hanazono, N Tateiwa, K Amaya, Y Haga, R Settai, and Y Onuki. *J. Phys.: Condes. Matter* **14**, 10779–10782, 2002.

[Kohn59] W Kohn. *Phys. Rev. Lett.* **2**, 393–394, 1959.

[Konoike04] T Konoike, S Uji, T Terashima, M Nishimura, S Yasuzuka, K Enomoto, H Fujiwara, B Zhang, and H Kobayashi. *Phys. Rev. B* **70**, 094514, 2004.

[Kotegawa04] H. Kotegawa, S. Kawasaki, A. Harada, Y. Kawasaki, K. Okamoto, G. Q. Zheng, Y. Kitaoka, E. Yamamoto, Y. Haga, Y. Onuki, K. M. Itoh, and E. E. Haller. *J. Magn. Magn. Mater.* **272**, E27–E28, 2004.

[Kotegawa05] H Kotegawa, A Harada, S Kawasaki, Y Kawasaki, Y Kitaoka, Y Haga, E Yamamoto, Y Onuki, K. M. Itoh, E. E. Haller, and H Harima. *J. Phys. Soc. Jpn.* **74**, 705–711, 2005.

[Kotegawa11] Hisashi Kotegawa, Valentin Taufour, Dai Aoki, Georg Knebel, and Jacques Flouquet. *J. Phys. Soc. Jpn.* **80**, 083703, 2011.

[Kuwahara07] K. Kuwahara, T. Sakai, M. Kohgi, Y. Haga, and Y. Onuki. *J. Magn. Magn. Mater.* **310**, 362–364, 2007.

[Larkin69] A. I. Larkin and S. A. Pikin. *Sov. Phys.-JETP* **29**, 891, 1969.

[Laughlin01] R. B. Laughlin, G. G. Lonzarich, P. Monthoux, and D. Pines. *Adv. Phys.* **50**, 361–365, 2001.

[Lebech89] B. Lebech, J. Bernhard, and T. Freltoft. *J. Phys.-Condes. Matter* **1**, 6105–6122, 1989.

[Levy06] Florence Levy. *Etude de la coexistence de la supraconductivite et du ferromagnetisme dans le compose URhGe.* PhD thesis, Universite Joseph Fourier Grenoble 1, 2006.

[Linder08] Jacob Linder, Iver B. Sperstad, Andriy H. Nevidomskyy, Mario Cuoco, and Asle Sudbo. *Phys. Rev. B* **77**, 184511, 2008.

[Lévy05] F. Lévy, I. Sheikin, B. Grenier, and Andrew D. Huxley. *Science* **309**, 1343–1346, 2005.

[Machida01] K Machida and T Ohmi. *Phys. Rev. Lett.* **86**, 850–853, 2001.

[Makarov59] E. S. Makarov and V. N. Bykov. *Sov. Phys. Crystallogr.* **4**, 164, 1959.

[Marmeggi99] JC Marmeggi, R Currat, A Bouvet, and GH Lander. *Physica B* **263**, 624–626, 1999.

[Maslov09] Dmitrii L. Maslov and Andrey V. Chubukov. *Phys. Rev. B* **79**, 075112, 2009.

[Matsuda00] T. D. Matsuda, H. Okada, H. Sugawara, Y. Aoki, H. Sato, A. V. Andreev, Y. Shiokawa, V. Sechovsky, T. Honma, E. Yamamoto, and Y. Onuki. *Physica B* **281**, 220–222, 2000.

[Matthias58] B. T. Matthias, H. Suhl, and E. Corenzwit. *Phys. Rev. Lett.* **1**, 92–94, 1958.

[Mattis63] D. C. Mattis and T. D. Schultz. *Phys. Rev.* **129**, 175, 1963.

[McCumber63] D. E. McCumber and M. D. Sturge. *J. Appl. Phys.* **34**, 1682, 1963.

[McMillan68] W. L. McMillan. *Phys. Rev.* **167**, 331, 1968.

[Menovsky83] A. Menovsky, F. R. de Boer, P. H. Frings, and J. J. M. Franse. *High Field Magnetism*, 189, 1983.

[Meul84] H. W. Meul, C. Rossel, M. Decroux, O. Fischer, G. Remenyi, and A. Briggs. *Phys. Rev. Lett.* **53**, 497–500, 1984.

[Meyer01] D Meyer and W Nolting. *Phys. Rev. B* **64**, 052402, 2001.

[Millis93] A. J. Millis. *Phys. Rev. B* **48**, 7183–7196, 1993.

[Millis02] A. J. Millis, A. J. Schofield, G. G. Lonzarich, and S. A. Grigera. *Phys. Rev. Lett.* **88**, 217204, 2002.

[Mineev11a] V. P. Mineev. *Phys. Rev. B* **83**, 064515, 2011.

[Mineev11b] Vladimir P. Mineev. *Comptes Rendus Physique* **12**, 567–572, 2011.

[Misawa71] S. Misawa. *Phys. Rev. Lett.* **26**, 1632, 1971.

[Misiorek05] H Misiorek, J Mucha, R Troc, and B Coqblin. *J. Phys.-Condes. Matter* **17**, 679–688, 2005.

[Miyake02] K Miyake and O Narikiyo. *J. Phys. Soc. Jpn.* **71**, 867–871, 2002.

[Miyake08] Atsushi Miyake, Dai Aoki, and Jacques Flouquet. *J. Phys. Soc. Jpn.* **77**, 094709, 2008.

[Miyake09] Atsushi Miyake, Alain Villaume, Yoshinori Haga, Georg Knebel, Bernard Salce, Gerard Lapertot, and Jacques Flouquet. *J. Phys. Soc. Jpn.* **78**, 044703, 2009.

[Mohn89] P Mohn and G Hilscher. *Phys. Rev. B* **40**, 9126–9134, 1989.

[Mohn02] Peter Mohn. *Magnetism in the Solid State*. Springer, 2002.

[Monthoux01] P. Monthoux and G. G. Lonzarich. *Phys. Rev. B* **63**, 054529, 2001.

[Moriya95] T. Moriya and T. Takimoto. *J. Phys. Soc. Jpn.* **64**, 960–969, 1995.

[Motoyama01] G Motoyama, S Nakamura, H Kadoya, T Nishioka, and NK Sato. *Phys. Rev. B* **65**, 020510, 2001.

[Motoyama03] G Motoyama, T Nishioka, and N. K. Sato. *Phys. Rev. Lett.* **90**, 166402, 2003.

[Murata72] K. K. Murata and S Doniach. *Phys. Rev. Lett.* **29**, 285, 1972.

[Murata77] K. K. Murata. *Phys. Rev. B* **15**, 4328–4335, 1977.

[Nakane05] H Nakane, G Motoyama, T Nishioka, and N. K. Sato. *J. Phys. Soc. Jpn.* **74**, 855–858, 2005.

[Niklowitz05] P. G. Niklowitz, F. Beckers, G. G. Lonzarich, G. Knebel, B. Salce, J. Thomasson, N. Bernhoeft, Daniel Braithwaite, and Jacques Flouquet. *Phys. Rev. B* **72**, 024424, 2005.

[Nishimura94] K. Nishimura, G. Oomi, S.W. Yun, and Y. Onuki. *J. Alloys Comp.* **213-214**, 383–386, 1994.

[Ohmi93] T Ohmi and K Machida. *Phys. Rev. Lett.* **71**, 625–628, 1993.

[Ohta10] Tetsuya Ohta, Taisuke Hattori, Kenji Ishida, Yusuke Nakai, Eisuke Osaki, Kazuhiko Deguchi, Noriaki K. Sato, and Isamu Satoh. *J. Phys. Soc. Jpn.* **79**, 023707, 2010.

[Oikawa96] K Oikawa, T Kamiyama, H Asano, Y Onuki, and M Kohgi. *J. Phys. Soc. Jpn.* **65**, 3229–3232, 1996.

[Olsen60] C. E. Olsen. *J. Appl. Phys.* **31**, S340–S341, 1960.

[Onuki91] Y Onuki, S. W. Yun, I Ukon, I Umehara, K Satoh, I Sakamoto, M Hunt, P Meeson, P. A. Probst, and M Springford. *J. Phys. Soc. Jpn.* **60**, 2127–2130, 1991.

[Onuki92] Y Onuki, I Ukon, S. W. Yun, I Umehara, K Satoh, T Fukuhara, H Sato, S Takayanagi, M Shikama, and A Ochiai. *J. Phys. Soc. Jpn.* **61**, 293–299, 1992.

[Oomi93] G Oomi, K Nishimura, Y Onuki, and S. W. Yun. *Physica B* **188**, 758–760, 1993.

[Oomi95] Gendo Oomi, Tomoko Kagayama, Kazutaka Nishimura, S. W. Yun, and Yoshichika Onuki. *Physica B* **206-207**, 515–518, 1995.

[Oomi98] G Oomi, T Kagayama, and Y Onuki. *J. Alloy. Compd.* **271**, 482–485, 1998.

[Padamsee73] H. Padamsee, J. E. Neighbor, and C. A. Shiffman. *J. Low Temp. Phys.* **12**, 387–411, 1973.

[Palstra85] T. T. M. Palstra, A. A. Menovsky, J. Vandenberg, A. J. Dirkmaat, P. H. Kes, G. J. Nieuwenhuys, and J. A. Mydosh. *Phys. Rev. Lett.* **55**, 2727–2730, 1985.

[Papon02] Pierre Papon, Jacques Leblond, and Paul H. E. Meijer. *Physique des transitions de phases Concepts et applications*. Dunod, second edition edition, 2002.

[Park94] J. G. Park and B. R. Coles. *J. Phys.-Condes. Matter* **6**, 1425–1430, 1994.

[Pedrazzini07] P. Pedrazzini, H. Wilhelm, D. Jaccard, T. Jarlborg, M. Schmidt, M. Hanfland, L. Akselrud, H. Q. Yuan, U. Schwarz, Yu. Grin, and F. Steglich. *Phys. Rev. Lett.* **98**, 047204, 2007.

[Pfleiderer97] C Pfleiderer, GJ McMullan, SR Julian, and GG Lonzarich. *Phys. Rev. B* **55**, 8330–8338, 1997.

[Pfleiderer01] C Pfleiderer, SR Julian, and GG Lonzarich. *Nature* **414**, 427–430, 2001.

[Pfleiderer02] C Pfleiderer and Andrew D. Huxley. *Phys. Rev. Lett.* **89**, 147005, 2002.

[Pfleiderer07] C. Pfleiderer, P. Boni, T. Keller, U. K. Rossler, and A. Rosch. *Science* **316**, 1871–1874, 2007.

[Pfleiderer09] Christian Pfleiderer. *Rev. Mod. Phys.* **81**, 1551–1624, 2009.

[Piermarini75] G. J. Piermarini, S. Block, J. D. Barnett, and R. A. Forman. *J. Appl. Phys.* **46**, 2774–2780, 1975.

[Raymond04] S Raymond and Andrew D. Huxley. *Physica B* **350**, 33–35, 2004.

[Raymond06] S Raymond and Andrew D. Huxley. *Phys. Rev. B* **73**, 094420, 2006.

[Rech06] Jerome Rech, Catherine Pepin, and Andrey V. Chubukov. *Phys. Rev. B* **74**, 195126, 2006.

[Rice54] O. K. Rice. *J. Chem. Phys.* **22**, 1535–1544, 1954.

[Roussev01] R. Roussev and A. J. Millis. *Phys. Rev. B* **63**, 140504, 2001.

[Rowley10] Stephen Rowley et al. *Phys. Status Solidi B-Basic Solid State Phys.* **247**, 469–475, 2010.

[Sak74] J Sak. *Phys. Rev. B* **10**, 3957–3960, 1974.

[Sakarya05] S. Sakarya, N. H. van Dijk, and E. Bruck. *Phys. Rev. B* **71**, 174417, 2005.

[Sakon07] T. Sakon, S. Saito, K. Koyama, S. Awaji, I. Sato, T. Nojima, K. Watanabe, and N. K. Sato. *Phys. Scr.* **75**, 546–550, 2007.

[Sandeman02] K. G. Sandeman, G. G. Lonzarich, and A. J. Schofield. *arXiv:cond-mat* , 0210552, 2002.

[Sandeman03] K. G. Sandeman, G. G. Lonzarich, and A. J. Schofield. *Phys. Rev. Lett.* **90**, 167005, 2003.

[Satoh92] K Satoh, S. W. Yun, I Umehara, Y Onuli, S Uji, T Shimizu, and H Aoki. *J. Phys. Soc. Jpn.* **61**, 1827–1828, 1992.

[Satoh01] H. Satoh and F. J. Ohkawa. *Phys. Rev. B* **63**, 184401, 2001.

[Saxena00] S. S. Saxena et al. *Nature* **406**, 587–592, 2000.

[Settai02] R Settai et al. *J. Phys.: Condes. Matter* **14**, L29–L36, 2002.

[Settai03] R Settai, M Nakashima, H Shishido, Y Haga, H Yamagami, and Y Onuki. *Acta Phys. Pol. B* **34**, 725–728, 2003.

[Sheikin01] I Sheikin, Andrew D. Huxley, Daniel Braithwaite, JP Brison, S Watanabe, K Miyake, and Jacques Flouquet. *Phys. Rev. B* **64**, 220503, 2001.

[Shick01] A. B. Shick and W. E. Pickett. *Phys. Rev. Lett.* **86**, 300–303, 2001.

[Shick04] AB Shick, V Janis, V Drchal, and WE Pickett. *Phys. Rev. B* **70**, 134506, 2004.

[Shimizu64] M Shimizu. *Proc. Phys. Soc. of London* **84**, 397–&, 1964.

[Sidorov11] V. A. Sidorov, V. N. Krasnorussky, A. E. Petrova, A. N. Utyuzh, W. M. Yuhasz, T. A. Lograsso, J. D. Thompson, and S. M. Stishov. *Phys. Rev. B* **83**, 060412, 2011.

[Skalski64] S. Skalski, O. Betbeder, and P. R. Weiss. *Phys. Rev. A* **136**, 1500, 1964.

[Soda91] K Soda, T Mori, Y Onuki, T Komatsubara, S Suga, A Kakizaki, and T Ishii. *J. Phys. Soc. Jpn.* **60**, 3059–3066, 1991.

[Stockert11] U. Stockert and N. Oeschler. *Cryogenics* **51**, 154–155, 2011.

[Su75] D. R. Su and T. M. Wu. *J. Low Temp. Phys.* **19**, 481–491, 1975.

[Sugiyama90] K. Sugiyama, H. Fuke, K. Kinko, K. Shimohata, A. A. Menovsky, J. A. Mydosh, and M Date. *J. Phys. Soc. Jpn.* **59**, 3331–3339, 1990.

[Sugiyama99] K Sugiyama, M Nakashima, H Ohkuni, K Kindo, Y Haga, T Honma, E Yamamoto, and Y Onuki. *J. Phys. Soc. Jpn.* **68**, 3394–3401, 1999.

[Sullivan68] P. F. Sullivan and G. Seidel. *Phys. Rev.* **173**, 679, 1968.

[Sumiyama86] A Sumiyama, Y Oda, H Nagano, Y Onuki, K Shibutani, and T Komatsubara. *J. Phys. Soc. Jpn.* **55**, 1294–1304, 1986.

[Takahashi93] H Takahashi, N Mori, Y Onuki, and S. W. Yun. *Physica B* **188**, 772–774, 1993.

[Tateiwa01a] N Tateiwa, K Hanazono, T. C. Kobayashi, K Amaya, T Inoue, K Kindo, Y Koike, N Metoki, Y Haga, R Settai, and Y Onuki. *J. Phys. Soc. Jpn.* **70**, 2876–2879, 2001.

[Tateiwa01b] N Tateiwa, T. C. Kobayashi, K Hanazono, K Amaya, Y Haga, R Settai, and Y Onuki. *J. Phys.-Condes. Matter* **13**, L17–L23, 2001.

[Tateiwa02] N Tateiwa, T. C. Kobayashi, K Amaya, Y Haga, R Settai, and Y Onuki. *Physica B* **312**, 109–111, 2002.

[Tateiwa04] N Tateiwa, TC Kobayashi, K Amaya, Y Haga, R Settai, and Y Onuki. *Phys. Rev. B* **69**, 180513, 2004.

[Tateiwa07] Naoyuki Tateiwa, Yoshinori Haga, Tatsuma D. Matsuda, Shugo Ikeda, Etsuji Yamamoto, Yusuke Okuda, Yuichiro Miyauchi, Rikio Settai, and Yoshichika Onuki. *J. Phys. Soc. Jpn.* **76**, 083706, 2007.

[Tateiwa09] Naoyuki Tateiwa and Yoshinori Haga. *Rev. Sci. Instrum.* **80**, 123901, 2009.

[Tatsuoka10] Sho Tatsuoka, Makoto Watanabe, Bunya Suemitsu, Yoshinori Ogawa, Atsushi Yamada, Kazuyuki Matsubayashi, Yoshiya Uwatoko, Ryuji Higashinaka, Yuji Aoki, Takahiro Namiki, Keitaro Kuwahara, and Hideyuki Sato. *J. Phys. Soc. Jpn.* **79**, 063704, 2010.

[Taufour10] V. Taufour, Dai Aoki, G. Knebel, and Jacques Flouquet. *Phys. Rev. Lett.* **105**, 217201, 2010.

[Taufour11] V. Taufour, A. Villaume, Dai Aoki, G. Knebel, and Jacques Flouquet. Magnetic Field Evolution of Critical end Point in UGe2. In *Journal of Physics: Conference Series*, volume 273, 012017 (4 pp.), UK, 2011. IOP Publishing Ltd. International Conference on Strongly Correlated Electron Systems (SCES 2010), „ Santa Fe, NM, USA.

[Taylor07] O. J. Taylor, A. Carrington, and J. A. Schlueter. *Phys. Rev. Lett.* **99**, 057001, 2007.

[Terashima01] T Terashima, T Matsumoto, C Terakura, S Uji, N Kimura, M Endo, T Komatsubara, and H Aoki. *Phys. Rev. Lett.* **87**, 166401, 2001.

[Terashima02] T Terashima, T Matsumoto, C Terakura, S Uji, N Kimura, M Endo, T Komatsubara, H Aoki, and K Maezawa. *Phys. Rev. B* **65**, 174501, 2002.

[Terashima06] T Terashima et al. *Phys. Rev. B* **73**, 140406, 2006.

[Terashima07] T. Terashima, K. Enomoto, T. Konoike, T. Matsumoto, S. Uji, N. Kimura, M. Endo, T. Komatsubara, H. Aoki, and K. Maezawa. *J. Magn. Magn. Mater.* **310**, E116–E117, 2007.

[Thomasson97] J. Thomasson, Y. Dumont, J. C. Griveau, and C. Ayache. *Rev. Sci. Instrum.* **68**, 1514–1517, 1997.

[Thomasson98] J. Thomasson, Y. Okayama, I. Sheikin, J. P. Brison, and Daniel Braithwaite. *Solid State Commun.* **106**, 637–641, 1998.

[Tokiwa00] Y Tokiwa, H Harima, Dai Aoki, S Nojiri, M Murakawa, K Miyake, N Watanabe, R Settai, Y Inada, H Sugawara, H Sato, Y Haga, E Yamamoto, and Y Onuki. *J. Phys. Soc. Jpn.* **69**, 1105–1112, 2000.

[Tomaszewski02] P. E. Tomaszewski. *J. Cryst. Growth* **236**, 1–4, 2002.

[Tran98] V. H. Tran, R Troc, and G Andre. *J. Magn. Magn. Mater.* **186**, 81–86, 1998.

[Tran04] V. H. Tran, S. Paschen, R. Troc, M. Baenitz, and F. Steglich. *Phys. Rev. B* **69**, 195314, 2004.

[Uemura07] Y. J. Uemura et al. *Nature Physics* **3**, 29–35, 2007.

[Uhlarz04] M Uhlarz, C Pfleiderer, and S. M. Hayden. *Phys. Rev. Lett.* **93**, 256404, 2004.

[Uji01] S Uji, H Shinagawa, T Terashima, T Yakabe, Y Terai, M Tokumoto, A Kobayashi, H Tanaka, and H Kobayashi. *Nature* **410**, 908–910, 2001.

[Uji05] S Uji, S Yasuzuka, M Tokumoto, H Tanaka, A Kobayashi, B Zhang, H Kobayashi, E. S. Choi, D Graf, and J. S. Brooks. *Phys. Rev. B* **72**, 184505, 2005.

[Vaks81] V. G. Vaks, A. V. Trefilov, and S. V. Fomichev. *Sov. Phys.-JETP* **53**, 830, 1981.

[Villaume08] A. Villaume, F. Bourdarot, E. Hassinger, S. Raymond, V. Taufour, Dai Aoki, and Jacques Flouquet. *Phys. Rev. B* **78**, 012504, 2008.

[Vollmer02] R Vollmer, C Pfleiderer, H von Lohneysen, E. D. Bauer, and M. B. Maple. *Physica B* **312**, 112–114, 2002.

[Wang69] Y. L. Wang and B. R. Cooper. *Phys. Rev.* **185**, 696–&, 1969.

[Watanabe02] S Watanabe and K Miyake. *J. Phys. Soc. Jpn.* **71**, 2489–2499, 2002.

[Wegner74] F. J. Wegner. *J. Phys. C: Solid State Phys.* **7**, 2109–2125, 1974.

[Wu11] W. Wu, A. McCollam, S. A. Grigera, R. S. Perry, A. P. Mackenzie, and S. R. Julian. *Phys. Rev. B* **83**, 045106, 2011.

[Yamada93] H. Yamada. *Phys. Rev. B* **47**, 11211–11219, 1993.

[Yamada99] H Yamada and K Terao. *Phys. Rev. B* **59**, 9342–9347, 1999.

[Yamada07] H. Yamada. *Physica B* **391**, 42–46, 2007.

[Yamagami93] H Yamagami and A Hasegawa. *Physica B* **188**, 182–184, 1993.

[Yamaji06] Youhei Yamaji, Takahiro Misawa, and Masatoshi Imada. *J. Phys. Soc. Jpn.* **75**, 094719, 2006.

[Yamaji07] Youhei Yamaji, Takahiro Misawa, and Masatoshi Imada. *J. Phys. Soc. Jpn.* **76**, 063702, 2007.

[Yamamoto04] E. Yamamoto, Y. Haga, T. D. Matsuda, S. Ikeda, Y. Inada, R. Settai, and Y. Onuki. *J. Magn. Magn. Mater.* **272**, E171–E172, 2004.

Résumé des chapitres en français

Chapitre 1

Dans ce chapitre, le contexte scientifique général est présenté rapidement. Les composés à base dúranium sont introduits à partir du diagramme de Hill qui distingue les propriétés magnétiques ou supraconductices de ces matériaux en fonction de la distance entre les plus proches atomes d'uranium. Ce diagramme montre aussi la séparation qui existe la plupart du temps entre le magnétisme et la supraconductivité. Les composés Fermions lourds sont des exceptions à ce diagramme et sont également introduits dans ce chapitre. Le plan de la thèse est ensuite annoncé.

Chapitre 2

Les techniques expérimentales utilisées durant la thèse sont exposées dans ce chapitre. La préparation des monocristaux par la technique de Czochralski a été réalisée dans un four tétra-arc qui a été acheté au début de la thèse. Différentes étapes de la préparation des cristaux sont présentées (recuit, polissage, découpe...). Les techniques de mesures dans des conditions extrêmes de température, champ magnétique et pression sont présentées, ainsi que les techniques de mesures de chaleur spécifique alternative et d'expansion thermique sous pression. La dernière partie de ce chapitre présente quelques-uns des nouveaux résultats obtenus à partir des cristaux réalisés pendant la thèse sur URu_2Si_2 et UCoGe.

Chapitre 3

Ce chapitre constitue une introduction étendue à la physique du composé UGe_2. Différents résultats de la littérature scientifique sont comparés. L'ordre des transitions de phase observées dans ce composé est présenté. Les propriétés de la phase supraconductrice qui coexiste avec le ferromagnétisme sont examinées. Quelques points inexplorés apparaissent :

- La position du CEP qui termine la ligne de transition de phase du premier ordre entre la phase FM1 et FM2 n'est pas connue. Au dessus de ce point, un crossover est observé signifiant que l'on passe continument de la phase FM2 à la phase FM1.
- La position du TCP n'est également pas déterminée. Au TCP, la transition de deuxième ordre entre l'état paramagnétique et l'état ferromagnétique devient du premier ordre.
- Il n'y a pas de résultat au dessus de 2 GPa.
- Les résultats provenant de la littérature sur le saut de chaleur spécifique à la transition supraconductrice montrent une petite valeur du saut et n'ont jamais été confirmés, du fait de la difficulté expérimentale de cette mesure sous pression.

Cela présente les motivations du travail expérimental présenté dans les chapitres 4 et 5.

Chapitre 4

Dans ce chapitre, le diagramme de phase de UGe_2 est présenté avec pour nouveau résultat la position du TCP et une nouvelle ligne dans l'espace température-pression-champ magnétique. Cette ligne émerge du TCP (à 24 K dans le cas d'UGe_2) et descend en température. Les résultats montrent que cette ligne atteint 0 K autour de 3.6 GPa et 18 T, ce qui constitue la première estimation de la position d'un nouveau type de point critique quantique, le QCEP. Le nouveau diagramme de phase de UGe_2 a une structure avec des ailes (wings) qui sont détectées pour la première fois expérimentalement, alors que ce type de diagramme est prédit par la théorie comme général à tous les composés ferromagnétiques (dont la température de Curie peut être réduite à 0 K par un paramètre tel que la pression ou le dopage).

La détermination de ce diagramme de phase par des mesures de résistivité et d'effet Hall est décrite. Les premiers résultats sur le coefficient A de la résistivité à proximité du QCEP sont aussi présentés.

Les différentes théories sont exposées, ainsi que les premières comparaisons avec les résultats expérimentaux.

Dans la dernière partie de ce chapitre, la position du CEP ainsi que son évolution sous champ magnétique sont présentées à partir de mesures de résistivité et de dilatation thermique.

Chapitre 5

Ce chapitre traite de la phase supraconductrice qui coexiste avec le ferromagnétisme dans UGe_2. Les résultats des mesures de résistivité et de chaleur spécifique alternative sous pression sont présentés. Dans la phase FM1, la largeur de transition en résistivité et en chaleur spécifique augmente rapidement, alors que la température de transition T_{sc} diminue rapidement lorsque l'on s'éloigne de la pression critique p_x ou du champ critique H_x qui séparent la phase FM1 de la phase FM2. Dans la phase FM2, la faible valeur du saut en chaleur spécifique est confirmée. De plus, un renforcement de la supraconductivité sous champ magnétique est mesuré. Ce résultat constitue une confirmation par une mesure volumique (la chaleur spécifique) des résultats récemment observés en résistivité dans les trois ferromagnétiques supraconducteurs UCoGe, URhGe et UGe_2. La comparaison entre ces composés est également présentée.

Chapitre 6

Ce chapitre reprend les principaux résultats des chapitres précédents.

Abstract

In this thesis, the study on the superconducting ferromagnet UGe_2 is presented. Crystal growth of UGe_2 single crystals was realized in a tetra-arc furnace using the Czochralski technique. This technique was also used to obtain high quality single crystals of other uranium compounds, notably UCoGe and URu_2Si_2. The Curie temperature of UGe_2 ($T_{\mathrm{Curie}} = 53$ K) decreases with pressure and is suppressed at $p_c = 1.5$ GPa. Before being suppressed, the ferromagnetic transition changes from second to first order at a tricritical point. Precise resistivity and Hall resistivity measurements under pressure and magnetic field revealed the position of the tricritical point as well as its evolution under magnetic field which draw a wing structure phase diagram. Despite the theoretical prediction that this diagram is general for a ferromagnet, here we present the first experimental observation. Other measurements focus on the superconductivity ($T_{sc} = 0.75$ K) which coexists with ferromagnetism under pressure. The bulk nature of the superconductivity is investigated by AC calorimetry measurements under pressure. The attention is turned to the interesting phenomenon of field enhanced superconductivity.

Résumé

Cette thèse porte sur l'étude du composé supraconducteur ferromagnétique UGe_2. La croissance de monocristaux de UGe_2 a été réalisée dans un four tétra-arc par la technique du tirage Czochralski. Cette technique a également servi à l'obtention d'autres composés à base d'uranium, notamment UCoGe et URu_2Si_2. Pour la première fois, la structure avec des ailes (wings) du diagramme de phase de UGe_2 a été vérifiée expérimentalement. Cette observation est une conséquence d'une température de transition ferromagnétique qui décroît par application d'un paramètre extérieur tel que la pression, et qui devient du premier ordre avant de disparaître. Le changement d'ordre se fait à un point tricritique. D'autres mesures ont porté sur la transition supraconductrice qui se produit à l'intérieur de la phase ferromagnétique. La nature volumique de la supraconductivité a été confirmée et l'accent s'est porté sur son renforcement sous champ magnétique.